UC Irvine

UC Irvine Previously Published Works

Title

The clustering of galaxies in the SDSS-III Baryon Oscillation Spectroscopic Survey: baryon acoustic oscillations in the Data Release 9 spectroscopic galaxy sample

Permalink

https://escholarship.org/uc/item/78x5n2dr

Journal

Monthly Notices of the Royal Astronomical Society, 427(4)

ISSN

0035-8711

Authors

Anderson, Lauren
Aubourg, Eric
Bailey, Stephen
et al.

Publication Date

2012-12-21

DOI

10.1111/j.1365-2966.2012.22066.x

Copyright Information

This work is made available under the terms of a Creative Commons Attribution License, availalbe at https://creativecommons.org/licenses/by/4.0/

Peer reviewed

eScholarship.org Powered by the California Digital Library
University of California

Monthly Notices
of the
ROYAL ASTRONOMICAL SOCIETY

MNRAS **441,** 24–62 (2014) doi:10.1093/mnras/stu523

The clustering of galaxies in the SDSS-III Baryon Oscillation Spectroscopic Survey: baryon acoustic oscillations in the Data Releases 10 and 11 Galaxy samples

Lauren Anderson,[1] Éric Aubourg,[2] Stephen Bailey,[3] Florian Beutler,[3] Vaishali Bhardwaj,[1,3] Michael Blanton,[4] Adam S. Bolton,[5] J. Brinkmann,[6] Joel R. Brownstein,[5] Angela Burden,[7] Chia-Hsun Chuang,[8] Antonio J. Cuesta,[9,10] Kyle S. Dawson,[5] Daniel J. Eisenstein,[11] Stephanie Escoffier,[12] James E. Gunn,[13] Hong Guo,[5] Shirley Ho,[14] Klaus Honscheid,[15,16] Cullan Howlett,[7] David Kirkby,[17] Robert H. Lupton,[14] Marc Manera,[7,18] Claudia Maraston,[7] Cameron K. McBride,[11] Olga Mena,[19] Francesco Montesano,[20] Robert C. Nichol,[7] Sebastián E. Nuza,[21] Matthew D. Olmstead,[5] Nikhil Padmanabhan,[9] Nathalie Palanque-Delabrouille,[3,22] John Parejko,[9] Will J. Percival,[7] Patrick Petitjean,[23] Francisco Prada,[8,24,25] Adrian M. Price-Whelan,[26] Beth Reid,[3,27]★ Natalie A. Roe,[3] Ashley J. Ross,[7] Nicholas P. Ross,[3,28] Cristiano G. Sabiu,[29] Shun Saito,[30] Lado Samushia,[7,31] Ariel G. Sánchez,[20] David J. Schlegel,[3]† Donald P. Schneider,[32,33] Claudia G. Scoccola,[8,34,35] Hee-Jong Seo,[16,36] Ramin A. Skibba,[37] Michael A. Strauss,[13] Molly E. C. Swanson,[11] Daniel Thomas,[7] Jeremy L. Tinker,[4] Rita Tojeiro,[7] Mariana Vargas Magaña,[2] Licia Verde,[35,38] David A. Wake,[39,40] Benjamin A. Weaver,[4] David H. Weinberg,[16,41] Martin White,[3,27,42]‡ Xiaoying Xu,[14] Christophe Yèche,[22] Idit Zehavi[43] and Gong-Bo Zhao[7,44]

Affiliations are listed at the end of the paper

Accepted 2014 March 13. Received 2014 March 12; in original form 2013 December 17

ABSTRACT

We present a one per cent measurement of the cosmic distance scale from the detections of the baryon acoustic oscillations (BAO) in the clustering of galaxies from the Baryon Oscillation Spectroscopic Survey, which is part of the Sloan Digital Sky Survey III. Our results come from the Data Release 11 (DR11) sample, containing nearly one million galaxies and covering approximately 8500 square degrees and the redshift range $0.2 < z < 0.7$. We also compare these results with those from the publicly released DR9 and DR10 samples. Assuming a concordance Λ cold dark matter (ΛCDM) cosmological model, the DR11 sample covers a volume of 13 Gpc^3 and is the largest region of the Universe ever surveyed at this density. We measure the correlation function and power spectrum, including density-field reconstruction of the BAO feature. The acoustic features are detected at a significance of over 7σ in both the correlation function and power spectrum. Fitting for the position of the acoustic features measures the distance relative to the sound horizon at the drag epoch, $r_{\rm d}$, which has a value of $r_{\rm d,fid} = 149.28$ Mpc in our fiducial cosmology. We find $D_V = (1264 \pm 25\,{\rm Mpc})(r_{\rm d}/r_{\rm d,fid})$

★ Hubble Fellow.
† BOSS PI: djschlegel@lbl.gov
‡ E-mail: mwhite@berkeley.edu

© 2014 The Authors
Published by Oxford University Press on behalf of the Royal Astronomical Society

Downloaded from http://mnras.oxfordjournals.org/ at University of California, Irvine on March 16, 2016

at $z = 0.32$ and $D_V = (2056 \pm 20\,\mathrm{Mpc})(r_\mathrm{d}/r_{\mathrm{d,fid}})$ at $z = 0.57$. At 1.0 per cent, this latter measure is the most precise distance constraint ever obtained from a galaxy survey. Separating the clustering along and transverse to the line of sight yields measurements at $z = 0.57$ of $D_\mathrm{A} = (1421 \pm 20\,\mathrm{Mpc})(r_\mathrm{d}/r_{\mathrm{d,fid}})$ and $H = (96.8 \pm 3.4\,\mathrm{km\,s^{-1}\,Mpc^{-1}})(r_{\mathrm{d,fid}}/r_\mathrm{d})$. Our measurements of the distance scale are in good agreement with previous BAO measurements and with the predictions from cosmic microwave background data for a spatially flat CDM model with a cosmological constant.

Key words: cosmological parameters – cosmology: observations – dark energy – distance scale – large-scale structure of Universe.

1 INTRODUCTION

Measuring the expansion history of the Universe has been one of the key goals of observational cosmology since its founding. To date the best constraints come from measuring the distance–redshift relation over as wide a range of redshifts as possible (Weinberg et al. 2013), and imply that the expansion rate of the Universe has recently transitioned from a deceleration to an acceleration phase (Riess et al. 1998; Perlmutter et al. 1999). While the flat Λ cold dark matter (ΛCDM) model provides a simple mathematical description of expansion that matches current observations (Planck Collaboration 2013b), it is physically perplexing given the small vacuum energy density measured, when compared with the high densities that traditionally correspond to new physics (see e.g. Weinberg et al. 2013; Mortonson, Weinberg & White 2014, for recent reviews). Understanding the physical cause of the accelerating expansion rate remains one of the most interesting problems in modern physics.

One of the most robust methods for measuring the distance–redshift relation is to use the Baryon Acoustic Oscillation (BAO) feature(s) in the clustering of galaxies as a 'standard ruler'. The acoustic oscillations arise from the tight coupling of baryons and photons in the early Universe: the propagation of sound waves through this medium gives rise to a characteristic scale in the distribution of perturbations corresponding to the distance travelled by the wave before recombination (Peebles & Yu 1970; Sunyaev & Zel'dovich 1970; Doroshkevich, Zel'dovich & Sunyaev 1978; a description of the physics leading to the features can be found in Eisenstein & Hu 1998 or appendix A of Meiksin, White & Peacock 1999 and a discussion of the acoustic signal in configuration space can be found in Eisenstein, Seo & White 2007a). This signal is imprinted in the distribution of both the matter and the radiation. The latter are seen as anisotropies in the cosmic microwave background (CMB) radiation while the former are the signal of interest here. The distance that sound waves travel before the coupling between baryons and radiation breaks down, known as the acoustic scale, is quite large, $r_\mathrm{d} \approx 150\,\mathrm{Mpc}$. The signal therefore relies on simple, linear, well-understood physics that can be well calibrated by CMB anisotropy measurements and is quite insensitive to non-linear or astrophysical processing that typically occurs on much smaller scales. This makes experiments using the BAO signal relatively free of systematic errors.

A number of experiments have used the BAO technique to measure the distance–redshift relationship. The strongest early detections were with galaxies at low redshift (Cole et al. 2005; Eisenstein et al. 2005; Hutsi 2006; Tegmark et al. 2006; Percival et al. 2007), though BAO have now also been detected in the distribution of clusters (Veropalumbo et al. 2014), and at higher redshift using the Lyman α forest in quasar spectra (Busca et al., 2013; Kirkby et al. 2013; Slosar et al. 2013) and cross-correlation between quasars and the Lyman α forest (Font-Ribera et al. 2013). A review of BAO measurements was provided in Anderson et al. (2012), which described recent experiments (e.g. the 6dFGRS, WiggleZ and SDSS; Beutler et al. 2011; Blake et al. 2011; Padmanabhan et al. 2012), and presented the first set of analyses of the galaxies in Data Release 9 of the Baryon Oscillation Spectroscopic Survey (BOSS; Dawson et al. 2012), part of the Sloan Digital Sky Survey III (SDSS III; Eisenstein et al. 2011).

In Anderson et al. (2012), we used reconstruction to provide a 1.7 per cent distance measurement from the BOSS DR9 galaxies, the most precise measurement ever obtained from a galaxy survey. This measurement benefitted from a simple reconstruction procedure, which used the phase information within the density field to reconstruct linear behaviour and sharpen the BAO (Eisenstein et al. 2007b). In Anderson et al. (2014), we fitted moments of the anisotropic correlation function measured from the same data, providing distance constraints split into radial and anisotropic directions. We now extend and update the BAO measurements based on the BOSS galaxy samples to the latest data set from the ongoing BOSS.

This paper concentrates on the DR11 data set, comprised of SDSS-III observations through 2013 May, which is scheduled for public release in 2014 December together with the final SDSS-III Data Release (DR12). The DR10 data set, comprised of observations through 2012 June, is already public (Ahn et al. 2014). We provide the DR10 large-scale structure samples, including the masks, weights, and random catalogues needed for clustering analyses, through the SDSS-III Science Archive Server. To facilitate community comparisons to our results, in this paper we also present several of our key analyses for the DR10 subset of our data sample.

Five companion papers present extensions to the methodology, testing, and data sets beyond those applied previously to the DR9 data:

(i) Ross et al. (2014) split the DR10 CMASS sample (see Section 2) into red and blue galaxies, showing that consistent cosmological measurements result from both data sets.

(ii) Vargas-Magana et al. (2013) investigate the different possible systematics in the anisotropic fitting methodologies, showing that we achieve unbiased results with fiducial fitting methodology.

(iii) Manera et al. (2014) describe the production of mock catalogues, used here to determine errors and test our analysis methods.

(iv) Percival et al. (2014) present a method to propagate errors in the covariance matrices determined from the mocks through to errors on the final measurements.

(v) Tojeiro et al. (2014) present measurements made at $z = 0.32$ from the low-redshift 'LOWZ' BOSS sample of galaxies which we now include in our constraints.

We also have produced a series of companion papers presenting complementary cosmological measurements from the DR10 and DR11 data:

Downloaded from http://mnras.oxfordjournals.org/ at University of California, Irvine on March 16, 2016

(i) Beutler et al. (2013) present a fit to the CMASS power spectrum monopole and quadrupole, measuring redshift-space distortions (RSD).

(ii) Samushia et al. (2014) fit the CMASS correlation function monopole and quadrupole, measuring RSD using a streaming model.

(iii) Chuang et al. (2013b) fit CMASS correlation function monopole and quadrupole using quasi-linear scales (e.g. above $50\,h^{-1}$ Mpc) to extract single-probe measurements. For the LOWZ sample, they include smaller scales with Finger-of-God (FoG) modelling.

(iv) Sánchez et al. (2013b) fit LOWZ and CMASS correlation function monopole and wedges (Kazin, Sanchez & Blanton 2012) with a model inspired by renormalized perturbation theory.

The layout of this paper is as follows. We introduce the data and the catalogue in the next section. The catalogue construction is similar to that described in Anderson et al. (2012) for DR9, and so we focus primarily on the differences and improvements in Section 3. We present the analysis methods for our isotropic and anisotropic measurements in Sections 4 and 5, respectively. We then present the isotropic results in Section 6 and the anisotropic results in Section 7. Our systematic error assessment and final distance measurements are presented in Section 8 and these measurements are placed in a cosmological context in Section 9. We conclude in Section 10.

Throughout the paper, we assume a fiducial ΛCDM+GR, flat cosmological model with $\Omega_{\rm m} = 0.274$, $h = 0.7$, $\Omega_{\rm b}\,h^2 = 0.0224$, $n_{\rm s} = 0.95$ and $\sigma_8 = 0.8$, matching that used in Anderson et al. (2012, 2014). Note that this model is different from the current best-fitting cosmology; however, these parameters allow us to translate angles and redshifts into distances and provide a reference against which we measure distances. The BAO measurement allows us to constrain changes in the distance scale relative to that predicted by this fiducial model.

2 THE DATA

2.1 SDSS-III BOSS

We use data included in Data Releases 10 (DR10; Ahn et al. 2014) and 11 (DR11; to be publicly released with the final BOSS data set) of the SDSS (York et al. 2000). Together, SDSS I, II (Abazajian et al. 2009), and III (Eisenstein et al. 2011) used a drift-scanning mosaic CCD camera (Gunn et al. 1998) to image over one third of the sky (14 555 square degrees) in five photometric bandpasses (Fukugita et al. 1996; Smith et al. 2002; Doi et al. 2010) to a limiting magnitude of $r \simeq 22.5$ using the dedicated 2.5-m Sloan Telescope (Gunn et al. 2006) located at Apache Point Observatory in New Mexico. The imaging data were processed through a series of pipelines that perform astrometric calibration (Pier et al. 2003), photometric reduction (Lupton et al. 2001), and photometric calibration (Padmanabhan et al. 2008). All of the imaging was re-processed as part of SDSS Data Release 8 (DR8; Aihara et al. 2011).

BOSS is designed to obtain spectra and redshifts for 1.35 million galaxies over a footprint covering 10 000 square degrees. These galaxies are selected from the SDSS DR8 imaging and are being observed together with 160 000 quasars and approximately 100 000 ancillary targets. The targets are assigned to tiles of diameter 3° using a tiling algorithm that is adaptive to the density of targets on the sky (Blanton et al. 2003). Spectra are obtained using the double-armed BOSS spectrographs (Smee et al. 2013). Each observation is performed in a series of 900-s exposures, integrating until a minimum signal-to-noise ratio is achieved for the faint galaxy targets. This ensures a homogeneous data set with a high-redshift completeness of more than 97 per cent over the full survey footprint. Redshifts are extracted from the spectra using the methods described in Bolton et al. (2012). A summary of the survey design appears in Eisenstein et al. (2011), and a full description, including a discussion of the motivation for the targeting criteria, is provided in Dawson et al. (2012).

2.2 Galaxy catalogues

BOSS selects two classes of galaxies to be targeted for spectroscopy using SDSS DR8 imaging. The 'LOWZ' algorithm is designed to select red galaxies at $z < 0.45$ from the SDSS DR8 imaging data via

$$r_{\rm cmod} < 13.5 + c_{\parallel}/0.3 \quad (1)$$

$$|c_{\perp}| < 0.2 \quad (2)$$

$$16 < r_{\rm cmod} < 19.6 \quad (3)$$

$$r_{\rm psf} - r_{\rm mod} > 0.3, \quad (4)$$

where i and r indicate magnitudes and all magnitudes are corrected for Galactic extinction (via the Schlegel, Finkbeiner & Davis 1998 dust maps), the subscript psf denotes PSF magnitudes, the subscript mod denotes 'model' magnitudes (Stoughton et al. 2002), the subscript cmod denotes 'cmodel' magnitudes (Abazajian et al. 2004), and

$$c_{\parallel} = 0.7\,(g_{\rm mod} - r_{\rm mod}) + 1.2\,(r_{\rm mod} - i_{\rm mod} - 0.18) \quad (5)$$

and

$$c_{\perp} = r_{\rm mod} - i_{\rm mod} - (g_{\rm mod} - r_{\rm mod})/4.0 - 0.18. \quad (6)$$

The resulting LOWZ galaxy sample has three times the spatial density of the SDSS-II LRGs, as is shown in Fig. 1, with a similar clustering amplitude to the CMASS sample (Parejko et al. 2013).

We define the effective redshift, $z_{\rm eff}$, as the mean redshift of a sample weighted by the number of galaxy pairs with separations

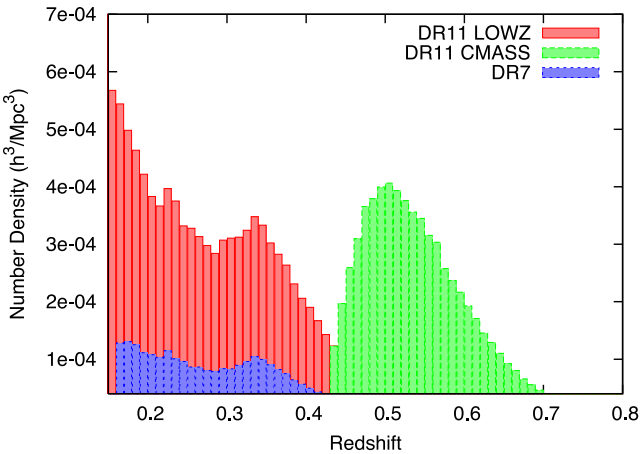

Figure 1. Histograms of the galaxy number density as a function of redshift for LOWZ (red) and CMASS (green) samples we analyse. We also display the number density of the SDSS-II DR7 LRG sample in order to illustrate the increase in sample size provided by BOSS LOWZ galaxies.

Downloaded from http://mnras.oxfordjournals.org/ at University of California, Irvine on March 16, 2016

$80 < s < 120\,h^{-1}$ Mpc. For the LOWZ sample $z_{\rm eff} = 0.32$, slightly lower than that of the SDSS-II LRGs as we place a redshift cut $z < 0.43$ to ensure no overlap with the CMASS sample, and hence independent measurements. Further details can be found in Parejko et al. (2013) and Tojeiro et al. (2014). Due to difficulties during the early phases of the project, the sky area of the LOWZ sample lags that of the full survey by approximately 1000 deg^2, as can be seen in comparison of Tables 1 and 2.

The CMASS sample is designed to be approximately stellar-mass-limited above $z = 0.45$. These galaxies are selected from the SDSS DR8 imaging via

$$17.5 < i_{\rm cmod} < 19.9 \quad (7)$$

$$r_{\rm mod} - i_{\rm mod} < 2 \quad (8)$$

$$d_\perp > 0.55 \quad (9)$$

$$i_{\rm fib2} < 21.5 \quad (10)$$

$$i_{\rm cmod} < 19.86 + 1.6(d_\perp - 0.8), \quad (11)$$

where

$$d_\perp = r_{\rm mod} - i_{\rm mod} - (g_{\rm mod} - r_{\rm mod})/8.0, \quad (12)$$

and i_{fib2} is the i-band magnitude within a 2 arcsec aperture radius.

For CMASS targets, stars are further separated from galaxies by only keeping objects with

$$i_{\rm psf} - i_{\rm mod} > 0.2 + 0.2(20.0 - i_{\rm mod}) \quad (13)$$

$$z_{\rm psf} - z_{\rm mod} > 9.125 - 0.46\,z_{\rm mod}, \quad (14)$$

unless the target also passes the LOWZ cuts (equations 1– 4) listed above.

The CMASS selection yields a sample with a median redshift $z = 0.57$ and a stellar mass that peaks at $\log_{10}(M/{\rm M}_\odot) = 11.3$ (Maraston et al. 2013) and a (stellar) velocity dispersion that peaks at 240 km s^{-1} (Bolton et al. 2012; Thomas et al. 2013). Most CMASS targets are central galaxies residing in dark matter haloes of $\sim 10^{13}\,h^{-1}\,{\rm M}_\odot$, but a non-negligible fraction are satellites that live primarily in haloes about 10 times more massive (White et al. 2011; Nuza et al. 2013). Further discussion can be found in Tojeiro et al. (2012). Kinematics and emission line properties are described in Thomas et al. (2013).

Target lists are produced using these algorithms and are then 'tiled' to produce lists of galaxies to be observed with a single pointing of the Sloan telescope. Not all targets can be assigned fibres, and not all that are result in a good redshift measurement. In fact, there are three reasons why a targeted galaxy may not obtain a BOSS spectrum:

(i) SDSS-II already obtained a good redshift for the object; these are denoted *known*.

Table 1. Basic properties of the CMASS target class and corresponding mask as defined in the text.

	DR10			DR11		
Property	NGC	SGC	Total	NGC	SGC	total
$N_{\rm targ}$	479 625	137 079	616 704	630 749	212 651	843 400
$N_{\rm gal}$	420 696	119 451	540 147	556 896	186 907	743 803
$N_{\rm known}$	7338	1520	8858	10044	1675	11 719
$N_{\rm star}$	11 524	3912	15 436	13 506	6348	19 854
$N_{\rm fail}$	7150	2726	9876	9059	4493	13 552
$N_{\rm cp}$	25 551	6552	32 103	33 157	9427	42 584
$N_{\rm missed}$	7366	2918	10 284	8087	3801	11 888
$N_{\rm used}$	392 372	109 472	501 844	520 805	170 021	690 826
$N_{\rm obs}$	439 370	126 089	565 459	579 461	197 748	777 209
Total area / deg^2	5185	1432	6617	6769	2207	8976
Veto area / deg^2	293	58	351	378	100	478
Used area / deg^2	4892	1375	6267	6391	2107	8498
Effective area / deg^2	4817	1345	6161	6308	2069	8377

Table 2. Basic properties of the LOWZ target class and corresponding mask as defined in the text.

	DR10			DR11		
Property	NGC	SGC	Total	NGC	SGC	total
$N_{\rm targ}$	220 241	82 952	303 193	302 679	129 124	431 803
$N_{\rm gal}$	113 624	67 844	181 468	156 569	108 800	265 369
$N_{\rm known}$	89 989	8959	98 948	124 533	11 639	136 172
$N_{\rm star}$	804	523	1327	944	754	1698
$N_{\rm fail}$	477	278	755	726	497	1223
$N_{\rm cp}$	8199	2928	11 127	10 818	4162	14 980
$N_{\rm missed}$	7148	2420	9568	9089	3272	12 361
$N_{\rm used}$	157 869	61 036	218 905	219 336	94 444	313 780
$N_{\rm obs}$	114 905	68 645	183 550	158 239	110 051	268 290
Total area / deg^2	4205	1430	5635	5793	2205	7998
Veto area / deg^2	252	58	309	337	99	436
Used area / deg^2	3954	1372	5326	5456	2106	7562
Effective area / deg^2	3824	1332	5156	5291	2051	7341

Downloaded from http://mnras.oxfordjournals.org/ at University of California, Irvine on March 16, 2016

(ii) A target of different type (e.g., a quasar) is within 62 arcsec; these are denoted *missed*.

(iii) another target of the same type is within 62 arcsec; these are denoted cp for 'close pair'.

The second and third conditions correspond to hardware constraints on the closest that two fibres can be placed on a plate. In regions where plates overlap, observations of close pairs are achieved. There are two reasons why a spectrum might not result in a good redshift measurement:

(i) The spectrum reveals that the object is a star (i.e. it was not properly classified by the imaging data and targeted as a galaxy); denoted *star*.

(ii) The pipeline fails to obtain a good redshift determination from the spectrum. These are denoted *fail*.

The numbers of targets over the sky-region used in our analyses that fall into these categories are given in Table 1 for CMASS and Table 2 for LOWZ. We also report $N_{\rm gal}$, the total number of galaxies with good BOSS spectra, and $N_{\rm used}$, the subset of $N_{\rm gal} + N_{\rm known}$ that pass our redshift cuts. As in Anderson et al. (2012), missed close pairs and redshift failures are accounted for by up-weighting the nearest target of the same target class with a successful spectral identification/redshift (regardless of its category). The LOWZ sample is then cut to $0.15 < z < 0.43$ and the CMASS sample is cut to $0.43 < z < 0.7$ to avoid overlap, and to make the samples independent. The regions of sky included for the DR10 and DR11 samples are described in the next section. In order to provide results that use the largest publicly available BOSS data sets, we analyse both the DR10 and DR11 samples throughout this paper.

2.3 Masks

We use the MANGLE software (Swanson et al. 2008) to track the areas covered by the BOSS survey and the angular completeness of each distinct region. The mask is constructed of spherical polygons, which form the base unit for the geometrical decomposition of the sky. The angular mask of the survey is formed from the intersection of the imaging boundaries (expressed as a set of polygons) and spectroscopic sectors (areas of the sky covered by a unique set of spectroscopic tiles, see Blanton et al. 2003; Tegmark et al. 2004; Aihara et al. 2011). In each sector, we determine an overall completeness

$$C_{\rm BOSS} = \frac{N_{\rm obs} + N_{\rm cp}}{N_{\rm targ} - N_{\rm known}}, \tag{15}$$

where N is the number of objects in the sector, obs denotes observed and targ denotes target. We discard any sectors where $C_{\rm BOSS} < 0.7$. We define the redshift completeness

$$C_{\rm red} = \frac{N_{\rm gal}}{N_{\rm obs} - N_{\rm star}} \tag{16}$$

and discard any sector with $C_{\rm red} < 0.8$. Further details can be found in Anderson et al. (2012), which defined and applied these same two masking choices.

In addition to tracking the outline of the survey region and the position of the spectroscopic plates, we apply several 'vetos' in constructing the catalogue. Regions were masked where the imaging was unphotometric, the PSF modelling failed, the imaging reduction pipeline timed out (usually due to too many blended objects in a single field), or the image was identified as having critical problems in any of the five photometric bands. We mask the small regions around the centre posts of the plates, where fibres cannot be placed due to physical limitations and also around bright stars in the Tycho catalogue (Høg et al. 2000), with area given by equation 9 of Anderson et al. (2012). We also place a mask at the locations of objects with higher priority (mostly high-z quasars) than galaxies, as a galaxy cannot be observed at a location within the fibre collision radius of these points. In total we masked ∼5 per cent of the area covered by the set of observed tiles due to our 'veto' mask.

The sky coverage of the LOWZ and CMASS galaxies is shown in Fig. 2 for both the Northern Galactic Cap (NGC) and Southern Galactic Cap (SGC). The ratio of total edge length to total area has decreased significantly with each release, and the effective area has increased from 3275 deg^2 for DR9, to 6161 deg^2, to 8377 deg^2 for the CMASS DR10 and DR11 samples, respectively. Tables 1 and 2 list the total footprint area $A_{\rm total}$, the area removed by the veto masks $A_{\rm veto}$, and the total area used $A_{\rm used} = A_{\rm total} - A_{\rm veto}$. The total effective area is the used area weighted by $C_{\rm BOSS}$.

The raw volume enclosed by the survey footprint and redshift cuts is 10 Gpc^3 for the DR11 CMASS sample and 3 Gpc^3 for the DR11 LOWZ sample, for a total of 13 Gpc^3. For these samples, we have also calculated the effective volume, summing over 200 redshift shells

$$V_{\rm eff} = \sum_i \left(\frac{\bar{n}(z_i) P_0}{1 + \bar{n}(z_i) P_0} \right)^2 \Delta V(z_i), \tag{17}$$

where $\Delta V(z_i)$ is the volume of the shell at z_i, and we assume that $P_0 = 20\,000\,h^{-3}$ Mpc^3, approximately matching the power spectrum amplitude where the BAO information is strongest. The 'holes' in the survey introduced by the veto mask are small, and are better approximated by a reduction in the galaxy density than the volume covered for the large-scale modes of interest. We therefore estimate the galaxy density $\bar{n}(z_i)$ by dividing the number of galaxies in each shell by the shell volume calculated using area $A_{\rm total}$, and the volume of each shell is estimated using area $A_{\rm total}$. For DR10, the LOWZ sample then has an effective volume of 1.7 Gpc^3, and the CMASS sample 4.4 Gpc^3. For DR11, these increase to 2.4 Gpc^3 for LOWZ and 6.0 Gpc^3 for CMASS.

2.4 Weighting galaxies

To correct for the effects of redshift failures and fibre collisions, each galaxy is given a set of weights. A galaxy is upweighted if its nearest neighbour (of the same target class) had a redshift failure ($w_{\rm zf}$) or a redshift of that neighbour was not obtained because it was in a close pair ($w_{\rm cp}$). For CMASS, we additionally apply weights to account for the systematic relationships we find between the number density of observed galaxies and stellar density and seeing (weights $w_{\rm star}$ and $w_{\rm see}$, respectively). Each galaxy is thus counted as

$$w_{\rm tot} = (w_{\rm cp} + w_{\rm zf} - 1)\, w_{\rm star}\, w_{\rm see}, \tag{18}$$

where $w_{\rm star}$ and $w_{\rm see}$ are equal to 1 for all LOWZ galaxies. In this section, we justify the application of these weights and describe how they are determined.

Ross et al. (2011) created a photometric redshift catalogue of the CMASS sample over the full DR8 area, using early BOSS redshifts as a training sample. Using this photometric redshift catalogue, Ross et al. (2011) and Ho et al. (2012) found that there exists a significant anticorrelation between the surface number density of CMASS galaxies selected from the SDSS DR8 imaging and stellar density. This relationship was found to impart spurious large-scale clustering in angular distribution of CMASS galaxies.

Downloaded from http://mnras.oxfordjournals.org/ at University of California, Irvine on March 16, 2016

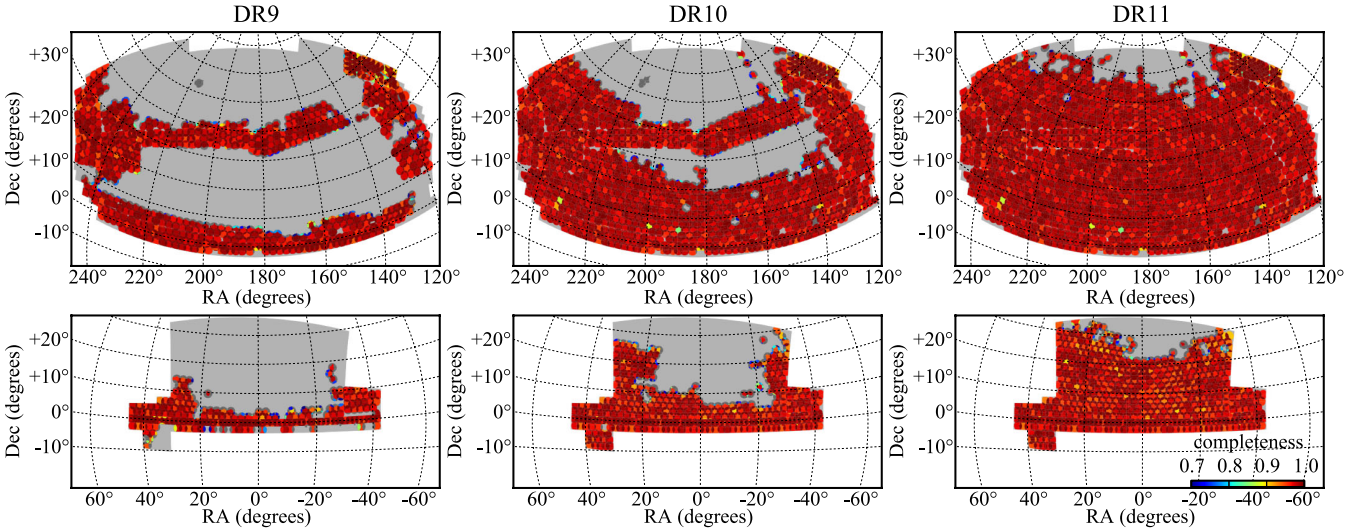

Figure 2. Evolution of the BOSS sky coverage from DR9 to DR11. Top panels show our observations in the Northern Galactic Cap (NGC) while lower panels show observations in the Southern Galactic Cap (SGC). Colours indicate the spectroscopic completeness within each sector as indicated in the key in the lower-right panel. Grey areas indicate our expected footprint upon completion of the survey. The total sky coverage in DR9, DR10, and DR11 is 3275, 6161, and 8377 deg^2, respectively.

Ross et al. (2011) and Ho et al. (2012) also found a significant anticorrelation between the number density of CMASS galaxies and seeing of the imaging data. It was found that in areas with poorer seeing, the star–galaxy separation algorithm was more restrictive inducing the observed anticorrelation. Using the same catalogue, Ho et al. (2012) derived corrections based on measurements of the galaxy–seeing cross-power and applied them to their angular power spectrum measurements, showing that the seeing impacts the measured clustering. Over the DR9 footprint, the impact of the systematic with seeing was found to be insignificant (Ross et al. 2012), as the pattern of seeing over the DR9 area has negligible large-scale power. However, the effect on clustering measured for any given footprint will scale with the pattern of seeing in that particular footprint and any impact on the DR10 and DR11 clustering measurements must be re-tested.

Ross et al. (2012) determined that weights applied to the DR9 CMASS galaxies as a function of stellar density and the $i_{\rm fib2}$ magnitude effectively removed any angular and redshift dependence of the CMASS galaxy field on the number density of stars. They found that, while a significant relationship existed between the observed density of CMASS galaxies and seeing, the relationship did not affect the measured clustering. Additional potential systematics such as Galactic extinction, airmass, and sky background were tested and the relationships were consistent with the expected angular variation in galaxy number density. No significant systematic trends were detected in the LOWZ sample.

For the DR10 and DR11 samples, we followed the same procedure as in Ross et al. (2012) to test and model the relation between the density of spectroscopically identified galaxies and stellar density, seeing, Galactic extinction, airmass and sky background. To perform these tests, we made HEALPIX (Górski et al. 2005) maps of the DR11 galaxies and compared them to maps of the number of stars with $17.5 < i < 19.9$, where i is the extinction-corrected i-band magnitude, and to maps of the mean values of the potential systematic based on data from the SDSS DR8 Catalog Archive Server, using various map resolution parameters $N_{\rm side}$.

The solid red lines of Fig. 3 show the relationships between the surface number density of galaxies in the CMASS sample, obtained after applying the completeness and close-pair corrections described above, and the stellar density (panel a), Galactic extinction (panel b), and i-band seeing (panel c). These lines systematically deviate from $n_{\rm g}/\bar{n}_g = 1$, indicating the presence of systematics affecting the galaxy distribution. The error bars in these relations were obtained by applying the same test to the mock catalogues described in Section 3.2. The systematic effect associated with the surface density of stars, $n_{\rm s}$, is clearly visible in panel (a), causing a decrease in the number of galaxies of as much as 20 per cent in regions with high stellar density. A weak relation between the observed number of galaxies and the galactic extinction can be seen in panel (b). This is due to the correlation between A_r and $n_{\rm s}$ and not to an independent systematic. Panel (c) illustrates the strong impact of poor seeing conditions on the observed galaxy number density: an i-band seeing of $S \simeq 2$ arcsec leads to a loss of approximately 50 per-cent of the galaxies. While this effect is dramatic, only 1 per cent of the survey footprint has $S > 1.6$ arcsec. The systematic relationship we find between the DR11 CMASS sample and the seeing in the imaging catalogue is consistent with relationship found in the DR9 data (Ross et al. 2012).

We use the method to determine the corrective weight for stellar density, $w_{\rm star}$, defined in Ross et al. (2012). This method weights galaxies as a function of the local stellar density and the surface brightness of the galaxy. We use the $i_{\rm fib2}$ as a measure of surface brightness and adopt a form for

$$w_{\rm star}(n_{\rm s}, i_{\rm fib2}) = A_{i_{\rm fib2}} + B_{i_{\rm fib2}} n_{\rm s}, \tag{19}$$

where $A_{i_{\rm fib2}}$ and $B_{i_{\rm fib2}}$ are coefficients to be fit empirically. To construct these weights, we divide the CMASS catalogue into five bins of $i_{\rm fib2}$, and fit the coefficients $A_{i_{\rm fib2}}$ and $B_{i_{\rm fib2}}$ in each bin so as to give a flat relation between galaxy density and $n_{\rm s}$. The stellar density map used for this task is based on a HEALPIX grid with $N_{\rm side} = 128$, which splits the sky into equal area pixels of 0.21 deg^2. This relatively coarse mask is enough to reproduce the large-scale variations of the stellar density. The values of the $A_{i_{\rm fib2}}$ and $B_{i_{\rm fib2}}$ coefficients for DR10 and DR11 are given in Table 3. The final weight $w_{\rm star}$ for a given galaxy is then computed according to the local stellar density by interpolating the binned values of the coefficients $A_{i_{\rm fib2}}$

Downloaded from http://mnras.oxfordjournals.org/ at University of California, Irvine on March 16, 2016

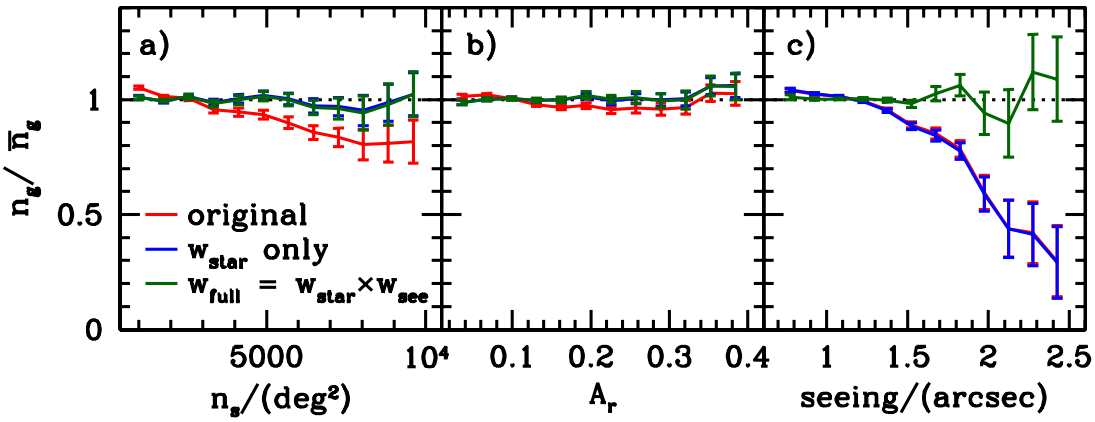

Figure 3. Dependence of the CMASS galaxy surface number density on the density of SDSS stars with $17.5 < i < 19.9$ (panel a), r-band Galactic extinction (b), and the i-band seeing of the imaging data (c). These lines deviate from $n_g = 1$, indicating the presence of systematics affecting the galaxy distribution. We correct for the systematic relationships using weights, with the relationships after applying weights shown in green. The relationship with seeing is dramatic, but only one per cent of the DR11 footprint has i-band seeing worse than 1.6 arcsec.

Table 3. The coefficients we determine to apply weights for stellar density, as defined by equation (19). The stellar density weights are determined in bins of i_{fib2} magnitude.

	DR10		DR11	
i_{fib2} range	A_{fib2}	B_{fib2}	A_{fib2}	B_{fib2}
<20.3	1.015	-6.3×10^{-6}	0.998	1.1×10^{-6}
20.320.6	0.991	3.8×10^{-6}	0.983	7.8×10^{-6}
20.620.9	0.952	2.03×10^{-5}	0.953	2.11×10^{-5}
20.921.2	0.902	4.20×10^{-5}	0.906	4.33×10^{-5}
>21.2	0.853	6.42×10^{-5}	0.870	6.06×10^{-5}

and $B_{i_{fib2}}$ to its observed i_{fib2}. The blue lines in Fig. 3 illustrate the effect of applying these weights, which correct for the systematic trend associated with n_s while leaving the relationship with the seeing unchanged, implying there is no significant correlation between the seeing and the stellar density.

Previous analyses of CMASS data (Ross et al. 2011, 2012; Ho et al. 2012) found a systematic dependence with seeing consistent with the one we find for the DR11 CMASS data. In DR9, the relationship was not found to significantly impact the measured clustering and no weight was applied. For DR11, we now find a detectable impact of the relationship with seeing on the measured clustering. We therefore extend the DR9 analyses include a weight, w_{see}, for the i-band seeing, S, defined as

$$w_{see}(S) = A_{see}\left[1 - \mathrm{erf}\left(\frac{S - B_{see}}{\sigma_{see}}\right)\right]^{-1}, \quad (20)$$

which gives a good description of the observed relation. Here, the coefficients A_{see}, B_{see}, and σ_{see} are fitted using the full sample, as opposed to bins of i_{fib2}. For this task, we use a HEALPIX map with $N_{side} = 1024$ (each pixel has an area 0.003 deg^2) as high resolution is required to sample the intricate structure of the seeing in the footprint of the survey. The green lines in Fig. 3 show the effect of applying the full weights $w_{sys} = w_{star} w_{see}$, which correct for all the observed systematic trends. To avoid applying large weights, we set w_{sys} to a constant value for $S > 2.5$ arcsec. Introducing w_{see} is necessary, as we find the pattern of seeing in the SGC has significant angular clustering and thus the systematic induces spurious clustering into SGC measurements. The w_{see} weights have negligible impact on measurements of the NGC clustering (and, indeed, the DR9 SGC clustering); there is negligible large-scale power in the pattern of the seeing in the NGC data. The best-fitting coefficients for the seeing weights we find and apply to the DR10 CMASS data are $A_{see} = 1.034$, $B_{see} = 2.086$, and $\sigma_{see} = 0.731$ and for DR11 $A_{see} = 1.046$, $B_{see} = 2.055$, and $\sigma_{see} = 0.755$. We find no trend in the relationship between galaxy density and seeing as a function of redshift. This implies that weighting based on equation (20) removes from the CMASS density field any dependence on seeing in its full 3D space.

3 ANALYSIS CHANGES COMMON TO ISOTROPIC AND ANISOTROPIC CLUSTERING SINCE DR9

We analyse the BAO feature and fit for distances using the two-point function in both configuration space (the correlation function, ξ) and in Fourier space (the power spectrum, P). In Section 4, we present the analysis techniques we use to obtain spherically averaged P and ξ and extract isotropic distance-scale measurements. In Section 5, we present the analysis techniques we use measure the distance scale along and perpendicular to the line of sight using Multipoles and Wedges in configuration space. In this section, we detail the changes common to both the isotropic and anisotropic clustering analysis since DR9. These include changes in (i) density-field reconstruction, (ii) mock catalogues, and (iii) estimation of errors on these measurements by analysing mock catalogues.

3.1 Reconstruction

The statistical sensitivity of the BAO measurement is limited by non-linear structure formation. Following Eisenstein et al. (2007b), we apply a procedure to *reconstruct* the linear density field. This procedure attempts to partially reverse the effects of non-linear growth of structure and large-scale peculiar velocities from the data. This is accomplished using the measured galaxy density field and Lagrangian theory relations between density and displacement. Reconstruction reduces the anisotropy in the clustering, reverses the smoothing of the BAO feature due to second-order effects, and significantly reduces the expected bias in the BAO distance scale that arises from these same second-order effects. Reconstruction thus improves the precision of our BAO-scale measurements while simplifying our analyses.

We apply reconstruction to both the LOWZ and CMASS samples. Briefly, we use the galaxy density field, applying an assumed bias for

Downloaded from http://mnras.oxfordjournals.org/ at University of California, Irvine on March 16, 2016

the galaxies, in order to estimate the matter density field and solve for the displacement field. A correction is applied to account for the effect of linear RSD. Full details of the reconstruction algorithm we apply can be found in Padmanabhan et al. (2012) and Anderson et al. (2012). Compared to Anderson et al. (2012), we have increased the number of points in the random catalogues used both when estimating the displacement field, and when sampling this field to give the shifted field (see Eisenstein et al. 2007b; Anderson et al. 2012; Padmanabhan et al. 2012, for definitions). Internal tests have shown that the results can be biased if the number of points in the random catalogue is too small. Given the large separation between the data in the NGC and SGC, we continue to run reconstruction on these two regions separately.

3.2 Mock catalogues

To create mock galaxy catalogues for LOWZ and CMASS samples, we use the PTHALOS methodology described in Manera et al. (2013a) assuming the same fiducial cosmology as the data analysis. The mocks reproduce the monopole and quadrupole correlation functions from the observed galaxies, and are randomly down-sampled to have the same mean $n(z)$ as a fitted 10-node spline to the sample $n(z)$. This achieves a smooth redshift distribution for the mean of the mocks. We mask each mock to the area of the observed samples, simulate close-pair completeness (fibre collisions) and randomly down-sample to the overall sky completeness based on regions defined by the specific tiling geometry of the data.

To analyse the DR10 and DR11 CMASS samples, 600 mock CMASS galaxy catalogues were used with a slightly updated method as described in Manera et al. (2014). For the LOWZ sample, 1000 mock LOWZ catalogues were created (again assuming the same fiducial cosmology) using a new incarnation of the PTHALOS methodology (Manera et al. 2014) that includes a redshift-dependent halo occupation distribution. The redshift dependence is fitted to the data based jointly on the observed clustering and the observed $n(z)$.

The analysis presented in this paper uses an earlier version of the mocks than the ones that will be publicly released in Manera et al. (2014). The differences are small and include an early estimate of the redshift distribution, a small difference in the way redshifts are assigned to random points, and lower intrahalo peculiar velocities. The mock catalogues are used to test our methodology and estimate covariance matrices. We expect these differences to have negligible statistical and systematic effects, especially when taking the approximate nature of the PTHALOS methodology into account. Our systematic error budget is discussed further in Section 9.1.

3.3 Covariance matrices

For each clustering metric we measure on the data, we also measure on the each mock galaxy catalogue. We use the distribution of values to estimate the sample covariance matrices that we use in the fitting. We use 600 mock catalogues for CMASS and 1000 for the LOWZ analysis. As the same underlying simulation was used to construct NGC and SGC versions of each mock catalogue, we carefully combine a total measurement for each mock by using NGC and SGC measurements from different boxes. The full procedure we adopted is described in detail in Percival et al. (2014), which focuses on understanding the error in the derived covariance matrix. Percival et al. (2014) also includes how we propagate errors in the covariance matrix through to the parameter errors for all results presented in this paper.

4 MEASURING ISOTROPIC BAO POSITIONS

The BAO position in spherically averaged two-point measurements is fixed by the projection of the sound horizon at the drag epoch, $r_{\rm d}$, and provides a measure of

$$D_V(z) \equiv \left[cz(1+z)^2 D_{\rm A}(z)^2 H^{-1}(z)\right]^{1/3}, \quad (21)$$

where $D_{\rm A}(z)$ is the angular diameter distance and $H(z)$ is the Hubble parameter. Matching our DR9 analysis (Anderson et al. 2012) and previous work on SDSS-II LRGs (Percival et al. 2010), we assume that the enhanced clustering amplitude along the line of sight due to RSD does not alter the relative importance of radial and angular modes when calculating spherically averaged statistics. This approximation holds best for our results including reconstruction, which are also our statistically most constraining measures. If we measure the correlation function or power spectrum using a fiducial cosmological model, denoted by a subscript fid, to convert angles and redshifts into distances, then to an excellent approximation the observed BAO position depends simply on the scale dilation parameter

$$\alpha \equiv \frac{D_V(z) r_{\rm d,fid}}{D_V^{\rm fid}(z) r_{\rm d}}, \quad (22)$$

which measures the relative position of the acoustic peak in the data versus the model, thereby characterizing any observed shift. If $\alpha > 1$, the acoustic peak is shifted towards smaller scales, and $\alpha < 1$ shifts the observed peak to larger scales. We now outline the methodology we use to measure α, tests made using mock catalogues, and how we combine results from $\xi(s)$, and $P(k)$ measurements and from different binning schemes.

4.1 Methodology

We have created separate pipelines to measure the average BAO position in the BOSS data in configuration space using the correlation function, $\xi(s)$, and in Fourier space using the power spectrum, $P(k)$. The BAO position presents as a single peak in $\xi(s)$ and an oscillation in $P(k)$.

To calculate $\xi(s)$, we use the Landy & Szalay (1993) estimator, summing pair-counts into bins of width $8\,h^{-1}$ Mpc (as discussed further in Percival et al. 2014). As a fiducial choice, the smallest s bin is centred at $6\,h^{-1}$ Mpc, but we will also obtain results for the eight binning choices shifted by increments of $1\,h^{-1}$ Mpc. For each binning, we calculate $\xi(s)$ for bin centres in the range $29 < s < 200\,h^{-1}$ Mpc (22 bins, for our fiducial choice).

To calculate $P(k)$, we use the Feldman, Kaiser & Peacock (1994) estimator. We use a Fourier grid of size 2048^3, $4000\,h^{-1}$ Mpc along each side: this comfortably encloses the survey including both the NGC and SGC components; we use with sufficient zero-padding that aliasing is not a problem which was confirmed by consistency between results from other box sizes. Compared to our DR9 analysis presented in Anderson et al. (2012), we modify our normalization to properly account for the weights of galaxies introduced to account for nearby close-pair or redshift failures. We calculate $P(k)$ in Fourier modes averaged over bin widths of $\Delta k = 0.008\,h\,{\rm Mpc}^{-1}$. Percival et al. (2014) find that this bin width minimizes the combined error when fluctuations in the covariance matrix are also included. Our fiducial choice has the smallest k-bin centred at $k = 0.004\,h\,{\rm Mpc}^{-1}$. We will also use the nine additional binning schemes that shift the bin centres by increments of $0.0008\,h\,{\rm Mpc}^{-1}$. We calculate $P(k)$ for bin centres in the range $0.02 < k < 0.3\,h\,{\rm Mpc}^{-1}$, giving 35 bins for our fiducial choice. These limits are imposed because the BAO have effectively died out for

Downloaded from http://mnras.oxfordjournals.org/ at University of California, Irvine on March 16, 2016

smaller scales, and larger scales can be sensitive to observational systematics.

We fit the measured, spherically averaged, correlation function and power spectrum separately and then combine results using the mocks to quantify the correlation coefficient between measurements. Our fits use polynomial terms to marginalize over the broad-band shape in either two-point measurement, while rescaling a model of the damped BAO to fit the data. We use slightly different template BAO models for $\xi(s)$ and $P(k)$ fits, as they enter the model functions in different ways.

To produce a template model for the $P(k)$ fit, we first compute a linear power spectrum $P^{\rm lin}$ produced by CAMB (Lewis, Challinor & Lasenby 2000). We then split into two components, one oscillatory $O^{\rm lin}$ and the other smooth $P^{\rm sm,lin}$, that return the CAMB-derived power spectrum when multiplied together. To perform the split, we fit $P^{\rm lin}$ using the same method that we use to fit to the data, but with a BAO model calculated using the fitting formulae of Eisenstein & Hu (1998). The resulting smooth model is taken to be $P^{\rm sm,lin}$, and $O^{\rm lin}$ is calculated by dividing $P^{\rm lin}$ by this. This follows the procedure used in Anderson et al. (2012).

The full model fitted to the data power spectrum is then

$$P^{\rm fit}(k) = P^{\rm sm}(k)\left[1 + (O^{\rm lin}(k/\alpha) - 1)\mathrm{e}^{-(1/2)k^2\Sigma_{\rm nl}^2}\right], \quad (23)$$

where

$$P^{\rm sm}(k) = B_{\rm P}^2 P^{\rm sm,lin}(k) + A_1 k + A_2 + \frac{A_3}{k} + \frac{A_4}{k^2} + \frac{A_5}{k^3}. \quad (24)$$

There are therefore six 'nuisance' parameters: a multiplicative constant for an unknown large-scale bias $B_{\rm P}$, and five polynomial parameters, A_1, A_2, A_3, A_4, and A_5, which marginalize over broad-band effects including RSD, scale-dependent bias, and any errors made in our assumption of the model cosmology. These effects may bias our measurement of the acoustic scale if not removed.

The damping was treated as a free parameter, with a Gaussian prior with conservative width $\pm 2\,h^{-1}$ Mpc centred at the best-fitting values recovered from the mocks: for the CMASS sample these are $\Sigma_{\rm nl} = 8.3\,h^{-1}$ Mpc pre-reconstruction and $\Sigma_{\rm nl} = 4.6\,h^{-1}$ Mpc post-reconstruction, and for LOWZ they are $\Sigma_{\rm nl} = 8.8\,h^{-1}$ Mpc pre-reconstruction and $\Sigma_{\rm nl} = 4.8\,h^{-1}$ Mpc post-reconstruction. This model, which differs from that used to fit the power spectrum in Anderson et al. (2012), is better matched to the now standard model for the correlation function (e.g. Anderson et al. 2012) that we adopt.

To fit to the correlation function, we adopt the template model for the linear correlation function given in Eisenstein et al. (2007a), with damped BAO

$$\xi^{\rm mod}(s) = \int \frac{k^2 \mathrm{d}k}{2\pi^2} P^{\rm mod}(k) j_0(ks) \mathrm{e}^{-k^2 a^2}, \quad (25)$$

where the Gaussian term has been introduced to damp the oscillatory transform kernel $j_0(ks)$ at high-k to induce better numerical convergence. The exact damping scale used in this term is not important, and we set $a = 1\,h^{-1}$ Mpc, which is significantly below the scales of interest. The power spectrum is given by

$$P^{\rm mod}(k) = P^{\rm nw}(k)\left[1 + \left(\frac{P^{\rm lin}(k)}{P^{\rm nw}(k)} - 1\right)\mathrm{e}^{-(1/2)k^2\Sigma_{\rm nl}^2}\right], \quad (26)$$

where $P^{\rm lin}(k)$ is the same model produced by CAMB, and used to create the power spectrum fit template. $P^{\rm nw}(k)$ is a model created using the no-wiggle fitting formulae of Eisenstein & Hu (1998), in which the BAO feature is erased. We refer to this template as the 'De-Wiggled' template.

Using this template, our correlation function model is given by

$$\xi^{\rm fit}(s) = B_\xi^2 \xi^{\rm mod}(\alpha s) + A^\xi(s). \quad (27)$$

where B_ξ is a multiplicative constant allowing for an unknown large-scale bias, and the additive polynomial is

$$A^\xi(s) = \frac{a_1}{s^2} + \frac{a_2}{s} + a_3, \quad (28)$$

where a_1, a_2, a_3 help marginalize over the broad-band signal.

Unlike for the power spectrum, we do not allow the damping parameter to vary and instead fix it at the average best-fittin value recovered from the mocks: the interplay between B_ξ and the additive polynomial A_ξ in our fit to $\xi(s)$ means that the amplitude of the BAO peak has more freedom already.

Apart from the differences in damping correction, the parallel between $\xi(s)$ and $P(k)$ fitting methods is clear and follows from the match between equation (23) and (26), and between equation (24) and the combination of equations (27) and (28). There are three subtle differences as follows. For the power spectrum, we only shift the BAO with the parameter α, while for $\xi(s)$ we shift the full model. As the nuisance parameters are marginalizing over the broad-band, this should have no effect. For the correlation function, the nuisance parameters are added to the final model compared to the data $\xi^{\rm fit}(s)$; for the power spectrum, they are added to the smooth model $P^{\rm sm}(k)$. This slightly changes the meaning of the BAO damping term. We also split the CAMB power spectrum into BAO and smooth components in different ways, utilizing the Eisenstein & Hu (1998) functions for the $\xi(s)$ template, whereas for the $P(k)$ fit we can applying the same fitting method to the CAMB power spectrum as used to fit the data. The effect of this is expected to be small.

For fits to both the correlation function and power spectrum, we obtain the best-fitting value of α assuming that $\xi(s)$ and $\log P(k)$ were drawn from multivariate Gaussian distributions, calculating χ^2 at intervals of $\Delta\alpha = 0.001$ in the range $0.8 < \alpha < 1.2$. Our final error on α is determined by marginalizing over the likelihood surface and then correcting for the error in the covariance matrix as described in Percival et al. (2014).

4.2 Testing on mock galaxy catalogues

We test our $\xi(s)$ and $P(k)$ isotropic BAO fitting procedure on each of our CMASS mock galaxy samples, both pre- and post-reconstruction. The results are summarized in Table 4. Tojeiro et al. (2014) presents similar tests on the LOWZ mock galaxy samples.

Overall, we find a small, positive bias in the mean recovered $\langle\alpha\rangle$ values pre-reconstruction, varying between 0.0026 (DR10 $P(k)$) and 0.0041 (DR11 $\xi(s)$). This bias is significantly reduced post-reconstruction, as expected (Eisenstein et al. 2007a; Noh, White & Padmanabhan 2009; Padmanabhan & White 2009; Mehta et al. 2011). For the post-reconstruction DR11 samples, given that the uncertainty on one realization is 0.009, the statistical (1σ) uncertainty on $\langle\alpha\rangle$ is 0.0004. The $P(k)$ and $\xi(s)$ $\langle\alpha\rangle$ results are both consistent with 1 (i.e. unbiased). This result is independent of bin size.

In general, the mean 1σ uncertainties recovered from the individual likelihood surfaces are close to the standard deviation in the recovered α. All of these values include the appropriate factors to correct for the biases imparted by using a finite number of mocks, determined using the methods described in Percival et al. (2014). The agreement between the recovered uncertainty and the standard deviation suggests that our recovered uncertainties are a fair estimation of the true uncertainty.

Downloaded from http://mnras.oxfordjournals.org/ at University of California, Irvine on March 16, 2016

Table 4. The statistics of isotropic BAO-scale measurements recovered from the mock galaxy samples. The parameter $\langle\alpha\rangle$ is the mean α value determined from 600 mock realizations of each sample, $S_\alpha = \sqrt{\langle(\alpha - \langle\alpha\rangle)^2\rangle}$ is the standard deviation of the α values, $\langle\sigma\rangle$ is the mean 1σ uncertainty on α recovered from the likelihood distribution of each realization. The 'combined' results are post-reconstruction measurements optimally combined across a set of bin centre choices based on the correlation matrix determined from the mock realizations, as described in the text.

Estimator	$\langle\alpha\rangle$	S_α	$\langle\sigma\rangle$	$\langle\chi^2\rangle$/dof
DR11				
Consensus $P(k)$+$\xi(s)$	**1.0000**	**0.0090**	**0.0088**	
Combined $P(k)$	1.0001	0.0092	0.0089	
Combined $\xi(s)$	0.9999	0.0091	0.0090	
Post-recon $P(k)$	1.0001	0.0093	0.0090	28.6/27
Post-recon $\xi_0(s)$	0.9997	0.0095	0.0097	17.6/17
Pre-recon $P(k)$	1.0037	0.0163	0.0151	27.7/27
Pre-recon $\xi_0(s)$	1.0041	0.0157	0.0159	15.7/17
DR10				
Post-recon $P(k)$	1.0006	0.0117	0.0116	28.4/27
Post-recon $\xi_0(s)$	1.0014	0.0122	0.0126	17.2/17
Pre-recon $P(k)$	1.0026	0.0187	0.0184	27.7/27
Pre-recon $\xi_0(s)$	1.0038	0.0188	0.0194	15.8/17

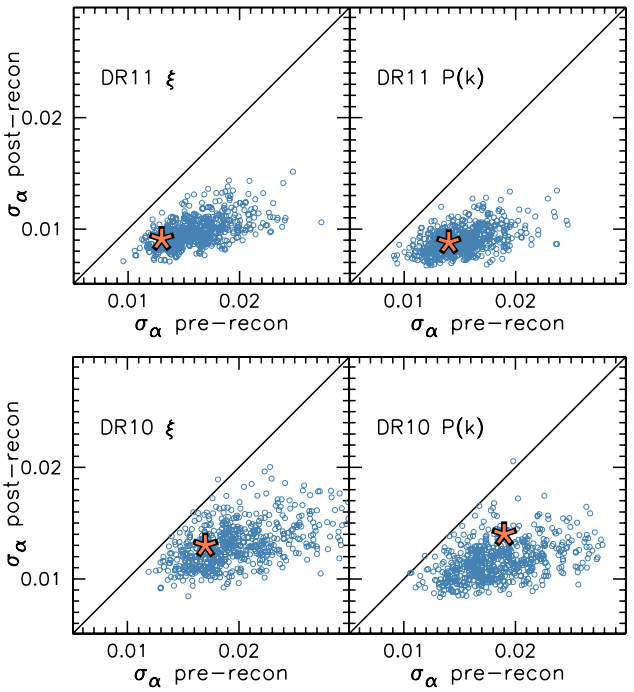

Figure 4. Scatter plots of σ_α pre- and post-reconstruction: mocks (circles) + data (star) for ξ and $P(k)$ CMASS DR10 and DR11. For the DR11 data, reconstruction improves the precision in each of the 600 mock realizations, for both $\xi(s)$ and $P(k)$.

Applying reconstruction to the mock galaxy samples improves the uncertainty in BAO fits substantially. Fig. 4 displays scatter plots of σ_α before and after reconstruction for the DR11 (top) and DR10 (bottom) samples for $\xi(s)$ (left) and $P(k)$ (right). For DR11, reconstruction reduces the uncertainty in every case. The mean improvement, determined by comparing $\langle\sigma\rangle$ pre- and post-reconstruction, is more than a factor of 1.5 in every case and is even more for the DR11 $P(k)$ results.

In summary, DR11 CMASS post-reconstruction $\xi(s)$ and $P(k)$ measurements are expected to yield estimates of the BAO scale, with statistical uncertainties that are less than 1 per cent, obtained from likelihood errors that agree with the standard deviation found in the measurements obtained from the mock samples. Furthermore, post-reconstruction, the systematic errors on the value of α measured from the mocks are consistent with zero for both correlation function and power spectrum fits, with an error on the measurement of 0.04 per cent. Section 8.1 considers possible systematic errors on our measurements in more detail.

4.3 Combining results from separate estimators

We have used $\xi(s)$ and $P(k)$ to measure the BAO scale for a number of different binning choices, with different values of bin centres and bin sizes in s and k, respectively. These do not yield perfectly correlated BAO measurements because shot noise varies within each binning choice. Each estimate is unbiased, and we can therefore combine BAO measurements using different binning schemes and different estimators, provided we take the correlation into account, which we will do using the mocks. This results in more precise measurements of the BAO scale. The dispersion in values of α that we recover from the mocks for a single choice of bin width but with different bin centres, is greater for $\xi(s)$ than for $P(k)$. There is therefore more to be gained by combining results from offset bins for our analysis of $\xi(s)$. The correlation matrices for α recovered from the 8 $\xi(s)$ and the 10 $P(k)$ bin centres tested (see Section 4.1) are displayed in Fig. 5. For $\xi(s)$, the correlation is as low as 0.89. The $P(k)$ results are more correlated, as all of the correlations are greater than 0.94. The fact that results using different bin centres are not perfectly correlated implies that an optimized α measurement can be made by calculating the weighted mean of α across all of the bin centre choices. The process we use is as follows. We find the weighted mean uncertainty, σ_b, using the correlation matrix, $\mathbf{D}$

$$\sigma_\mathrm{b} = \frac{\sum_{i,j} \sigma_i D^{-1}_{i,j}}{\sum_{i,j} D^{-1}_{i,j}}. \tag{29}$$

We then scale the elements of $\mathbf{D}$ by σ_b^2 to obtain the covariance matrix, $\mathbf{D}$, for the measurements at each bin centre. The BAO-scale measurement, α_o, and its uncertainty, $\sigma_{\alpha,\mathrm{o}}$, obtained combining the results across bin centres are then given by

$$\alpha_\mathrm{o} = \frac{\sum_{i,j} \alpha_i C^{-1}_{i,j}}{\sum_{i,j} C^{-1}_{i,j}}, \qquad \sigma^2_{\alpha,\mathrm{o}} = \frac{1}{\sum_{i,j} C^{-1}_{i,j}}. \tag{30}$$

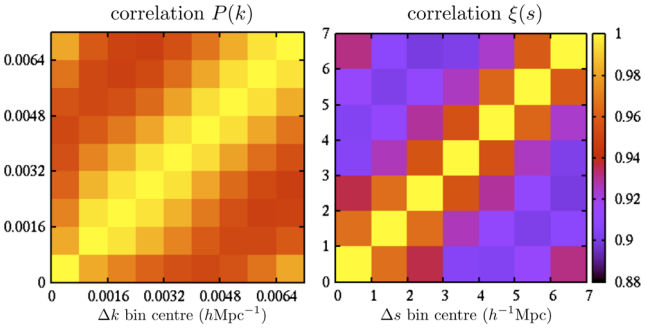

Figure 5. The correlation between recovered α values calculated using different bin centres for the DR11 CMASS reconstructed power spectrum ($P(k)$; left) and correlation function ($\xi(s)$; right). The correlation between bins is of lower amplitude for $\xi(s)$ compared with $P(k)$, implying that combining results across $\xi(s)$ bin centres will improve the precision more than doing the same for $P(k)$.

Downloaded from http://mnras.oxfordjournals.org/ at University of California, Irvine on March 16, 2016

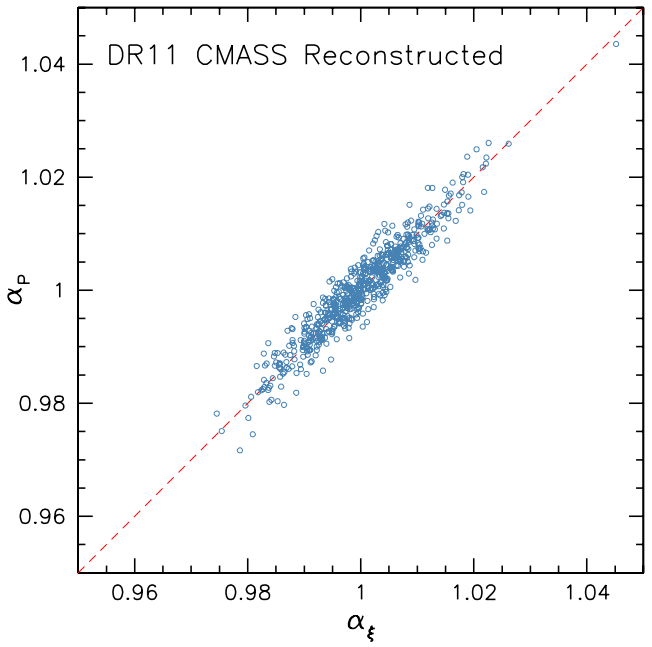

Figure 6. Scatter plot showing the measured BAO positions (α) using DR11 CMASS reconstructed mock galaxy $P(k)$ versus those obtained from $\xi(s)$ (blue circles). The measurements are strongly correlated, with $C_{P,\xi} = 0.95$ and an rms difference of 0.0027.

Applying this to $\xi(s)$ and $P(k)$ decreases the uncertainty and standard deviation such that they are nearly identical for $\xi(s)$ and $P(k)$, shown as the 'combined' results in Table 4.

The method we apply to measure the BAO position from $P(k)$ has changed from the method applied in Anderson et al. (2012); it is now more similar to the method applied to the $\xi(s)$ measurements (e.g., the smooth polynomials are similar). We combine information across bin centre choices for both fits. This results in BAO measurements that are more correlated between fits to $\xi(s)$ and $P(k)$. We use

$$C_{1,2}(X) = \frac{\sum_i^N (X_{1,i} - \langle X_1 \rangle)(X_{2,i} - \langle X_1 \rangle)}{(N-1)\sigma_1\sigma_2} \tag{31}$$

to quantify the correlation between two measures, where σ in this case represents the standard deviation of sample X. For the DR11 CMASS reconstructed mock galaxy samples, we find $C_{P,\xi}(\alpha) = 0.95$. Fig. 6 displays a scatter plot illustrating this tight correlation.

In order to combine BAO measurements from $P(k)$ and $\xi(s)$, we take $\alpha_{\xi+P}$ as the mean of the two estimates and its uncertainty as $\sigma_{\xi+P} = 0.987\bar{\sigma}$, where $\bar{\sigma}$ is the mean uncertainty of the two α estimates. This allows the uncertainty to vary for any given realization, but assumes that the uncertainty is equal and Gaussian distributed for α_P and α_ξ. The 0.987 factor is the reduction in uncertainty obtained by averaging two measurements with a 0.95 correlation factor that we identified from the mock measurements.

5 MEASURING ANISOTROPIC BAO POSITIONS

Assuming an incorrect cosmology when calculating the galaxy correlation function or power spectrum will differentially shift the BAO feature in both the transverse and line-of-sight directions. These shifts are typically parametrized by $\alpha_\perp$ and $\alpha_{||}$, which are the natural extension of the isotropic scale dilation factor α introduced in Section 4. Together, they allow us to measure the angular diameter distance (relative to the sound horizon at the drag epoch r_d) $D_A(z)/r_d$, and the Hubble parameter $H(z)$ via $cz/(H(z)r_d)$ separately through

$$\alpha_\perp = \frac{D_A(z) r_d^{fid}}{D_A^{fid}(z) r_d}, \quad \alpha_\parallel = \frac{H^{fid}(z) r_d^{fid}}{H(z) r_d}. \tag{32}$$

Another parametrization that exists in the literature decomposes the anisotropic shifts into α and an anisotropic warping factor ϵ, which can be defined in terms of $\alpha_\perp$ and $\alpha_\parallel$ as

$$\alpha = \alpha_\perp^{2/3} \alpha_\parallel^{1/3}, \quad 1 + \epsilon = \left(\frac{\alpha_\parallel}{\alpha_\perp}\right)^{1/3}. \tag{33}$$

Note that in the fiducial cosmology, $\alpha = \alpha_\perp = \alpha_\parallel = 1$ and $\epsilon = 0$. In this paper, we concentrate on $\alpha_\parallel$ and $\alpha_\perp$, but there are discussions that use α and ϵ parametrization for the ease of explanation. In particular, we use α–ϵ and $\alpha_\parallel$–$\alpha_\perp$ interchangeably for multipoles as we can convert one to another parametrization easily. Note that the α measured through anisotropic clustering is in theory the same as α measured using isotropic clustering. However, there can be a small amount of scatter between the two measured α.

We have developed separate pipelines using either multipoles of the correlation function, or top-hat windows in μ (called wedges Kazin et al. 2012), to estimate $\alpha_\parallel$ and $\alpha_\perp$. We now outline the methodology behind each pipeline and present the results of tests on both using mock data.

5.1 Methodology

For the CMASS data, we measure the average BAO position in configuration space using moments of the correlation function, $\xi(s, \mu)$, where μ is the cosine of the angle between a galaxy pair (we use the mid-point of the two galaxy positions in redshift space) and the line of sight. We use the CMASS galaxy catalogue only and we do not do an anisotropic Fourier space analysis in this paper (see Beutler et al. 2013, for a complementary analysis). We measure $\xi(s, \mu)$ using the Landy & Szalay (1993) estimator, with radial bins of width $8\,h^{-1}$ Mpc and angular bins of $\Delta\mu = 0.01$ (see Vargas-Magana et al. 2013; Percival et al. 2014 for the effect of bin-sizes on the measurement). We then project the μ-dependence to obtain both 'multipoles'

$$\xi_\ell(s) = \frac{2\ell+1}{2} \int_{-1}^{1} d\mu\, \xi(s,\mu) L_\ell(\mu), \tag{34}$$

and 'wedges'

$$\xi_{\Delta\mu}(s) = \frac{1}{\Delta\mu} \int_{\mu_{min}}^{\mu_{min}+\Delta\mu} d\mu\, \xi(s,\mu). \tag{35}$$

Throughout we shall denote the Legendre polynomial of the order of ℓ as L_ℓ, since P_ℓ will be reserved for moments of the power spectrum. As wedges and multipoles are alternative projections of $\xi(s, \mu)$, we expect similar constraints from both. We perform both analyses principally as a test for systematic errors.

For both cases, we only measure and fit to two projections. For the multipoles, we use $\ell = 0$ and 2. In linear theory, there is information in the $\ell = 4$ multipole as well, and beyond linear theory there is information in all even multipoles, but we do not include the higher multipoles as the increase in signal-to-noise ratio is small compared to the increase in modelling complexity. Furthermore, after reconstruction, the effect of RSD is significantly reduced, decreasing the information in $\ell \geq 4$ further. For the wedges, we

Downloaded from http://mnras.oxfordjournals.org/ at University of California, Irvine on March 16, 2016

choose $\Delta\mu = 0.5$ such that we have a bin which is primarily 'radial', $\xi_{\parallel}(s) \equiv \xi(s,\ \mu > 0.5)$, and a bin which is primarily 'transverse', $\xi_{\perp}(s) \equiv \xi(s,\ \mu < 0.5)$. This matches the methodology adopted for the anisotropic DR9 BAO measurements presented in Anderson et al. (2014).

We model the moments of the correlation function as the transform of

$$P(k,\ \mu) = (1 + \beta\mu^2)^2 F(k,\ \mu,\ \Sigma_{\rm s}) P_{\rm pt}(k,\ \mu)\,, \tag{36}$$

where

$$F(k,\ \mu,\ \Sigma_{\rm s}) = \frac{1}{(1 + k^2\mu^2\Sigma_{\rm s}^2/2)^2}\,, \tag{37}$$

is a streaming model for the FoG effect (Peacock & Dodds 1994) and $\Sigma_{\rm s}$ is the streaming scale, which we set to $3\,h^{-1}$ Mpc. This choice of the streaming scale has been tested in Xu et al. (2012b), Anderson et al. (2014) and Vargas-Magana et al. (2013). The $(1 + \beta\mu^2)^2$ term is the linear theory prediction for RSD at large scales (Kaiser 1987). In linear theory, $\beta = f/b \simeq \Omega_{\rm m}^{0.55}/b$, where f is the linear growth rate, but we treat β as a parameter which we vary in our fits. This allows for modulation of the quadrupole amplitude, as β is degenerate with any quadrupole bias. To exclude unphysical values of β, we a impose a prior. This prior is discussed further in Section 5.2 and its effects tested in Section 7.3. We take $P_{\rm pt}$ to be

$$P_{\rm pt}(k) = P_{\rm lin}(k) {\rm e}^{-k^2\sigma_v^2} + A_{\rm MC} P_{\rm MC}(k)\,, \tag{38}$$

where the $P_{\rm MC}$ term includes some of the non-linearities to second order, and is given by (Goroff et al. 1986; Makino, Sasaki & Suto 1992; Jain & Bertschinger 1994)

$$P_{\rm MC} = 2 \int \frac{{\rm d}^3 q}{(2\pi)^3}\, |F_2(k - q,\ q)|^2 P_{\rm lin}(|k - q|) P_{\rm lin}(q)\,, \tag{39}$$

with F_2 given by equation (45) of the review of Bernardeau et al. (2002) or the references above. The parameter σ_v accounts for the damping of the baryonic acoustic feature by non-linear evolution and $A_{\rm MC}$ for the induced coupling between Fourier modes. We fit to the mocks with these parameters free and use the mean value of the best-fitting pre-reconstruction and post-reconstruction. In particular, σ_v is fixed to $4.85(1.9)\,h^{-1}$ Mpc and $A_{\rm MC}$ is fixed to 1.7(0.05) pre(post)-reconstruction.

The template of equation (38) is different from the one used in Anderson et al. (2014) and from the non-linear template used in Section 4. The isotropic fitting in both configuration and Fourier space used the 'De-Wiggled' template (equation 26), while we use $P_{\rm pt}$, inspired by renormalized perturbation theory. This template was previously used by Kazin et al. (2013) in the analysis of the CMASS DR9 multipoles and clustering wedges and is described in more detail in Sánchez et al. (2013a).

We then decompose the full 2D power spectrum into its Legendre moments:

$$P_\ell(k) = \frac{2\ell + 1}{2} \int_{-1}^{1} P(k,\ \mu) L_\ell(\mu) {\rm d}\mu \tag{40}$$

using $P(k,\ \mu)$ from equation (36), which can then be transformed to configuration space using

$$\xi_\ell(s) = i^\ell \int \frac{{\rm d}k}{k}\, \frac{k^3 P_\ell(k)}{2\pi^2}\, j_\ell(ks), \tag{41}$$

where $j_\ell(ks)$ is the ℓth spherical Bessel function.

Similar to the isotropic BAO fitting procedure (Section 4), we use polynomial terms to marginalize over the broad-band shape for both multipoles and wedges. The model multipoles, $\xi^{\rm m}_{0,2}(s)$, and projections, $\xi^{\rm m}_{\perp,\parallel}(s)$, are defined by our template evaluated for the fiducial cosmology. The model fit to the observed multipoles is then

$$\begin{aligned}
\xi_0^{\rm fit}(s) &= B_{\xi,0}^2 \xi_0^{\rm m}(\alpha, \epsilon, s) + A_0^\xi(s)\,,\\
\xi_2^{\rm fit}(s) &= \xi_2^{\rm m}(\alpha, \epsilon, s) + A_2^\xi(s)\,,
\end{aligned} \tag{42}$$

and to the observed wedges is

$$\begin{aligned}
\xi_\perp^{\rm fit}(s) &= B_{\xi,\perp}^2 \xi_\perp^{\rm m}(\alpha_\perp, \alpha_\parallel, s) + A_\perp^\xi(s)\,,\\
\xi_\parallel^{\rm fit}(s) &= r^2 B_{\xi,\perp}^2 \xi_\parallel^{\rm m}(\alpha_\perp, \alpha_\parallel, s) + A_\parallel^\xi(s)\,,
\end{aligned} \tag{43}$$

where Xu et al. (2012b) describe how to include α and ϵ in the template $\xi^{\rm m}_{0,2}$ and Kazin et al. (2013) describe the equivalent methodology for $\xi^{\rm m}_{\parallel,\perp}$. The parameters B_ξ are bias factors that rescale the amplitude of the input models, while r regulates the amplitude ratio of the two wedges. The polynomial terms

$$A_\ell(s) = \frac{a_{\ell,1}}{s^2} + \frac{a_{\ell,2}}{s} + a_{\ell,3};\quad \ell = 0, 2, \parallel, \perp\,, \tag{44}$$

are used to marginalize out broad-band (shape) information that contributes to $\xi_\ell(s)$ due to, e.g., scale-dependent bias or RSD.

In order to find the best-fitting values of $\alpha_\parallel$ and $\alpha_\perp$, we assume that the correlation function moments are drawn from a multivariate Gaussian distribution with a covariance matrix derived from our mocks (Manera et al. 2014), corrected as summarized in Section 3.3. We fit to 40 points over the range $45 < s < 200\,h^{-1}$ Mpc, including both the monopole and the quadrupole or the two wedges. Since there are 10 parameters in our fitting model, this gives 30 degrees of freedom in the fit.

In our analysis of the wedges, we use a Markov chain Monte Carlo (MCMC) to explore the parameter space

$$\theta = (\alpha_\perp, \alpha_\parallel, B_{\xi,\perp}, r, a_{i,\perp}, a_{i,\parallel}). \tag{45}$$

We impose flat priors in all these parameters and obtain our constraints on $\alpha_\perp$ and $\alpha_\parallel$ by marginalizing over all the remaining parameters.

In our analysis of the multipoles, we explore the parameter space by calculating the likelihood surface over a large grid of α and ϵ with $\Delta\alpha = 0.003$, and $\Delta\epsilon = 0.006$.[1] Before performing the fit, we normalize the model to the data at $s = 50\,h^{-1}$ Mpc and hence $B_\xi^2 \sim 1$. As mentioned previously, we allow β to vary in our fits but apply two priors:

(i) Gaussian prior on $\log(B_\xi^2)$ centred on 1, with standard deviation of 0.4.

(ii) Gaussian prior on β with a standard deviation of 0.2. The central value is set to $f/b \sim \Omega_{\rm m}^{0.55}(z)/b = 0.4$ pre-reconstruction, and zero post-reconstruction (Xu et al. 2012b).

For each grid point, (α,ϵ), we fit the remaining parameters to minimize the χ^2. Assuming the likelihood surface is Gaussian allows us to estimate the uncertainties of α and ϵ as the standard deviations of the marginalized 1D likelihoods (for more details, see Xu et al. 2012b and Vargas-Magana et al. 2013). The deviations are computed by integrating the likelihood surface over $\alpha = [0.8, 1.2]$ and $\epsilon = [-0.2, 0.2]$. We do however use an expanded likelihood surface covering a wider range of α and ϵ as input for measuring cosmological parameters, so the chosen integration intervals do not

[1] We have tested the effect of grid size on σ_α and σ_ϵ and have verified that finer grids results in no difference to the errors recovered (Vargas-Magana et al. 2013).

Downloaded from http://mnras.oxfordjournals.org/ at University of California, Irvine on March 16, 2016

have any effect on the downstream cosmological analysis. We test the effect of each of these priors in Section 5.2. We can then easily convert any (α,ϵ) to ($\alpha_{\parallel}$,$\alpha_{\perp}$).

5.2 Testing on mock galaxy catalogues

We test our anisotropic BAO fitting procedure with both multipoles and wedges, pre- and post-reconstruction using mock catalogues. The results are summarized in Table 5. We list the median values of the recovered $\alpha_{||}$, $\alpha_{\perp}$, $\sigma_{||}$, and $\sigma_{\perp}$ from all the mock galaxy samples. Pre-reconstruction, we find that there is a small positive bias (0.006) in the median $\alpha_{\parallel}$ using multipoles and a small negative bias (−0.004) when using wedges. The signs of biases are reversed for $\alpha_{\perp}$, as (again pre-reconstruction) there is a small negative bias (−0.003) for multipoles and a small positive bias (0.001) for wedges. Reconstruction reduces the bias. Post-reconstruction, the largest bias is 0.003 for the median multipole $\alpha_{\parallel}$. The others are all $\leq$0.001. Finally, we note that both the standard deviation of the α and the median of their errors are very consistent. The uncertainties are also significantly larger than the biases on α (the bias is at most 11 per cent of the uncertainty on α) for both methods.

Anderson et al. (2014) and Kazin et al. (2013) describe detailed tests applied to the 'Wedges' technique. Given the high degree of correlation between wedge- and multipole-based measurements and fitting methodology of multipoles has changed slightly since Anderson et al. (2014), here we focus on tests based on multipoles.

We tested the robustness of our fits to a number of parameter choices, including the following:

(i) changing fitting ranges;
(ii) changing the number of nuisance parameters, $A_{\ell}(r)$;
(iii) changing the priors on B_0 and β.

The results of these and further tests are extensively detailed in Vargas-Magana et al. (2013). Here, we only highlight the specific findings that are pertinent to this analysis (see Table 6). None of the tests resulted in significantly biased values for the best-fitting parameters or their associated errors. In particular, the best-fitting values of α do not vary by more than 0.2 per cent for all cases, and most of the best-fitting values of ϵ do not vary by more than 0.3 per cent. It is particularly interesting to note that the median errors of both α and ϵ do not change at all for all of the different fitting parameter choices. Note that this is not true if we extend the range of α and ϵ over which we integrate to make these measurements. By design, the priors act to exclude unphysical models, which otherwise can affect the measured errors. However, the likelihood close to the best-fitting solution is not affected by these priors, and hence, the best-fitting values and errors are not affected.

Finally, we further test our Multipoles method by looking at the error on both $\alpha_{||}$ and $\alpha_{\perp}$ for all of our mock galaxy samples (blue points), and compare it to our data in DR10 and DR11 (orange stars). We show in Fig. 7 that reconstruction decreases the uncertainty on $\alpha_{\perp}$ and $\alpha_{\parallel}$ in the vast majority of the 600 mock galaxy samples. This is especially true for $\alpha_{\perp}$. The DR10 footprint is less contiguous than the DR11 one and there are thus more outliers in DR10 than in DR11 where reconstruction does not improve the uncertainty. The constraints obtained using the pre- and post-reconstruction wedges show a similar behaviour.

Table 5. Measurements of $\alpha_{||}$ and $\alpha_{\perp}$ and their 1σ errors for CMASS mock galaxy catalogues when we use different anisotropic clustering estimates (multipoles and wedges). We choose to show median values which are less affected by the range of parameters over which we integrate to determine best-fitting values and their associated errors. The columns are the median values of α, ϵ, $\alpha_{||,\perp}$ ($\widetilde{\alpha}$, $\widetilde{\epsilon}$, $\widetilde{\alpha_{||,\perp}}$), and the standard deviations of α, ϵ, $\alpha_{||,\perp}$ ($S_{\alpha,\epsilon,\alpha_{||,\perp}}$). Further details can be found in Vargas-Magana et al. (2013). The 'consensus' results combine the likelihoods determined from multipoles and wedges, as described in the text.

Method	$\widetilde{\alpha}$	S_{α}	$\widetilde{\epsilon}$	S_{ϵ}	$\widetilde{\alpha_{\parallel}}$	$S_{\alpha_{\parallel}}$	$\widetilde{\sigma_{\alpha_{\parallel}}}$	$S_{\sigma_{\alpha_{\parallel}}}$	$\widetilde{\alpha_{\perp}}$	$S_{\alpha_{\perp}}$	$\widetilde{\sigma_{\alpha_{\perp}}}$	$S_{\sigma_{\alpha_{\perp}}}$
Post-recon DR11												
Consensus	–	–	–	–	1.0009	0.0252	0.0270	0.0045	0.9984	0.0143	0.0149	0.0018
Multipoles	1.0002	0.0092	0.0011	0.0122	1.0032	0.0266	0.0248	0.0072	0.9999	0.0149	0.0137	0.0018
Wedges	1.0003	0.0090	0.0005	0.0124	1.0006	0.0264	0.0296	0.0052	0.9993	0.0153	0.0161	0.0026
Pre-recon DR11												
Multipoles	0.9995	0.0155	0.0022	0.0189	1.0058	0.0443	0.0384	0.0150	0.9965	0.0210	0.0205	0.0033
Wedges	0.9991	0.0152	−0.0011	0.0207	0.9965	0.0475	0.0466	0.0137	1.0007	0.0222	0.0230	0.0086

Table 6. Variations in measured parameters and errors from the DR11 CMASS mock galaxy catalogues post-reconstruction for different changes to the fiducial fitting methodology. The variation is defined as $\Delta v = v^{i} - v^{\rm fid}$, where v is the parameter or error of interest. These results confirm the robustness of the fitting methodology. The largest variation observed on the fitted parameters is in epsilon $\Delta\epsilon = 0.003$ while the largest variation in α is only $\Delta\alpha = 0.001$. Median variations Δv, and percentiles are multiplied by 100.

Model	$100\widetilde{\Delta\alpha}$	$100\widetilde{\Delta\sigma_{\alpha}}$	$100\widetilde{\Delta\epsilon}$	$100\widetilde{\Delta\sigma_{\epsilon}}$	$100\widetilde{\Delta\alpha_{\parallel}}$	$100\widetilde{\Delta\sigma_{\alpha_{\parallel}}}$	$100\widetilde{\Delta\alpha_{\perp}}$	$100\widetilde{\Delta\sigma_{\alpha_{\perp}}}$
$30 < r < 200$	$0.05^{+0.13}_{-0.12}$	$-0.03^{+0.02}_{-0.03}$	$0.10^{+0.15}_{-0.11}$	$-0.01^{+0.03}_{-0.03}$	$0.25^{+0.41}_{-0.31}$	$-0.01^{+0.10}_{-0.12}$	$-0.06^{+0.09}_{-0.09}$	$-0.04^{+0.03}_{-0.03}$
Two-term $A_l(r)$	$0.03^{+0.07}_{-0.06}$	$0.02^{+0.02}_{-0.02}$	$0.27^{+0.15}_{-0.12}$	$-0.02^{+0.03}_{-0.04}$	$0.58^{+0.32}_{-0.25}$	$0.02^{+0.07}_{-0.07}$	$-0.24^{+0.13}_{-0.18}$	$-0.04^{+0.02}_{-0.03}$
Four-term $A_l(r)$	$-0.05^{+0.06}_{-0.08}$	$-0.01^{+0.02}_{-0.02}$	$-0.15^{+0.11}_{-0.12}$	$0.00^{+0.03}_{-0.03}$	$-0.35^{+0.27}_{-0.31}$	$-0.01^{+0.07}_{-0.07}$	$0.09^{+0.08}_{-0.07}$	$0.01^{+0.01}_{-0.01}$
Fixed $\beta = 0.0$	$-0.00^{+0.01}_{-0.03}$	$-0.00^{+0.00}_{-0.01}$	$0.02^{+0.10}_{-0.10}$	$-0.01^{+0.02}_{-0.03}$	$0.03^{+0.17}_{-0.21}$	$-0.02^{+0.09}_{-0.12}$	$-0.02^{+0.11}_{-0.12}$	$-0.02^{+0.03}_{-0.03}$
No priors (RL)	$0.00^{+0.04}_{-0.02}$	$0.02^{+0.06}_{-0.01}$	$-0.03^{+0.12}_{-0.12}$	$0.05^{+0.12}_{-0.03}$	$-0.05^{+0.24}_{-0.21}$	$0.08^{+0.36}_{-0.10}$	$0.02^{+0.15}_{-0.11}$	$0.05^{+0.08}_{-0.03}$
Only B_0 prior (RL)	$0.00^{+0.04}_{-0.01}$	$0.02^{+0.04}_{-0.01}$	$-0.02^{+0.11}_{-0.11}$	$0.04^{+0.08}_{-0.02}$	$-0.04^{+0.22}_{-0.20}$	$0.06^{+0.28}_{-0.09}$	$0.02^{+0.14}_{-0.11}$	$0.04^{+0.06}_{-0.03}$
Only β prior (RL)	$-0.00^{+0.01}_{-0.01}$	$0.00^{+0.01}_{-0.00}$	$-0.00^{+0.01}_{-0.02}$	$0.01^{+0.02}_{-0.01}$	$-0.00^{+0.03}_{-0.05}$	$0.02^{+0.04}_{-0.02}$	$0.00^{+0.01}_{-0.01}$	$0.01^{+0.01}_{-0.00}$

Downloaded from http://mnras.oxfordjournals.org/ at University of California, Irvine on March 16, 2016

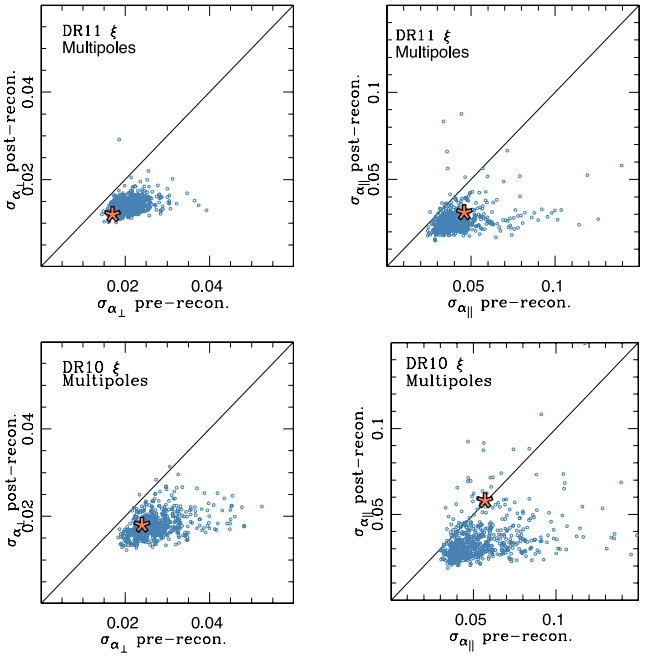

Figure 7. These are scatter plots of σ_α post-reconstruction: mocks (circles) + data (star) for $\sigma_{\alpha_\perp}$ and $\sigma_{\alpha_{||}}$ for CMASS DR10 and DR11. The reconstruction significantly improves the precision in nearly all of the 600 mock galaxy samples for both DR10 and DR11. Note that we converted to one parametrization ($\alpha_\parallel$, $\alpha_\perp$) for ease of comparison between multipoles and wedges.

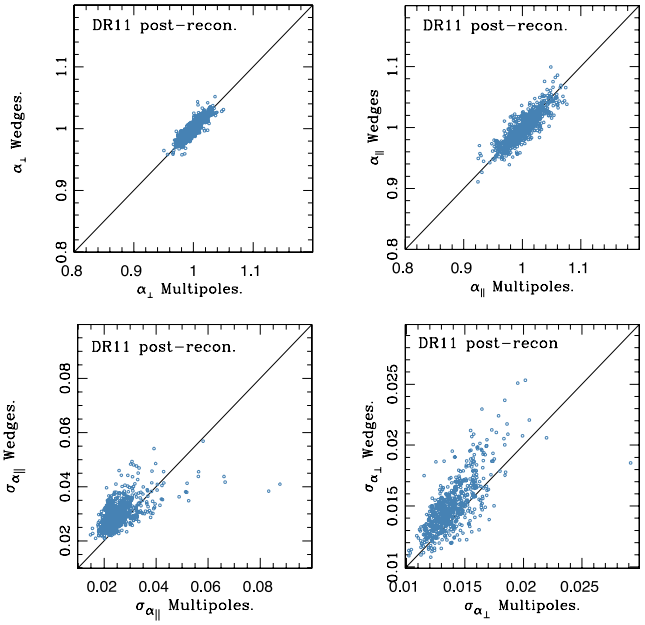

Figure 8. Top panels compare the $\alpha_\parallel$ and $\alpha_\perp$ recovered with the multipoles methodology with the values recovered from wedges for the DR11 CMASS mock galaxy samples. Bottom panel compares the $\sigma_{\alpha_{||}}$ and $\sigma_{\alpha_\perp}$ recovered with the multipoles with the values recovered from wedges using the same mock galaxy samples as in the top panel.

5.3 Comparing and combining methodologies

Table 5 compares the fitting results of our DR11 mock galaxy catalogues using the multipoles and clustering wedges. There are slight differences in both the median and dispersion between methods in pre-reconstruction, but both are unbiased and give similar errors in both $\alpha_\parallel$ and $\alpha_\perp$. For instance, the median and the 68 per cent confidence level of the variation between the two methods, $\Delta\alpha_{||} = \alpha_{||,\,\mathrm{multipoles}} - \alpha_{||,\,\mathrm{wedges}}$, is $\widetilde{\Delta\alpha_{||}} = +0.005^{+0.025}_{-0.028}$ while that for $\alpha_\perp$ is $\widetilde{\Delta\alpha_\perp} = -0.004^{+0.014}_{-0.011}$. These are small differences, especially when compared to the standard deviations ($S_{\alpha_\parallel}$ and $S_{\alpha_\perp}$) within the mocks, which are of the order of $\sim$0.046 and $\sim$0.021, respectively.

As we can see from Table 5, the fitting results of post-reconstructed mock catalogues from both methods are extremely similar. After reconstruction, the median BAO measurements become even more similar between the two methods and the scatter, relative to the standard deviation, decreases slightly: we find $\widetilde{\Delta\alpha_{||}} = +0.001^{+0.016}_{-0.016}$ and $\widetilde{\Delta\alpha_\perp} = -0.001^{+0.008}_{-0.007}$. The top panels of Fig. 8 show scatter plots between the BAO measurements for multipoles and those of wedges, post-reconstruction, determined from the 600 mock samples. The two measurements are clearly correlated.

We find that the multipole results are slightly more precise, on average. We obtain tight constraints on both $\alpha_{||}$ and $\alpha_\perp$. In particular, $\widetilde{\Delta\sigma_{\alpha_{||}}} = -0.008^{-0.008}_{+0.007}$ and $\widetilde{\Delta\sigma_{\alpha_\perp}} = -0.003^{+0.003}_{-0.003}$ pre-reconstruction and post reconstruction, while the median difference in best-fitting values are $\widetilde{\Delta\alpha_{||}} = -0.005^{+0.005}_{-0.004}$ and $\widetilde{\Delta\alpha_\perp} = -0.002^{+0.001}_{-0.002}$. As measurements from the two fitting methodologies are clearly correlated, it is not surprising that the obtained precisions on the α are similar.

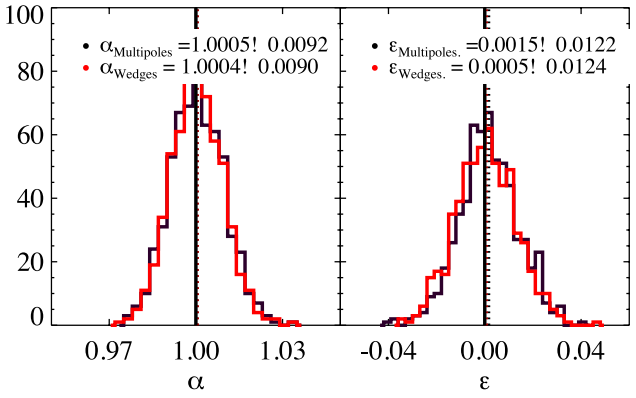

Figure 9. The distributions of α (left) and ϵ (right) recovered with multipoles methodology compared to the values recovered from wedges for DR11 mock galaxy samples. The legend indicates the mean and rms of the distribution.

For reasons that will become apparent later in Section 7, we also look at the differences in fitting results between wedges and multipoles when we measure α and ϵ, in addition to $\alpha_\perp$ and $\alpha_\parallel$. In Fig. 9, we show the histogram of the fitted α and ϵ from the two different methodologies used in anisotropic clustering. The median values of α are almost identical in the two methodologies with close to zero median shift. The ϵ distributions show small median shift of 0.2 and -0.1 per cent which point in different directions for multipoles and wedges approaches, respectively. The standard deviations in both α and ϵ from both methods are also comparable.

In general, the statistics indicate good agreement between the distributions of the fitted parameters and errors obtained from multipoles and wedges. We do not find any indication that favours one technique over the other. Pre-reconstruction, we find differences

Downloaded from http://mnras.oxfordjournals.org/ at University of California, Irvine on March 16, 2016

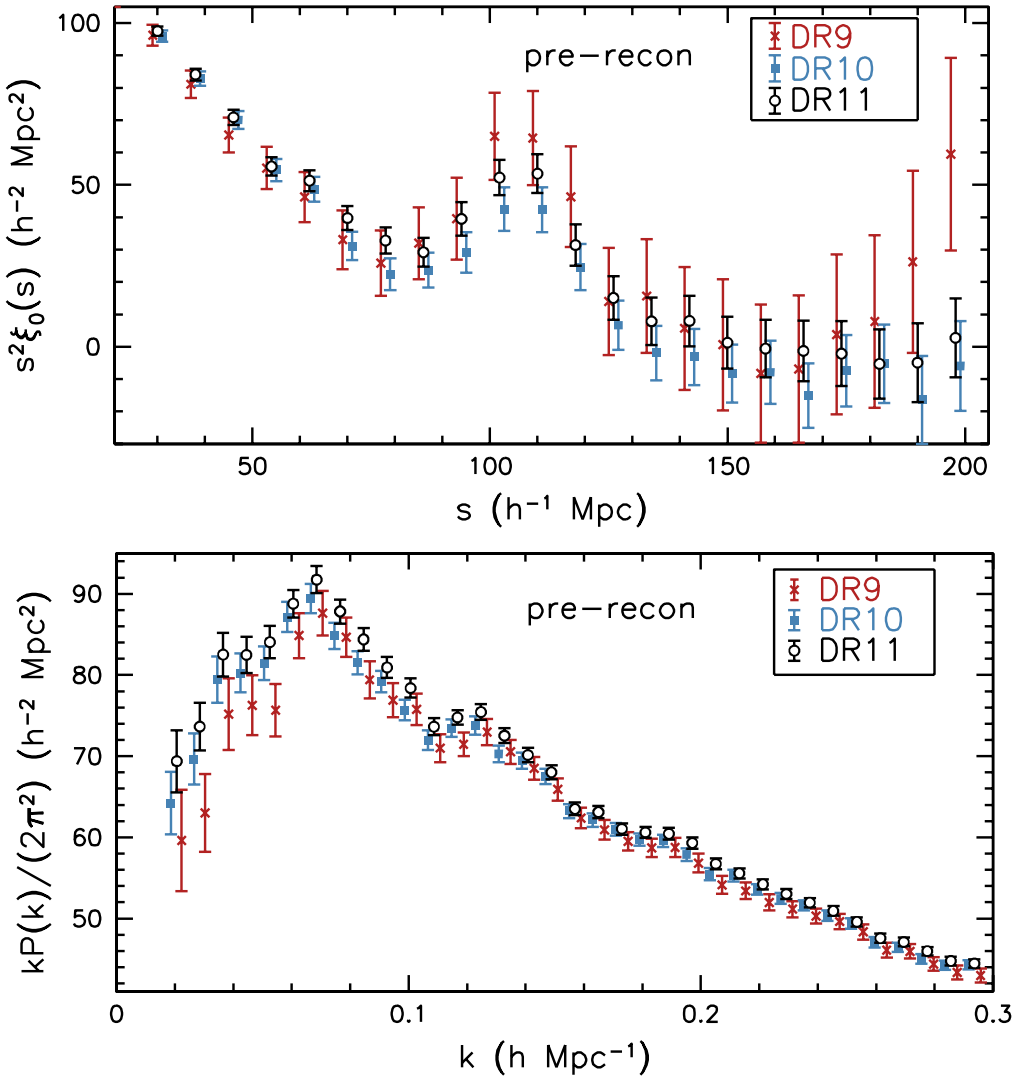

Figure 10. Top panel: the measured monopole of the CMASS galaxy correlation function, multiplied by the square of the scale, s, for each of the BOSS data releases. These figures are shown pre-reconstruction. For clarity, the DR10 data have been shifted horizontally by $+1\,h^{-1}$ Mpc and the DR9 data by $-1\,h^{-1}$ Mpc. Bottom panel: the measured spherically averaged CMASS galaxy power spectrum, multiplied by the frequency scale, k, for each of the BOSS data releases. For clarity, the DR9 data have been shifted by $+0.002\,h$ Mpc^{-1} and the DR10 data by $-0.002\,h$ Mpc^{-1}. All of the error bars shown in both panels represent the diagonal elements of the covariance matrix determined from the mocks. One can observe broadly consistent clustering, especially in the overall shape of each curve.

of 0.2σ in the median values of $\alpha_{||}$ and $\alpha_{\perp}$ recovered by the two methods, but post-reconstruction these differences become negligibly small, less than 0.08σ. We therefore believe that the two methods are equally unbiased. The scatter in the results recovered by the Multipoles and Wedges methods in individual realizations come from shot-noise and differences in methodology, as explored further in Vargas-Magana et al. (2013).

Given that the multipoles and wedges results are both unbiased but are not perfectly correlated, our results are improved by combining the two results. We do this following the procedure adopted in Anderson et al. (2014). Briefly, we take the mean of the log-likelihood surfaces obtained using each method and use this averaged likelihood surface to obtain consensus results. We have applied this procedure to the results from each mock realization and the statistics are listed as the 'consensus' values in Table 5. The standard deviation in both the BAO measurements and their uncertainties have decreased, showing that a small improvement is afforded by combining the two measurements.

6 BAO MEASUREMENTS FROM ISOTROPIC CLUSTERING ESTIMATES

6.1 Clustering estimates

In the previous sections, we detailed our analysis techniques and demonstrated they recover unbiased estimates of the BAO scale. We now apply our results to the BOSS data. We present our isotropic measurements in this section and our anisotropic results in the following section.

The configuration space and Fourier space clustering measurements made from the DR10 and DR11 CMASS samples are presented in Fig. 10 for $\xi(s)$ and $P(k)$, using our fiducial binning choice. These points are compared against the DR9 clustering results[2] presented in Anderson et al. (2012). For both $P(k)$ and $\xi(s)$, there are

[2] We recalculate the DR9 $P(k)$ using the new method presented in Section 4.1 for consistency.

Downloaded from http://mnras.oxfordjournals.org/ at University of California, Irvine on March 16, 2016

variations in the power observed in the different data sets, but the shapes of each are clearly consistent, suggesting that we should expect to recover consistent results for the BAO scale. Measurements of the clustering in the LOWZ sample are presented in Tojeiro et al. (2014).

The power is observed to increase with each data release, and similar behaviour is observed in the correlation function for $s < 70\,h^{-1}$ Mpc. The difference in clustering amplitude can be explained by the tiling of the survey. In order to obtain the most complete sample, dense regions are observed using overlapping plates. Thus, as the survey progresses, a larger percentage of observations using overlapping plates are completed and the mean density of the survey increases. This increase in density occurs almost exclusively by adding overdense regions and thus increases the clustering amplitude. The measured increase in clustering amplitude is roughly the square of increase in density (4 per cent between DR9 and DR11, and 2 per cent between DR10 and DR11). As the survey nears completion, the issue naturally becomes less important. For DR11, it represents, at worst, a 1 per cent underestimate of the bias of the CMASS galaxies. Consistent trends are found in the LOWZ sample (Tojeiro et al. 2014).

Fig. 11 displays the best-fitting BAO model (solid curves) compared to the data for $\xi(s)$ (left-hand panels) and $P(k)$ (right-hand panels) for DR11 only. The pre-reconstruction measurements are displayed in the top panels, and the post-reconstruction ones in the bottom panels. The measurements are presented for our fiducial binning width and centring, and show a clear BAO feature in both $P(k)$ and $\xi(s)$, with the best-fitting models providing a good fit. The effect of reconstruction is clear for both the correlation function and power spectrum, with the BAO signature becoming more pronounced relative to the smooth shape of the measurements. Indeed, all of the BAO measurements, listed in Table 7, have improved post-reconstruction, in contrast to our DR9 results (Anderson et al. 2012). This behaviour is expected given the results of Section 4.2, which showed that, given the precision afforded by the DR11 volume coverage, reconstruction improved the results from all of our mock catalogues. Reconstruction is particularly striking in the power spectrum plot, showing a clear third peak in the post-reconstruction $P(k)$.

6.2 DR11 acoustic-scale measurements

Our BAO measurements are listed in Table 7. The mocks for DR10 and DR11 show significant improvement with reconstruction in most realizations, and we therefore adopt the reconstruction results as our default measurements. Our consensus value for the CMASS BAO measurement, $\alpha = 1.0144 \pm 0.0089$, is determined from a combination of $P(k)$ and $\xi(s)$ measurements, and in what follows, we describe the process of obtaining this value, and tests that validate it.

Post-reconstruction, the significance of the BAO detection in both the correlation function and the power spectrum are greater than 7σ for the reconstructed DR11 CMASS BAO measurements. The significance of detection is shown in Fig. 12, where we also

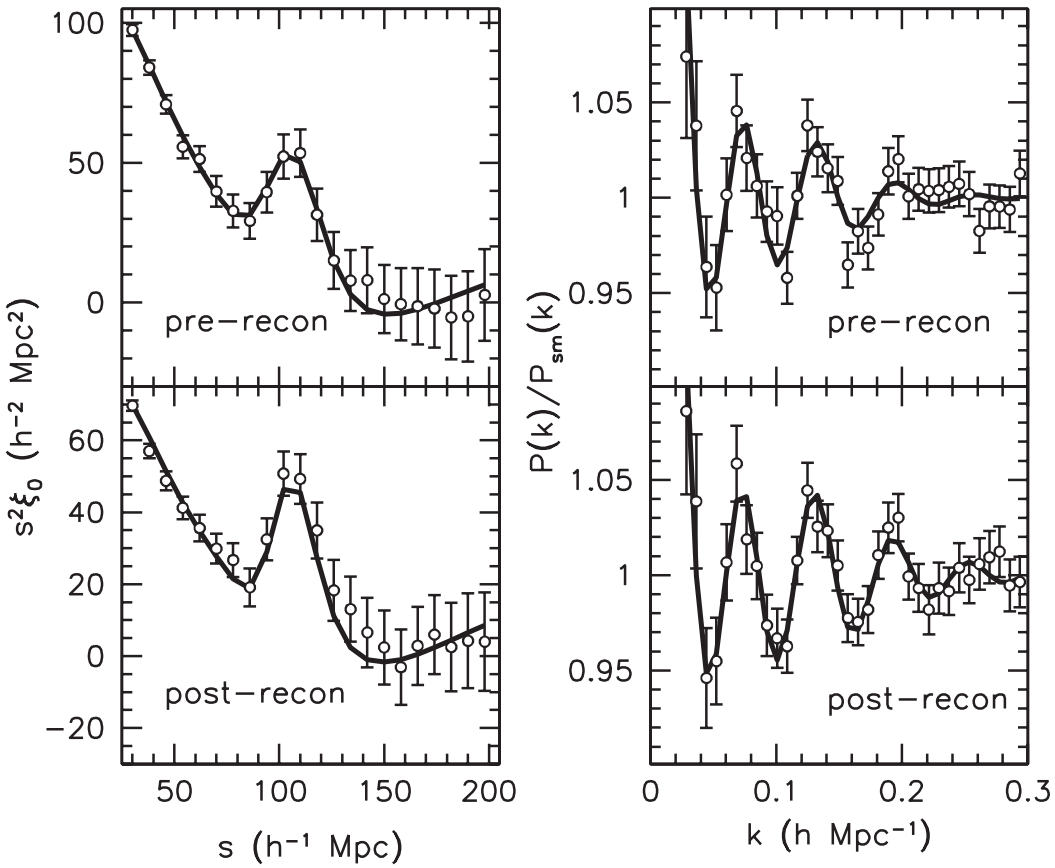

Figure 11. DR11 CMASS clustering measurements (black circles) with $\xi(s)$ shown in the left-hand panels and $P(k)$ in the right-hand panels. The top panels show the measurements prior to reconstruction and the bottom panels show the measurements after reconstruction. The solid lines show the best-fitting BAO model in each case. One can see that reconstruction has sharpened the acoustic feature considerably for both $\xi(s)$ and $P(k)$.

Downloaded from http://mnras.oxfordjournals.org/ at University of California, Irvine on March 16, 2016

Table 7. Isotropic BAO-scale measurements recovered from BOSS data. The 'combined' results are the optimally combined post-reconstruction α measurements across multiple bin centre choices, based on the correlation matrix obtained from the mock samples. The $P(k)$+$\xi(s)$ measurements are the mean of these combined results, with an uncertainty calculated as described in the text. The quoted errors are statistical only, except for the 'Consensus' measurements, where a systematic uncertainty has been included. This estimated systematic error is discussed in Section 8.1.

Estimator	α	χ^2/dof
DR11 CMASS		
Consensus $z = 0.57$	**1.0144 ± 0.0098 (stat+sys)**	
$P(k)$+$\xi(s)$	1.0144 ± 0.0089 (stat)	
Combined $P(k)$	1.0110 ± 0.0093	
Combined $\xi(s)$	1.0178 ± 0.0089	
Post-recon $P(k)$	1.0114 ± 0.0093	18/27
Post-recon $\xi_0(s)$	1.0209 ± 0.0091	16/17
Pre-recon $P(k)$	1.025 ± 0.015	33/27
Pre-recon $\xi_0(s)$	1.031 ± 0.013	14/17
DR10 CMASS		
Consensus	1.014 ± 0.014 (stat+sys)	
Post-recon $P(k)$	1.007 ± 0.013	23/28
Post-recon $\xi_0(s)$	1.022 ± 0.013	14/17
Pre-recon $P(k)$	1.023 ± 0.019	35/28
Pre-recon $\xi_0(s)$	1.022 ± 0.017	16/17
DR9 CMASS		
Consensus	1.033 ± 0.017	
DR11 LOWZ		
Consensus $z = 0.32$	**1.018 ± 0.021 (stat+sys)**	
$P(k)$+$\xi(s)$	1.018 ± 0.020 (stat)	
DR10 LOWZ		
Consensus	1.027 ± 0.029 (stat+sys)	

see a difference in the detection significance between results from $\xi(s)$ and $P(k)$. This variation is caused by the differential ability of the models for the broad-band component to match the offset between the data and the no-baryon model. The broad-band model for the power spectrum has more free parameters than that for the correlation function, so it is perhaps not surprising that the no-baryon model is a slightly better fit.

Table 7 also lists χ^2/dof for the best-fitting models, showing that they are close to unity for DR10 and DR11 fits using both the correlation function and power spectrum. The most unusual is the χ^2/dof $=18/27$ for the post-reconstruction DR11 $P(k)$ measurement. Such a low χ^2 is expected in 10 per cent of cases, thus we conclude that our best-fitting models provide adequate descriptions of the data.

The precision of the BAO measurements are typical of those achieved in the mock samples. This consistency in shown in the top panels of Fig. 4, where the orange stars show the uncertainty in the data post-reconstruction versus the uncertainty pre-reconstruction. All of the CMASS data points lie within well the distribution of the mock points. The most discrepant result is for the DR10 $P(k)$ measurement post-reconstruction; it has an uncertainty of 0.014, while the mean uncertainty from the mock realizations is 0.011, but one can see that many mock realizations recover an uncertainty larger than 0.014.

We combine the DR11 CMASS $\xi(s)$ BAO measurements using 8 bin centres and the $P(k)$ results using 10 bin centres in the same manner as applied to the mocks, as described in Section 4.3. The individual fits determined for different bin centres are shown in Table 8. For $\xi(s)$, our fiducial choice recovered the largest α of any of the bin centres. Thus, when combining the results across all of the bin centre choices, α decreases to 1.0178 ± 0.0089. The uncertainty has decreased by only 2 per cent (compared to the mean of 7 per cent found for the mocks) in part because the estimated uncertainty of the fiducial bin choice (0.0091) is less than the weighted mean uncertainty across all of the bin choices (0.0092). For $P(k)$, the result changes little when we combine across the results of the 10 bin centre choices; it changes from 1.0114 ± 0.0093 to 1.0110 ± 0.0093.

We obtain a BAO measurement with an expected error measured from the likelihood surface that is less than 1 per cent for both the reconstructed $\xi(s)$ and $P(k)$. The difference between the two values of α is 0.0068. While small in magnitude, this difference is unexpectedly large in the context of the mock results, for which we found a correlation factor of 0.95 between the $P(k)$ and $\xi(s)$ results combined

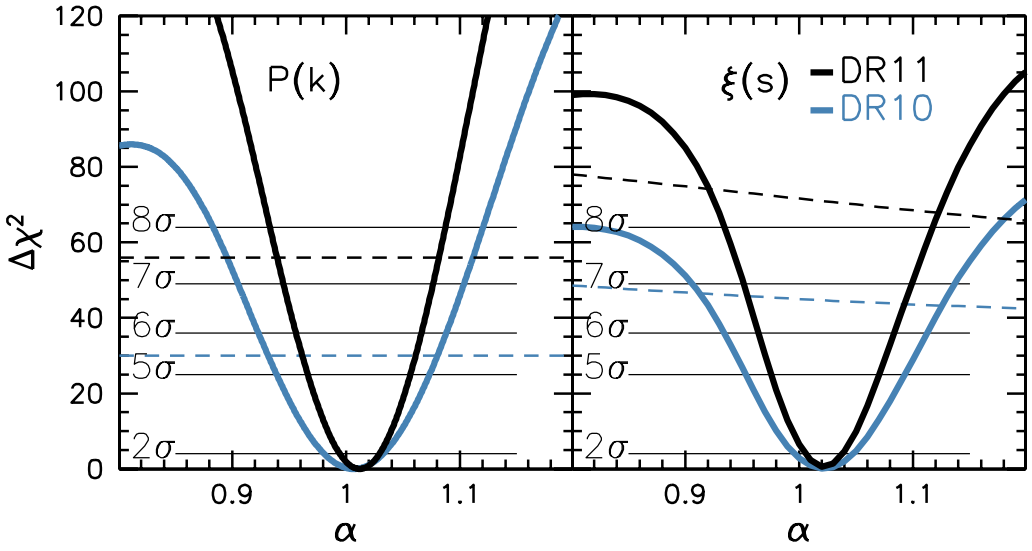

Figure 12. Plot of χ^2 versus α, for reconstructed data from DR10 (blue), and DR11 (black) data, for $P(k)$ (left) and $\xi(s)$ (right). The dashed lines display the χ^2 for a model without BAO, which we compute by setting $\Sigma_{\rm nl} \to \infty$ in equations (23) and (26). In the $\xi(s)$ case, this limiting template still depends on α, so the $\chi^2(\alpha)$ is not constant. Our $P(k)$ model has no dependence on α in this limit. The DR11 detection significance is greater than 7σ for $P(k)$ and 8σ for $\xi(s)$.

Downloaded from http://mnras.oxfordjournals.org/ at University of California, Irvine on March 16, 2016

Table 8. BAO-scale measurements for DR11 reconstructed data using different bin centres. These results are combined using their correlation matrix to obtain optimized BAO measurements.

Shift	α	χ^2/dof
$P(k)$		
$\Delta k_i = 0$	1.0115 ± 0.0093	18/27
$\Delta k_i = 0.0008\,h\,\mathrm{Mpc}^{-1}$	1.0113 ± 0.0094	19/27
$\Delta k_i = 0.0016\,h\,\mathrm{Mpc}^{-1}$	1.0101 ± 0.0096	21/27
$\Delta k_i = 0.0024\,h\,\mathrm{Mpc}^{-1}$	1.0097 ± 0.0097	21/27
$\Delta k_i = 0.0032\,h\,\mathrm{Mpc}^{-1}$	1.0103 ± 0.0095	20/27
$\Delta k_i = 0.004\,h\,\mathrm{Mpc}^{-1}$	1.0111 ± 0.0094	19/27
$\Delta k_i = 0.0048\,h\,\mathrm{Mpc}^{-1}$	1.0115 ± 0.0094	18/27
$\Delta k_i = 0.0056\,h\,\mathrm{Mpc}^{-1}$	1.0119 ± 0.0093	16/27
$\Delta k_i = 0.0064\,h\,\mathrm{Mpc}^{-1}$	1.0125 ± 0.0092	16/27
$\Delta k_i = 0.0072\,h\,\mathrm{Mpc}^{-1}$	1.0122 ± 0.0092	17/27
$\xi(s)$		
$\Delta s_i = -2\,h^{-1}\,\mathrm{Mpc}$	1.0188 ± 0.0104	12/17
$\Delta s_i = -1\,h^{-1}\,\mathrm{Mpc}$	1.0154 ± 0.0094	8/17
$\Delta s_i = 0$	1.0209 ± 0.0091	16/17
$\Delta s_i = +1\,h^{-1}\,\mathrm{Mpc}$	1.0186 ± 0.0086	14/17
$\Delta s_i = +2\,h^{-1}\,\mathrm{Mpc}$	1.0201 ± 0.0087	16/17
$\Delta s_i = +3\,h^{-1}\,\mathrm{Mpc}$	1.0164 ± 0.0087	19/17
$\Delta s_i = +4\,h^{-1}\,\mathrm{Mpc}$	1.0153 ± 0.0092	17/17
$\Delta s_i = +5\,h^{-1}\,\mathrm{Mpc}$	1.0191 ± 0.0100	13/17

across all of the bin choices. Accounting for this correlation factor, the expected 1σ dispersion in the $P(k)$ and $\xi(s)$ measurements is $(\sigma^2_{\alpha,P} + \sigma^2_{\alpha,\xi} - 2C_{P,\xi}\sigma_{\alpha,P}\sigma_{\alpha,\xi})^{1/2} = 0.0028$. The discrepancy in the data is thus 2.4σ. Comparing $|\alpha_P - \alpha_\xi|/(\sigma^2_{\alpha,P} + \sigma^2_{\alpha,\xi})^{1/2}$ to the results from the mocks, we find seven (1.2 per cent) that have a larger deviation, consistent with our estimation of a 2.4σ discrepancy. Both estimates of α are stable to a variety of robustness tests, as we will show in Section 6.4, and our tests on mock samples demonstrate that each estimator is unbiased. We therefore conclude that, despite being unusual, the difference between the two measurements is not indicative of an existence of a bias in either measurement.

Our tests on mocks suggest no systematic effects for either the $P(k)$ or $\xi(s)$ results when they are obtained by combining results across bin centres. Our methodology applied to mock samples recovers unbiased estimates of the BAO position for both $\xi(s)$ and $P(k)$ with nearly identical uncertainty. We therefore obtain the consensus BAO-scale measurement by assuming the mean uncertainty of the $\xi(s)$ and $P(k)$ measurements for each and using the 0.95 correlation factor. The correct treatment of the data, assuming Gaussian statistics and no systematic uncertainty is to take the mean of $P(k)$ and $\xi(s)$ measurements, reducing the uncertainty based on their correlation factor. Thus, our consensus value for the CMASS BAO measurement is $\alpha = 1.0144 \pm 0.0089$, where this uncertainty is purely statistical. Our systematic error budget is discussed in Section 8.1.

We obtain our consensus DR11 LOWZ isotropic BAO measurement, at an effective redshift $z = 0.32$ by applying the same process as applied to CMASS. The details can be found in Tojeiro et al. (2014). The difference in the recovered BAO scale from LOWZ $P(k)$ and $\xi(s)$ is within 1σ of the expected difference and is opposite in sign to the difference we find for CMASS. The consensus DR11 LOWZ measurement is $\alpha = 1.018 \pm 0.020$, considering only the statistical uncertainty.

6.3 DR10 BAO measurements

For completeness, we also include DR10 BAO measurements in Table 7. Post-reconstruction, these data produce a 1.4 per cent BAO-scale measurement that is consistent with the DR11 measurements discussed in the previous section. For pre-reconstruction measurements, the error on DR11 the result is 30 per cent lower than for DR10. For the post-reconstruction results, the improvement increases to 40 per cent. The reconstruction is more efficient for DR11, which almost certainly results from the more contiguous nature of the DR11 survey mask.

As shown in Fig. 12, the detections for DR10 are both greater than 5σ, with the significance for the $\xi(s)$ measurement being higher than that of the $P(k)$ measurement. As discussed in Section 6.2, the improved detection observed in $\xi(s)$ is because the $P(k)$ broad-band model is better able to model the full $P(k)$ when no BAO are included, compared with the broad-band $\xi(s)$ model.

The most obvious issue for the DR10 results in Table 7 is that, for the DR10 $P(k)$, the measurement of α shifts by -0.020 post-reconstruction, compared to a mean shift of -0.004 ± 0.015 observed in the mocks (here the uncertainty is the standard deviation of the mock values). The size of this shift is thus only just greater than 1σ and is consequently not a significant concern.

6.4 DR11 robustness checks

In order to ensure that our measurements on the CMASS data are robust to our methodological and binning choices, we re-measure the BAO scale using the reconstructed DR11 power spectrum and correlation function, changing the fitting methods, binning and fitting to the NGC and SGC separately. Table 9 lists the results of these tests.

The absolute difference in the α values recovered from the NGC and SGC regions has decreased considerably from Anderson et al. (2012). For the correlations function fits, the decrease if from 0.055 to 0.031. Given the decrease in the uncertainty thanks to the larger area coverage in both regions, the significance of the discrepancy is similar to that found for DR9, 1.4σ. We find that 79 out of the 600 mock samples (13 per cent) have a larger discrepancy, consistent with the estimation of a 1.4σ discrepancy. We find a similar picture when we fit to the $P(k)$ measurements from NGC and SGC although, in this case, the discrepancy is slightly larger, at 1.8σ. Less significant differences, with opposite sign, are found in the DR11 LOWZ sample (Tojeiro et al. 2014).

Table 9 also presents results fitting to the power spectrum for different ranges in k, removing the largest and smallest scale data in turn. The recovered errors on α do not change significantly if we remove data at $k < 0.05\,h\,\mathrm{Mpc}^{-1}$ or at $k > 0.25\,h\,\mathrm{Mpc}^{-1}$. This is not surprising, given there is little BAO signal on these scales. Only fitting to $0.02 < k < 0.25\,h\,\mathrm{Mpc}^{-1}$ reduces the best-fitting value of α by 0.0039, but cutting further in k to $0.02 < k < 0.2\,h\,\mathrm{Mpc}^{-1}$ returns the best fit back to the fiducial value, suggesting that there is no wavelength-dependent systematic trend present. Fixing the BAO damping at the best-fitting value from the mocks $\Sigma_{\rm nl} = 4.6\,h^{-1}\,\mathrm{Mpc}$ does not alter the best-fitting value of α, but does decrease the size of the error, but we consider this action to be too aggressive given that the true value of the damping is unknown. Changing $\Sigma_{\rm nl}$ by $\pm 1\,h^{-1}\,\mathrm{Mpc}$ does not have a large effect, although overdamping the BAO in the model does increase the error on α, as it removes the signal we wish to match to the data.

Results from applying two alternatives to the model for the broad-band power spectrum shape are also shown: cutting the polynomial

Downloaded from http://mnras.oxfordjournals.org/ at University of California, Irvine on March 16, 2016

Table 9. Robustness checks on isotropic BAO-scale measurements recovered from DR11 reconstructed data.

Estimator	Change	α	χ^2/dof
$P(k)$	Fiducial	1.0114 ± 0.0093	18/27
	NGC only	1.0007 ± 0.0113	16/27
	SGC only	1.0367 ± 0.0167	15/27
	$0.02 < k < 0.25\,h\,\mathrm{Mpc}^{-1}$	1.0082 ± 0.0094	14/21
	$0.02 < k < 0.2\,h\,\mathrm{Mpc}^{-1}$	1.0121 ± 0.0113	11/15
	$0.05 < k < 0.3\,h\,\mathrm{Mpc}^{-1}$	1.0120 ± 0.0091	15/23
	$\Sigma_{\rm nl} = 3.6 \pm 0.0\,h^{-1}$ Mpc	1.0111 ± 0.0085	19/28
	$\Sigma_{\rm nl} = 4.6 \pm 0.0\,h^{-1}$ Mpc	1.0119 ± 0.0089	19/28
	$\Sigma_{\rm nl} = 5.6 \pm 0.0\,h^{-1}$ Mpc	1.0116 ± 0.0097	18/28
	$A_1, A_2 = 0$	1.0136 ± 0.0095	40/29
	Spline fit	1.0109 ± 0.0094	17/24
	$\Delta k = 0.0032\,h\,\mathrm{Mpc}^{-1}$	1.0122 ± 0.0097	71/79
	$\Delta k = 0.004\,h\,\mathrm{Mpc}^{-1}$	1.0082 ± 0.0094	55/62
	$\Delta k = 0.006\,h\,\mathrm{Mpc}^{-1}$	1.0091 ± 0.0096	33/39
	$\Delta k = 0.01\,h\,\mathrm{Mpc}^{-1}$	1.0120 ± 0.0097	16/20
	$\Delta k = 0.012\,h\,\mathrm{Mpc}^{-1}$	1.0133 ± 0.0091	9/15
	$\Delta k = 0.016\,h\,\mathrm{Mpc}^{-1}$	1.0100 ± 0.0099	5/9
	$\Delta k = 0.02\,h\,\mathrm{Mpc}^{-1}$	1.0186 ± 0.0105	5/6
$\xi(s)$	Fiducial	1.0209 ± 0.0091	16/17
	NGC only	1.0132 ± 0.0105	12/17
	SGC only	1.0441 ± 0.0190	15/17
	$50 < s < 150\,h^{-1}$ Mpc	1.0208 ± 0.0094	6/7
	$a_1, a_2, a_3 = 0$	1.0210 ± 0.0097	24/20
	$a_1, a_2 = 0$	1.0232 ± 0.0098	19/19
	$a_1 = 0$	1.0231 ± 0.0099	19/18
	$a_2 = 0$	1.0218 ± 0.0097	18/18
	B_ξ free	1.0209 ± 0.0091	15/17
	$\Sigma_{\rm nl} = 3.6\,h^{-1}$ Mpc	1.0212 ± 0.0089	15/17
	$\Sigma_{\rm nl} = 5.6\,h^{-1}$ Mpc	1.0206 ± 0.0095	17/17
	Recon $\beta = 0.318$	1.0195 ± 0.0090	11/17
	Recon $\beta = 0.478$	1.0206 ± 0.0094	18/17
	Recon $b = 1.50$	1.0224 ± 0.0100	23/17
	Recon $b = 2.24$	1.0183 ± 0.0086	14/17
	$\Delta s = 4\,h^{-1}$ Mpc	1.0197 ± 0.0090	42/38
	$\Delta s = 5\,h^{-1}$ Mpc	1.0156 ± 0.0093	31/29
	$\Delta s = 6\,h^{-1}$ Mpc	1.0189 ± 0.0093	19/23
	$\Delta s = 7\,h^{-1}$ Mpc	1.0165 ± 0.0088	20/19
	$\Delta s = 9\,h^{-1}$ Mpc	1.0188 ± 0.0089	10/14
	$\Delta s = 10\,h^{-1}$ Mpc	1.0175 ± 0.0099	9/12

model back to a four-parameter model by setting $A_1 = 0$ and $A_2 = 0$ in equation (24) only slightly affects α and the recovered error, but does significantly increase the best-fitting value of χ^2, showing that this model inadequately describes the shape of the power. Changing to the bicubic spline broad-band model used previously (Anderson et al. 2012) does not significantly affect either the best-fitting value of α or the recovered error.

Table 9 also presents results reducing the range of scales fitted in the correlations function from $28 < s < 200\,h^{-1}$ Mpc to $50 < s < 150\,h^{-1}$ Mpc: we find a negligible change in the best-fitting value of α, and a revised error that only increases by a small amount, demonstrating that this reduced range of scales contains all of the BAO signal as expected. We also present results from possible changes to the model used to fit the broad-band correlation function, where we remove various polynomial terms, or remove the prior on B_ξ (equation 27). The greatest change is an increase in the recovered α value of 0.0023 when only the constant a_3 term is used to fit $\xi(s)$ (equation 28). Indeed, for $\xi(s)$, the preference for the inclusion of a polynomial is not strong; $\Delta\chi^2 = 8$ for three additional parameters. While the correlation function adds terms to a full linear model (equation 27), the power spectrum only includes the BAO component (equation 23), which is why the polynomial term is less important for $\xi(s)$. As we did for the power spectrum, we vary the non-linear BAO damping, finding consistent results.

The reconstruction algorithm requires an assumed amplitude for the real-space clustering of the galaxy field (b) and its associated velocity field (β). In the fiducial case, we assume $b = 1.87$ and $\beta = 0.398$, which are measured from the mocks. However, our results are not sensitive to these assumptions: if we change each by ± 20 per cent and re-calculate the reconstructed field for the DR11 data and re-determine $\xi(s)$, the resulting measurements of α show negligible change.

For both the power spectrum and correlation function, Table 9 also presents results where we change the bin size, revealing significant scatter. The equivalent comparison for the mock catalogues was presented in Percival et al. (2014). For both $P(k)$ and $\xi(s)$ measured from the data, a dispersion of 0.002 is found in the best-fitting α values. The weighted mean across bin sizes (accounting for the covariance between bins) is 1.0180 ± 0.0089 for $\xi(s)$ and 1.0117 ± 0.0091 for $P(k)$. These measurements are similar to the results obtained when combining across bin centres, suggesting that the combined bin centre results largely capture the same information as changing the bin size. The $\Delta k = 0.02\,h\,\mathrm{Mpc}^{-1}$ bin size recovers $\alpha = 1.0186 \pm 0.0105$. While this value is significantly larger than any of the other bin sizes, this bin size has a relatively small correlation factor, 0.8, with the weighted mean of the other bin sizes. It is thus only 1.2σ from the BAO fit to $P(k)$ averaged into narrower bins.

For all of the tests presented in this section, we find no evidence for changes in the best-fitting value of α that are sufficiently outside of the statistical expectation to indicate the presence of systematic effects. The most significant discrepancy we have observed is the different values of α recovered from $\xi(s)$ and $P(k)$, but the robustness checks presented in this section have not pointed to any origin for this difference, other than simply it being a 2.4σ statistical fluctuation.

6.5 Displaying the BAO feature

Plots of the two-point clustering statistics can be difficult to interpret because of the correlations between the data points. This effect is particularly severe for the correlation function: as the density of the data set increases, different scales become heavily correlated. For example, fluctuations in the amplitude in poorly constrained modes of very low wavenumbers cause the entire correlation function to shift up and down. This means that the diagonal of the covariance matrix is a poor representation of the actual uncertainties. In the case of the acoustic peak, this leads to the data being *more* constraining than it appears! This effect is of no consequence for the formal analysis – one simply uses the covariance matrix when fitting models – but it is a challenge for pedagogy.

The correlations of estimators can be avoided by adopting a new basis, i.e. choosing new estimators that are linear combinations of the original correlation function bins. Such transformations are extensively discussed in Hamilton & Tegmark (2000). There are an infinite number of choices of bases that will produce diagonal covariance matrices. The pedagogical challenge is that the new estimators now represent a mixture of all scales and hence it is not clear how to plot the measurements.

Downloaded from http://mnras.oxfordjournals.org/ at University of California, Irvine on March 16, 2016

Here, we present a hybrid approach in which one adopts a simply defined estimator with compact support as a function of scale, but chooses the estimator so that the covariances are significantly suppressed. In particular, Hamilton & Tegmark (2000) noted that transformations based on the symmetric square root of the Fisher matrix had surprisingly compact support for their power spectrum analysis. When we formed this matrix for the DR11 CMASS correlation function, we found that the first and second off-diagonal terms are nearly constant and that subsequent off-diagonals are small. This suggests that a basis transform of the pentadiagonal form

$$X(s_i) = \frac{x_i - a\,(x_{i-1} + x_{i+1}) - b\,(x_{i-2} + x_{i+2})}{1 - 2a - 2b} \tag{46}$$

will approach a diagonal form. Here, $x_i = s_i^2 \xi_0(s_i)$ and s_i is the bin centre of measurement bin i. We introduce the $1 - 2a - 2b$ factor so as to normalize X such that it returns $X = x$ for constant x. For the first two and last two bins, the terms beyond the end of the range are omitted and the normalization adjusted accordingly.

We find that for DR11 CMASS after reconstruction, values of $a = 0.3$ and $b = 0.1$ sharply reduce the covariances between the bins. The reduced covariance matrices for $\xi(r)$ and $X(r)$ are shown in Fig. 13. The bins near the edge of the range retain some covariances, but the off-diagonal terms of the central 10×10 submatrix of the reduced covariance matrix have a mean and rms of 0.008 ± 0.044, with a worst value of 0.11. For display purposes, this is a good approximation to a diagonal covariance matrix, yet the definition of $X(s)$ is well localized and easy to state. For comparison, the reduced covariance matrix of $s^2\xi_0$ has typical first off-diagonals values of 0.8 and second off-diagonals values of 0.6.

We display this function in Fig. 14. One must also transform the theory to the new estimator: we show the best-fitting BAO models with and without broad-band marginalization, as well as the best-fitting non-BAO model without broad-band marginalization. The presence of the BAO is clear, but now the error bars are representative. For example, the significance of the detection as measured by the $\Delta\chi^2$ of the best-fitting BAO model to the best-fitting non-BAO model is 69.5 using only the diagonal of the covariance matrix of X, as opposed to 74 with the full covariance matrix. We do not use this transformation when fitting models, but we offer it as a pedagogical view.

The same result is shown for DR11 LOWZ post-reconstruction in Fig. 15. Here, we use $a = 0.39$ and $b = 0.04$. The level of the off-diagonal terms is similarly reduced, with an rms of 3.4 per cent and a worst value of 12 per cent.

It is expected that the best values of a and b will depend on the data set, since data with more shot noise will have covariance matrices of the correlation function that are more diagonally dominant. Similarly, the choice of a pentadiagonal form may depend on the binning of the correlation function, as it likely reflects a physical scale of the covariances between bins. However, some of the simplicity likely results from the fact that the covariances between nearby bins are dominated by small-scale correlations in the density field that become independent of separation at large separation. This property gives the matrix a regularity: bins at 90 and 100 Mpc will be correlated to each other similarly to bins at 110 and 120 Mpc.

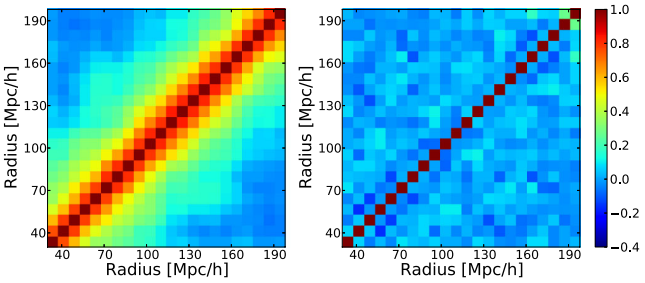

Figure 13. The reduced covariance matrix of $\xi(r)$ (left) and $X(r)$ (right), for the analysis of the DR11 CMASS sample post-reconstruction. One can see that the substantial correlations between separations in $\xi(r)$ have been largely cured in $X(r)$, save in the first two and last two bins where the pentadiagonal transformation must be modified.

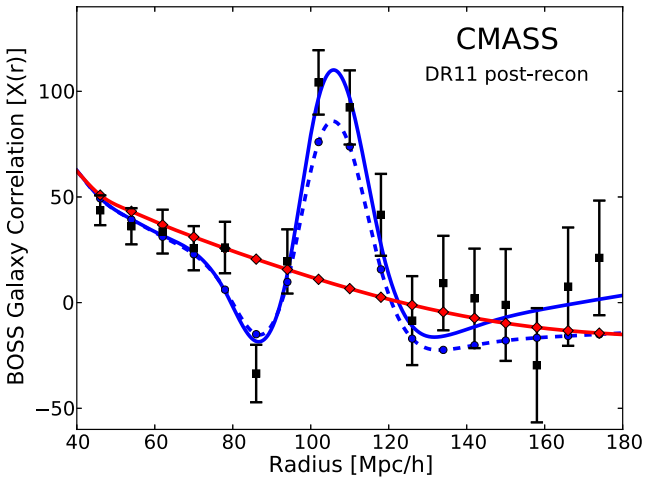

Figure 14. The DR11 CMASS correlation function, transformed as defined by equation (46) with $a = 0.30$ and $b = 0.10$. Unlike the usual correlation function, these error bars are nearly independent. The off-diagonal elements of the reduced covariance matrix deviate from zero only by an rms of 5 per cent, compared to 80 per cent covariance between neighbouring bins of the original correlation function. The blue solid line is the best-fitting BAO model with no marginalization of broad-band terms; the dashed line marginalizes over our standard quadratic polynomial. The red solid line is the best-fitting non-BAO model without marginalization; this model is rejected by $\Delta\chi^2 \approx 70$. We note that since the transformation is defined on the binned estimators, the models are formally not curves but simply predictions for the discrete estimators. We plot those predictions as the small dots; the curve is a spline connecting those dots.

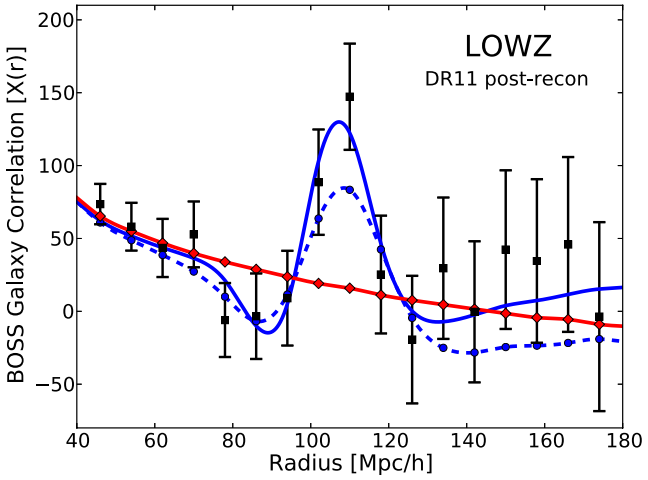

Figure 15. As Fig. 15, but for the DR11 LOWZ correlation function transformed as defined by equation (46) with $a = 0.39$ and $b = 0.04$. As before, these error bars are nearly independent, with a worst case of 12 per cent and an rms of 3.4 per cent in the off-diagonal elements of the reduced covariance matrix.

Downloaded from http://mnras.oxfordjournals.org/ at University of California, Irvine on March 16, 2016

Tridiagonal matrices have inverses with exponentially decreasing off-diagonal terms (Rybicki & Press 1995). Apparently, treating the off-diagonal covariances as exponentially decreasing with only weak dependences on separation provides a good approximation.

For $P(k)$, the measurements in k-bins are already fairly independent, as one would expect for a near-Gaussian random field. Correlations between bins can occur because of the finite survey volume and because of non-Gaussianity in the density field. For CMASS, we find the mean first off-diagonal term of the reduced covariance matrix is 0.28 (with a standard deviation of 0.06). When the $P(k)$ measurements are divided by the best-fitting smooth model, $P^{\rm sm}(k)$, they are, generally, even less correlated. We determine $P(k)/P^{\rm sm}(k)$ for each mock sample and construct a revised 'BAO' covariance matrix from this. We do not use this covariance matrix to perform any fits – our fits are to the full $P(k)$ and use the original covariance matrix. For the revised covariance matrix, the mean first off-diagonal term of the correlation matrix is reduced to 0.03 (with a standard deviation of 0.15). The diagonal elements within this covariance matrix are also reduced in amplitude, reflecting the smaller variance available once a smooth fit has been removed. The errors derived from this matrix thus better represent the errors on the measured BAO; the data when presented as $P(k)/P_{\rm sm}(k)$ are more independent and provide a more accurate visualization of the measurements.

Fig. 16 displays the measured post-reconstruction values of $P(k)/P^{\rm sm}(k)$, for the BOSS CMASS sample in DR9, DR10, and DR11 (from top to bottom), showing the evolution in the signal-to-noise ratio of the BAO as BOSS has increased its observed footprint. In the DR11 sample, the third peak is clearly visible. In Fig. 17, we display the DR11 post-reconstruction $P(k)/P^{\rm sm}(k)$ for the two BOSS samples; the CMASS sample at $z_{\rm eff} = 0.57$ is presented in the top panel and the LOWZ sample at $z_{\rm eff} = 0.32$ is shown in the bottom panel. The LOWZ sample possesses a clear BAO feature, but the signal-to-noise ratio is considerably lower than that of the CMASS sample.

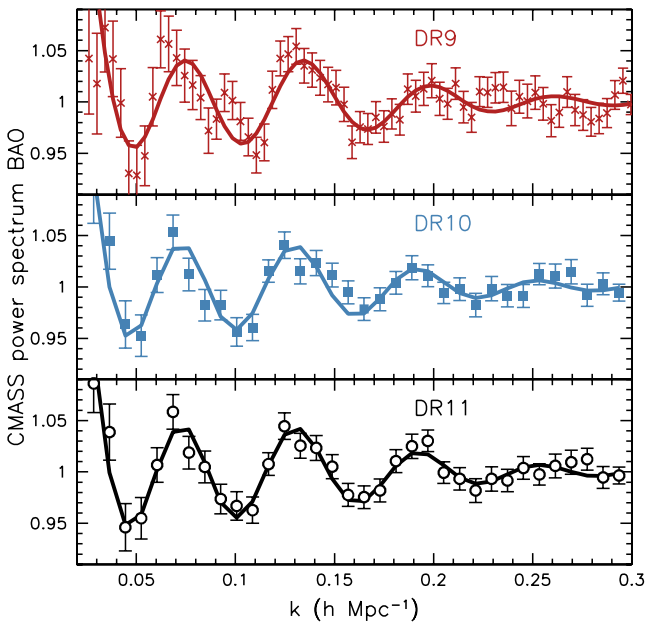

Figure 16. The CMASS BAO feature in the measured reconstructed power spectrum of each of the BOSS data releases, DR9, DR10, and DR11. The data are displayed with points and error bars and the best-fitting model is displayed with the curves. Both are divided by the best-fitting smooth model. We note that a finer binning was used in the DR9 analysis.

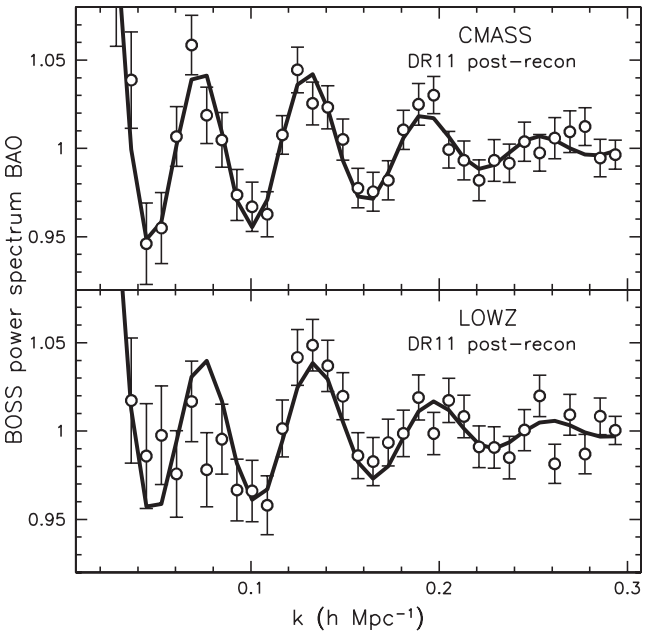

Figure 17. The BAO feature in the measured power spectrum of the DR11 reconstructed CMASS (top) and LOWZ (bottom) data. The data are displayed with black circles and the best-fitting model is displayed with the curve. Both are divided by the best-fitting smooth model.

7 BAO MEASUREMENTS FROM ANISOTROPIC CLUSTERING ESTIMATES

7.1 Anisotropic clustering estimates

In Section 5, we detailed our analysis techniques (multipoles and wedges statistics), and demonstrated they recover unbiased estimates of the BAO scales both along and perpendicular to line of sight with similar uncertainties. We now apply these two techniques to BOSS CMASS sample (at $z = 0.57$). Fig. 18 displays the multipoles, $\xi_{0,2}$, of the DR11 CMASS sample correlation function pre- and post-reconstruction, using our fiducial binning choice, for the range of scales fitted ($45 < s < 200\,h^{-1}$ Mpc). For the quadrupole (ξ_2), we see a dramatic change from the pre- to post-reconstruction results, as the reconstruction algorithm has removed almost all of the RSD contribution. Further, an apparent dip is now seen in the data on scales slightly larger than the peak in the monopole. The strength of this feature is related to the deviation in ϵ from 0 (or the deviation in $\alpha_\perp$ from 1).

Fig. 19 displays the correlation function divided into two wedges ($\xi_{||,\perp}$), once again with the pre-reconstruction measurements displayed in the top panel and the post-reconstruction measurements in the bottom panel. Reconstruction has made the BAO peak sharper for both $\xi_{||}$ and $\xi_\perp$. Further, reconstruction has decreased the difference in their amplitudes as the RSD signal has been reduced.

7.2 DR11 acoustic-scale measurement from anisotropic clustering

As for our isotropic analysis, the results of our anisotropic BAO fits to the DR10 and DR11 mocks show significant improvement on average with reconstruction (see Table 5), and therefore, we adopt post-reconstruction results as our default. Our consensus value for the CMASS anisotropic BAO measurement, $\alpha_{||} = 0.968 \pm 0.032$, $\alpha_\perp = 1.044 \pm 0.013$, is determined from a combination of the

Downloaded from http://mnras.oxfordjournals.org/ at University of California, Irvine on March 16, 2016

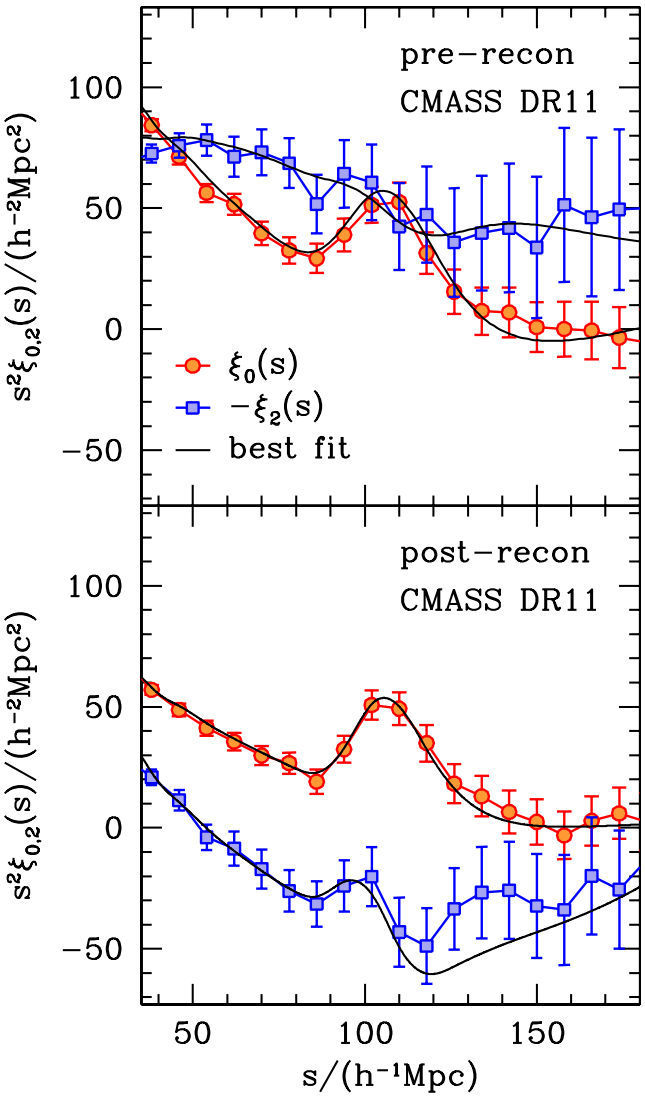

Figure 18. The DR11 multipole measurements along with their fits using the method described in Section 5. The top panel is pre-reconstruction while the bottom one is post-reconstruction.

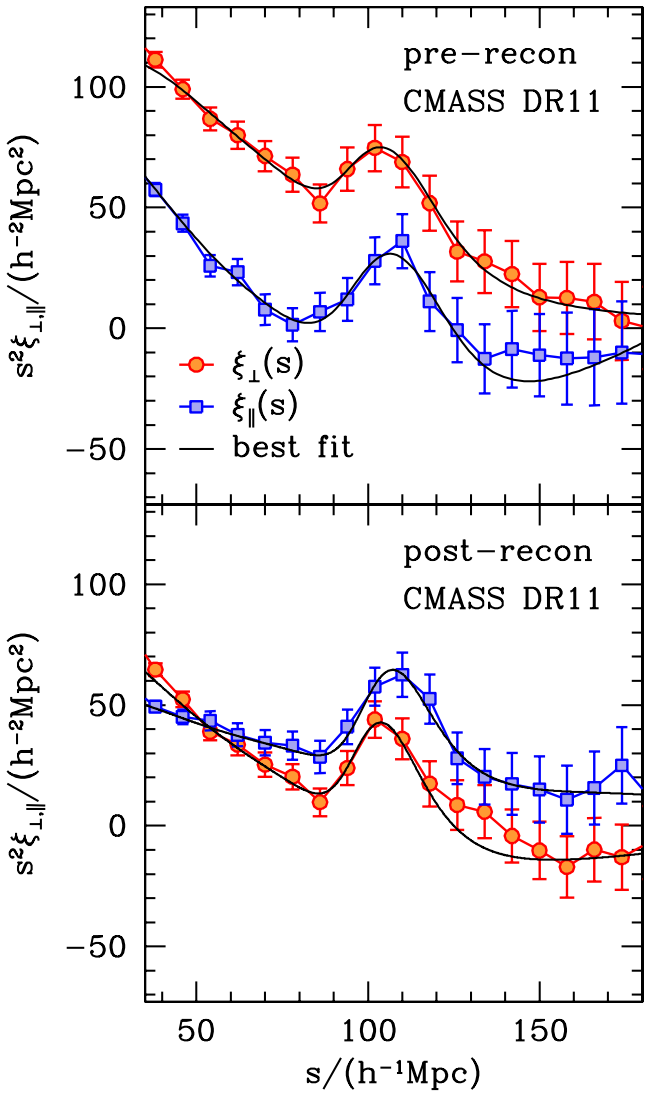

Figure 19. The DR11 wedge measurements along with their fits. The top panel is pre-reconstruction while the bottom one is post-reconstruction.

measurements using the multipoles and the wedges methodologies, and we describe the individual measurements and the process of arriving at our consensus measurement in what follows.

The curves in Figs 18 and 19 show the best-fitting BAO models[3] to the pre- and post-reconstruction data using the multipoles and wedges methodology. The fits, with characteristics listed in Table 10, provide a good description of the data for 30 dof: the largest χ^2 is 35 (a larger χ^2 would be expected 24 per cent of the time) and the smallest is 21 (a smaller χ^2 would be expected 11 per cent of the time).

The uncertainties on the anisotropic BAO measurements are typical of those we find in the mock samples. For the multipoles result, this is illustrated in Fig. 7, which shows that the uncertainties recovered from the data (orange stars) are within the range of those recovered from mock samples (blue points). The uncertainty on the BAO measurements using the wedges methodology are similar to the multipoles results, with a small increase for $\alpha_\perp$, that exactly matches that seen fitting mock catalogues. We further illustrate the constraints obtained from each method in Fig. 20 where one can see the comparison of the 60 and 95 per cent constraints in the D_A and $H(z)$ plane scaled by r^{fid}/r_d using the two methods. The size of the contours from both methods agree very well, with a slightly more elongated contour from multipoles, showing that the multipoles and wedges contain slightly different information.

The precision of the DR11 results are improved by reconstruction, as expected. This is illustrated in Fig. 20, where the post-reconstruction $D_A(z)$, $H(z)$ contours in the right-hand plot show a dramatic decrease compared to the pre-reconstruction results displayed in the left-hand panel. Based on our testing of 600 mock CMASS samples, we found (as shown in Fig. 7) that reconstruction is expected to improve the precision of the multipoles method measurement of $\alpha_\perp$ by ∼40 per cent (the median uncertainty decreases from 0.021 to 0.015) and of $\alpha_\parallel$ by 63 per cent (the median uncertainty decreases 0.044 to 0.027), with very similar results using the wedges methodology. We find that for the DR11 data, the results are similar to our expectation, as the improvements in the precision of the results gained by reconstruction are all between 39 and 50 per cent. The improvement in $\alpha_\perp$ (50 per cent for multipoles

[3] The best fits to both $\xi_\ell(r)$ where $\ell = 0, 2$ and $\ell = \parallel, \perp$, respectively.

Downloaded from http://mnras.oxfordjournals.org/ at University of California, Irvine on March 16, 2016

Table 10. Fits to anisotropic clustering measurements recovered from BOSS DR10 and DR11 pre- and post-reconstruction. We also show the fit to isotropic correlation function $\xi_0(s)$ for comparison (extracted from Table 7). The isotropic results we extracted refer to the one that we find closest in fitting methodology to the anisotropic fits. Therefore, the isotropic results here are fits to correlation functions only and without combining the bins across different bin centre choices. We include here anisotropic fits made using the 'De-Wiggled' template (see Anderson et al. 2014) since this matches the fit to the isotropic clustering measurements. It is not surprising that the α values fit from anisotropic clustering using this template are in even better agreement with the isotropic clustering measurement.

Model	α	ϵ	$\rho_{\alpha,\epsilon}$	$\alpha_{\parallel}$	$\alpha_{\perp}$	$\rho_{\alpha_{\parallel},\alpha_{\perp}}$	χ^2
DR11							
Consensus	$\mathbf{1.019 \pm 0.010}$	$\mathbf{-0.025 \pm 0.014}$	**0.390**	$\mathbf{0.968 \pm 0.033}$	$\mathbf{1.045 \pm 0.015}$	**−0.523**	–
Post-recons. Multipoles	1.017 ± 0.009	-0.033 ± 0.013	0.505	0.952 ± 0.031	1.051 ± 0.012	−0.311	21/30
Post-recon. Wedges	1.019 ± 0.010	-0.018 ± 0.013	0.389	0.982 ± 0.031	1.038 ± 0.014	−0.501	21./30
Post-recon. De-Wiggled	1.017 ± 0.009	-0.032 ± 0.013	0.512	0.952 ± 0.032	1.051 ± 0.012	−0.304	21/30
Post-recon. Isotropic	1.021 ± 0.009	–	–	–	–	–	16/17
Pre-recon. Multipoles	1.017 ± 0.013	-0.012 ± 0.019	0.495	0.992 ± 0.046	1.030 ± 0.017	−0.246	35/30
Pre-recon. Wedges	1.018 ± 0.015	-0.008 ± 0.018	0.236	1.001 ± 0.043	1.027 ± 0.021	−0.453	33/30
Pre-recon. De-Wiggled	1.025 ± 0.014	-0.010 ± 1.035	0.572	1.004 ± 0.049	1.035 ± 0.017	−0.149	33/30
Pre-recon. Isotropic	1.031 ± 0.013	–	–	–	–	–	14/17
DR10							
Consensus	$\mathbf{1.019 \pm 0.015}$	$\mathbf{-0.012 \pm 0.020}$	**0.502**	$\mathbf{0.994 \pm 0.050}$	$\mathbf{1.031 \pm 0.019}$	**−0.501**	-
Post-recon. Multipoles	1.015 ± 0.016	-0.020 ± 0.023	0.683	0.975 ± 0.058	1.037 ± 0.018	−0.240	16/30
Post-recon. Wedges	1.020 ± 0.015	-0.006 ± 0.019	0.513	1.009 ± 0.049	1.027 ± 0.018	−0.474	17/30
Post-recon. De-Wiggled	1.015 ± 0.016	-0.020 ± 0.023	0.669	0.974 ± 0.057	1.036 ± 0.018	−0.163	16./30
Post-recon. Isotropic	1.022 ± 0.013	–	–	–	–	–	14/17
Pre-recon. Multipoles	1.004 ± 0.016	-0.024 ± 0.025	0.439	0.956 ± 0.057	1.029 ± 0.024	−0.346	36/30
Pre-recon. Wedges	1.004 ± 0.018	-0.015 ± 0.022	0.104	0.975 ± 0.049	1.020 ± 0.028	−0.482	30/30
Pre-recon. De-Wiggled	1.012 ± 0.018	-0.021 ± 0.026	0.555	0.969 ± 0.063	1.035 ± 0.023	−0.237	35/30
Pre-recon Isotropic	1.022 ± 0.017	–	–	–	–	–	16/17

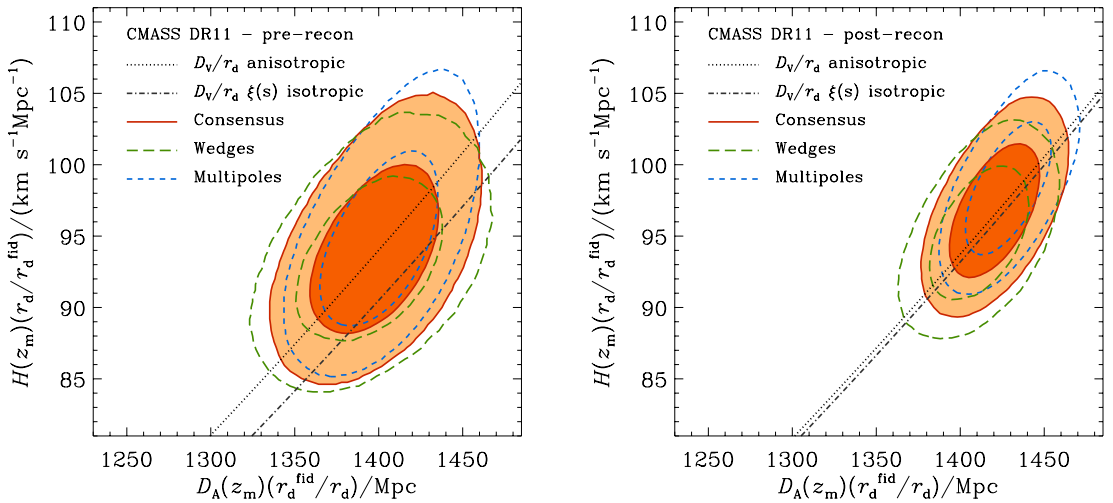

Figure 20. Comparison of the 68 and 95 per cent constraints in the $D_A(z)$–$H(z)$ plane scaled by (r_d^{fid}/r_d) obtained from multipoles gridded analysis (blue short-dashed line) and wedges (green long-dashed line), for DR11 pre-reconstruction (left) and post reconstruction (right). The solid contours are the consensus values issues from combining the $\log(\chi^2)$ from both approaches. The multipoles provide slightly tighter constraints, the consensus contours follow a more elongated form aligned with the axis of constant α. We also show the central values from fits of D_V/r_d from isotropic and anisotropic clustering. We note the slight difference between the isotropic and anisotropic constraints on D_V/r_d and the slight shift in direction of the contours of $D_A(z)$–$H(z)$ compared to $D_V(z)$. We note that anisotropic clustering measurements provide stronger cosmological constraints than isotropic clustering measurements. We thus adopt CMASS anisotropic values as our best cosmological data set (as discussed in both Sections 7.5 and 9.1) and will label it as 'CMASS' in subsequent sections.

and 42 per cent for wedges) is slightly better than expected and the improvement in $\alpha_{||}$ (39 per cent for multipoles and 48 per cent for wedges) is slightly worse, but Fig. 7 shows that the results (orange stars) are well within the range of the results determined from mock samples (blue points).

Table 10 shows that the DR11 post-reconstruction multipoles and wedges results disagree by close to 1σ: $\alpha_{\parallel,\,\mathrm{Mult}} = 0.952 \pm 0.031$, $\alpha_{\parallel,\,\mathrm{Wedges}} = 0.982 \pm 0.031$; $\alpha_{\perp,\,\mathrm{Mult}} = 1.051 \pm 0.012$, $\alpha_{\perp,\,\mathrm{Wedges}} = 1.038 \pm 0.012$. The difference in $\alpha_{\parallel}$ is 0.030. We then turn to the galaxy mock catalogues to see whether this behaviour is common. We find that 39 out of 600 mocks show the same or larger differences between the two methods. The mean difference is 0.005 with an rms of 0.016 suggesting that this difference in the data is a 1.9σ event. The difference in $\alpha_{\perp}$ is 0.013, we also found 45 out of

Downloaded from http://mnras.oxfordjournals.org/ at University of California, Irvine on March 16, 2016

Table 11. CMASS post-reconstruction DR11 results for several variations of the fitting models. We can see that the central values of $\alpha_\perp$ and $\alpha_\parallel$, and the errors around these best-fitting values are robust to the changes in methodology considered. Were we to extend the range of α and ϵ probed, then this would not be the case, and the derived errors would change. More details and further tests can be found in Vargas-Magana et al. (2013).

Method	α	ϵ	$\rho_{\alpha,\epsilon}$	$\alpha_{\|\|}$	$\alpha_\perp$	$\rho_{\|\|,\perp}$	χ^2/d.o.f	B_0	β
Fiducial	1.017 ± 0.009	-0.033 ± 0.013	0.505	0.952 ± 0.031	1.051 ± 0.013	-0.610	21./30	1.095	-0.096
Fitting $30 < r < 200$	1.019 ± 0.008	-0.030 ± 0.012	0.384	0.959 ± 0.028	1.050 ± 0.013	-0.638	36./30	1.113	0.028
Only B_0 prior	1.017 ± 0.010	-0.031 ± 0.014	0.580	0.955 ± 0.034	1.049 ± 0.013	-0.607	20./30	1.084	-0.199
Only β prior	1.016 ± 0.009	-0.034 ± 0.014	0.537	0.949 ± 0.032	1.052 ± 0.013	-0.622	20./30	1.106	-0.091
No priors	1.016 ± 0.010	-0.032 ± 0.015	0.612	0.953 ± 0.036	1.049 ± 0.013	-0.614	20./30	1.094	-0.190
Fixed $\beta = 0.0$	1.017 ± 0.008	-0.034 ± 0.012	0.447	0.949 ± 0.029	1.053 ± 0.012	-0.608	21./30	1.105	0.000
Two-term $A_0(s)$ and $A_2(s)$	1.017 ± 0.009	-0.025 ± 0.013	0.560	0.967 ± 0.031	1.044 ± 0.012	-0.555	37./30	1.048	-0.210
Four-term $A_0(s)$ and $A_2(s)$	1.016 ± 0.008	-0.034 ± 0.013	0.438	0.948 ± 0.029	1.052 ± 0.013	-0.601	16./30	1.094	-0.039

600 cases that show the same or larger differences between the two methods. The mean difference found in the mocks is 0.001 and the rms is 0.008; this suggests that the difference in the data is a 1.6σ event. This is mostly driven by differences in the fitted results of ϵ, Table 10 shows us that the fitted values of α from both methodologies only differ by 0.2 per cent, while ϵ is different by 1.5 per cent, which is comparable to the 1σ error on ϵ. We thus turn to a discussion using α-ϵ parametrization in the following discussion.

Pre-reconstruction, the multipoles and wedges measurements in α and ϵ differ by less than 0.25σ as shown in Table 10. Fig. 20 shows that, as reconstruction tightens the constraints from both methods, the central values shift slightly along the axis of constant α by 1.5 per cent in ϵ. When we look at this comparison in our mocks, we find an rms difference in ϵ fits of 0.007, indicating that the data is a 2σ outlier. 27 out of 600 mocks have differences more extreme than ± 0.015. The other three cases (DR10 and DR11 pre-reconstruction) show smaller variations. We conclude that this event is consistent with normal scatter of the two estimators.

Our tests on our fitting methodology, presented for the mock samples in Section 5.2 and on the DR11 data in Section 7.3, suggest no systematic issue causing the observed difference between the results of the two methods. Thus, we combine the likelihood distributions recovered from the multipoles and wedges measurements, using the method described in Section 5.3, to recover our consensus anisotropic BAO measurement, $\alpha_\perp = 1.045 \pm 0.015$ and $\alpha_\parallel = 0.968 \pm 0.033$. We quote the statistical and systematic error[4] here for consensus values, while the remaining values in Table 10 consider only the statistical errors.

7.3 Robustness checks on data

We measure the DR11 post-reconstruction anisotropic BAO scale with various choices of methodology, in order to test the robustness of our anisotropic BAO measurements. Because of the tight correlation between results calculated from fits to either multipoles or wedges (see Section 5.2), we only present robustness checks for fits to the multipoles. We have only summarized the results of the robustness that are of immediate relevance to this paper here, while the full robustness test of our anisotropic BAO fitting methodology is shown in Vargas-Magana et al. (2013).

We vary the choices when fitting to the data in the same way as we did when testing the results on the mock samples in Section 5.2. The results are summarized in Table 11, and we can see that the differences in central fitted values when we consider different choices of fitting parameters are impressively small. The central fitted values of α vary less than 0.1 per cent, while the various fitted errors vary less than 0.2 per cent. For all cases but one, the central fitted values of ϵ vary less than 0.2 per cent, while the fitted errors vary less than 0.2 per cent. The largest variation found is on ϵ when we change the broad-band polynomial such that each component ($A_\ell(s)$) is only limited to two-terms, which is still relatively small, at 0.8 per cent, which is less than 0.6σ. We can turn our attention to $\alpha_\parallel$ and $\alpha_\perp$, but as expected, since the variations are not large for α and ϵ, the changes in $\alpha_\parallel$ and $\alpha_\perp$ are equally small.

We also investigate the effects of priors. We refer the reader to the priors listed in Section 5.1. In both mocks and data of DR11 post-reconstructed, we find that as long as we either limit the ϵ to reasonable physical intervals when we calculate the error or use priors on both β and B_0, the final fitted central values and errors remain relatively unchanged to within 0.1 per cent. We have discussed this further in a companion paper (Vargas-Magana et al. 2013), which should be consulted for more details. Finally, it is also interesting to note that a fixed β parameter does not change the error or central values by more than 0.1 per cent. To conclude, the variations of DR11 post-reconstructed data are well within the scatter predicted when the same varying choices are applied to mock galaxy catalogues.

7.4 DR10 anisotropic BAO measurement

Although our default results are for DR11, it is instructive to examine the results from the reduced DR10 data set, which allow us to follow the transition in data quality from our previous DR9 results to our new DR11 results. Consequently, we present anisotropic BAO measurements from DR10 alongside the DR11 measurements in Table 10. For the mock catalogues, Fig. 7 showed that, for fits to the DR10 multipoles, the expected improvement of the measurement in $\alpha_\perp$ and $\alpha_\parallel$ with reconstruction is from 2.8 and 5.4 per cent to 1.9 and 3.6 per cent, respectively. Using the DR10 data, we measure $\alpha_\perp = 1.039 \pm 0.024$ and $\alpha_\parallel = 0.956 \pm 0.057$ pre-reconstruction. Post-reconstruction, we measure $\alpha_\perp = 1.037 \pm 0.018$ and $\alpha_\parallel = 0.975 \pm 0.058$, showing remarkable consistency with the mock results. The measurement using wedges, also presented in Table 10, are similar and consistent. Thus, the precision of the BAO measurements from the DR10 data are typical. This can also be seen in Fig. 7, where the orange star representing the data results is within the locus of the blue circles representing results from the mocks.

It is interesting that, for DR10, the error post-reconstruction is slightly larger for $\alpha_\parallel$, compared with the pre-reconstruction error. We can see this more clearly by looking at the α and ϵ pair

[4] The systematic errors are described in Sections 7.3 and 8.1. The addition of the two types of error is described in Section 8.1.

Downloaded from http://mnras.oxfordjournals.org/ at University of California, Irvine on March 16, 2016

pre- and post-reconstruction in DR10 in Table 10. It seems there is no improvement in σ_α, while there is some slight improvement in σ_ϵ post-reconstruction. We compare this to the mocks to try and understand this behaviour. Fig. 7 shows that not all mocks in DR10 have improved constraints on $\alpha_\parallel$ after reconstruction, even though it is uncommon: ≈20 out of 600 mocks that do not improve. We do see improvement on nearly all mocks in DR11, which may be due to the fact that DR11 has a more contiguous mask, so that there is less volume close to boundaries. This may contribute to a more successful reconstruction in DR11.

7.5 Comparison with isotropic results

For ease of comparison between our isotropic and anisotropic measurements, we include the results from isotropic fits to the correlation function (presented in Table 7) in Table 10. Post-reconstruction, the central values of α measured from isotropic and anisotropic clustering are consistent to well within 1σ. Pre-reconstruction, the central values of α from the isotropic correlation function are approximately 1σ higher than α from the anisotropic clustering, for both DR10 and DR11. Part of this difference can be explained by the different correlation function templates used for the isotropic and anisotropic analyses. The anisotropic fitting uses $P_{\rm pt}(k)$ as described in equation (38) which was chosen as it provides less biased measured values of α and ϵ fitting, while the isotropic fitting uses a non-linear power spectrum 'De-Wiggled template' (Anderson et al. 2012, 2014). The differences though between the templates are quite small and are further explored in Vargas-Magana et al. (2013). For comparison, we provide anisotropic fits made using the same 'De-Wiggled' power spectrum template used for the isotropic fits in Table 10; it is not surprising that the anisotropic results with the same power spectrum template provide more similar fits to those from the isotropic fits in both pre-reconstruction and post-reconstruction data sets (this is explored further in Vargas-Magana et al. 2013).

For DR11 post-reconstruction, which is our default choice for making cosmological measurements, we note that the isotropic power spectrum fits give lower values of α than the isotropic correlation function fits, pulling the isotropic consensus values of α down (see Table 9). On the other hand, the correlation function monopole measurement of α agrees very well with the α values measured from anisotropic fits to both the monopole and the quadrupole. They are both higher than the consensus value of the isotropic fits (a combination of both isotropic power spectrum fit and the correlation function fit), and the effect of this is noticeable when the measurements are combined with the CMB data and turned into cosmological constraints (see Fig. 23 and Section 9.2).

Isotropic fits of α only allow us to measure the spherically averaged distance $D_V(z) \propto D_{\rm A}^2(z)/H(z)$, where z is the median redshift of the sample. This has made the approximation that the clustering of the galaxy sample is isotropic. More importantly, the Hubble parameter $H(z)$ is degenerate with $D_{\rm A}(z)$ in this isotropic measurement, and thus we cannot directly probe the expansion of the Universe. The clustering of galaxies is not truly isotropic due to both large-scale RSD and from assuming the wrong cosmology when we calculate the two-point statistics. Therefore, the fit to the anisotropic clustering provides more information by breaking the degeneracy between $H(z)$ and $D_{\rm A}(z)$. We are therefore not surprised that the anisotropic clustering measurements provides stronger cosmological constraints as demonstrated by the different contour sizes in Fig. 23. We further compare and contrast the isotropic and anisotropic fits in Fig. 20. While on average the anisotropic degeneracy direction should lie along the isotropic (D_V) direction, in our data set the orientation is closer to vertical. This slight rotation is driven by the shot-noise differences along the line of sight and perpendicular to the line of sight. This is expected, given the comparison of the data and ensemble of mock constraints on $\alpha_\perp$ and $\alpha_\parallel$ shown in Fig. 7. This figure also illustrates the 0.5 per cent increase in the best-fitting α from the anisotropic fits compared with the isotropic ones. Anisotropic clustering's constraining power is also amplified depending on the models we explore. For example, variation in dark energy equation of state (w) shifts $D_{\rm A}$ at fixed CMB acoustic scale, and anisotropic clustering measurements provide stronger constraints than isotropic ones in the direction of $D_{\rm A}$ (Fig. 20).

Therefore, we choose the anisotropic clustering measurements to be the default measurement of the CMASS measurement in our cosmological analysis (thus will only be referred to as CMASS in later sections).

8 THE COSMOLOGICAL DISTANCE SCALE

8.1 Systematic errors on BOSS BAO measurements

Sections 4 and 5 presented the acoustic-scale fits and their statistical errors. Here, we present estimates of systematic errors, which we believe to be subdominant by a considerable margin. We organize the discussion into two separate classes of systematic errors. The first set includes possible artefacts from our survey, including the effects of survey boundaries and observational systematics on the reconstruction and fitting methodology. The second set concerns the possible residual effects of galaxy clustering bias on the shift of the acoustic scale after one applies our reconstruction algorithm assuming a large filled survey.

As shown in Table 4, when run on our mock catalogues, the estimators for both the spherically averaged correlation function and the power spectrum return unbiased results in DR11 after reconstruction, with precision of 0.04 per cent in the mean. Tables 5 and 6 show that when we run our different estimators (Multipoles and Wedges) for the anisotropic clustering signals on mock catalogues they return unbiased results in DR11 both pre-reconstruction and post-reconstruction. This is an extremely sharp test, as it includes the effects of the survey geometry and ability of reconstruction to remove the non-linear shifts of the acoustic scale that arise from Lagrangian perturbation theory as used in our mocks. It also validates our fitting methodology, e.g., demonstrating that effects of binning, interpolation, and integrations in the measurement and fitting procedures have been handled well. Ross et al. (2014) use two other sets of mocks, using the same formalism as Manera et al. (2013a) but with different halo mass cuts; they find similar unbiased performance after reconstruction, with precision better than 0.1 per cent.

The effects of variations in the fitting methodology was discussed in Sections 6 and 7, showing only small offsets, at the level of 0.1–0.2 per cent in α for cases that were expected to agree. Anderson et al. (2012, 2014) and Vargas-Magana et al. (2013) present further tests, again finding no substantial offsets.

One can also search for systematic errors by comparing different aspects of our analysis. Indeed, we do find cases in which different analyses of the same data return acoustic scales that differ by of order 0.5 per cent, e.g., the comparison of the α measured from ξ and P in DR11. However, these discrepancies occasionally occur in our mock catalogues and hence are not sufficiently unusual to indicate a systematic error, particularly because we examined a substantial number of these comparisons, many of which were unremarkable.

Downloaded from http://mnras.oxfordjournals.org/ at University of California, Irvine on March 16, 2016

If these differences are indeed due to systematic effects, then it must be for reasons that are not present in our mock catalogues, as each of our estimators is unbiased when averaged over many mocks.

The mocks do not include large-angle observational systematics due to such things as variations in star–galaxy separation effectiveness or seeing, as were discussed in Ross et al. (2012). However, the acoustic peak measurement is highly robust to such effects, as they tend to have smooth angular power spectra. One would expect that if such effects were present, they would be much more severe if we omitted the broadband nuisance terms described in Section 4. As shown in Section 6, performing our correlation function fits with fewer or even none of the three broad-band nuisance terms produces changes in α of 0.2 per cent or less. Removing two terms from the power spectrum fit also changes the answer by only 0.2 per cent.

Although we measure the clustering within a redshift bin of non-zero thickness, we interpret the fitted scale as measuring the distance to a single effective redshift. We base this estimate on the mean redshift of fully weighted pairs, rounded off for simplicity. This effective redshift is not formally well defined – for example, it might depend on scale or differ between line-of-sight and transverse clustering – but different reasonable choices vary by only 0.01 in redshift. We then expect the effect of this assumption to be small because any error in the effective redshift enters only as the variation with redshift in the ratio of the true cosmology to the fiducial cosmology. For example, we will see in Section 9 that the ratio of D_V between the best-fitting ΛCDM model and a model with $w = -0.7$ that matches the CMB data varies by about 1 per cent for each 0.1 in redshift. This would be a 0.1 per cent shift for an 0.01 change in effective redshift. Yet this much tilt in the distance–redshift relation is already disfavoured by the BAO Hubble diagram and by the supernova data. Hence, we argue that errors in the effective redshift affect our interpretations at below 0.1 per cent.

Similarly, our mocks are based on a single redshift snapshot of the simulations, rather than light-cone outputs that track the exact structure at each redshift. This approach could create errors when we combine a broad redshift bin into one clustering measurement and interpret the acoustic peak as arising from a single, effective redshift. Note that the amplitude of galaxy clustering changes much more slowly than the predicted variation in the amplitude of the matter clustering, which limits the mismatch of combining different redshifts. Preliminary tests of this approximation with light-cone simulations in a few cases show the effects to be small, but we intend to extend these tests in the future.

The choice of fiducial cosmology also enters through the linear power spectrum used in our fitting. The assumption of our methodology is that the α values recovered from fits with other template spectra would be well predicted by the ratios of sound horizons computed in these cosmologies to that of the fiducial model. Were this not the case, we would simply have to repeat the fit for each new cosmology, searching for cases of $\alpha = 1$. This assumption has been investigated in previous papers and found to be a good approximation (Seo et al. 2008; Xu et al. 2012a,b), with systematic offsets typically at or below 0.1 per cent in α. One exception was presented in Xu et al. (2012a), where a case with an extra relativistic neutrino species created an uncorrected 0.5 per cent shift of α due to template mismatches. Hence, more exotic cosmologies may require additional consideration of whether the sound horizon fully captures the impact of the variation in the fitting template.

Our conclusion from these tests is that there is no evidence for systematic errors from the survey effects and fitting above the 0.1 per cent rms level from any effect we have considered. However, there are several such terms that could accumulate, so we triple this to adopt a systematic error of 0.3 per cent for our measurements of D_V. We believe that further tests on a more diverse and realistic set of mock catalogues would boost confidence in the methods at the 0.1 per cent aggregate level.

The analysis of the anisotropic BAO could be subject to additional systematic errors due to the above effects. The anisotropic fitting is more complicated because of redshift distortions and the inherent anisotropy of the survey geometry and light-cone effects. Our tests on mock catalogues show the estimators to be unbiased at the level of 0.2 per cent in ϵ. Vargas-Magana et al. (2013) present an exhaustive set of tests of the multipole fitting method; Xu et al. (2012b), Anderson et al. (2014), and Kazin et al. (2013) present a wide variety of tests on earlier data sets. For the DR11 post-reconstruction case, Vargas-Magana et al. (2013) find variations in ϵ at the 0.1–0.2 per cent level as the parameters in the fitting method are varied. We take these results to indicate a 0.3 per cent rms systematic uncertainty in ϵ due to fitting. We increase this estimate to 0.5 per cent to include possible errors in the anisotropic BAO external to our mocks, e.g., due to light-cone effects, evolution in the sample, inaccuracies in assumptions about peculiar velocities in the mocks or reconstruction, or mismatches between our fiducial cosmology and the true one.

Our estimate of statistical error does depend on the assumption that the amplitude of clustering in the mocks matches that in the true data, as the sample variance of the density field depends on its power spectrum. Our current mocks have about 10 per cent less power than the data, which might lead to a small underestimate of the sample variance in the correlation function. The variance of the power spectrum analysis would actually be slightly overestimated because the covariance matrix was computed for $\ln P$ and hence includes only the fractional error on the power. The fractional error would be somewhat larger because of the increased importance of shot noise relative to a weaker clustering signal. The fact that the effects of a mismatch in clustering amplitude have opposite effects on the estimated errors in ξ and P, combined with the result that the uncertainties in α recovered from each statistic match closely, further argues that this effect is small. At present, we make no correction to our statistical error bars for the offset of clustering amplitude in our mocks, as the mismatch is small and the exact size of the resulting correction not well known. We also do not include a term in our systematic errors for possible mismatches of the amplitude of clustering, as this does not represent a bias in the mean, but rather an error on the error.

We next turn to systematic errors from true astrophysical shifts due to non-linear structure formation and galaxy clustering bias. Prior to reconstruction, one can see the small expected shift, of order 0.4 per cent, in the fitting of the mocks. From perturbation theory (Crocce & Scoccimarro 2008; Padmanabhan & White 2009) and simulations (Padmanabhan & White 2009; Seo et al. 2010), we expect shifts in the clustering of matter at 0.2–0.25 per cent at these redshifts. Galaxy bias produces additional small shifts (Padmanabhan & White 2009; Mehta et al. 2011). As reconstruction improves due to the larger and more contiguous survey volume, we expect it to remove the shifts due to large-scale velocities. Mehta et al. (2011) found no example in their models in which the shift after reconstruction was non-zero, with errors of about 0.1 per cent rms. The mock catalogues used here, as well as the two in Ross et al. (2014), also show no offsets at this level. Of course, our mock catalogues and the galaxy bias models of Mehta et al. (2011) do not span all possibilities, but there is a good physical reason why reconstruction is successful at removing shifts: in a wide range of bias models, the galaxy density field is proportional to the dark matter density

Downloaded from http://mnras.oxfordjournals.org/ at University of California, Irvine on March 16, 2016

field at scales above 10 Mpc. The shifts in the acoustic scale arise in second-order perturbation theory due to large-scale flows, which are well predicted by the galaxy maps. Reconstruction substantially reduces the flows and hence the source of the acoustic-scale shifts. To be conservative, we triple the level of uncertainty implied by our current mocks and adopt a systematic error of 0.3 per cent in α for shifts from galaxy bias that are not corrected by reconstruction.

Our systematic error budget for galaxy clustering bias does not encompass offsets that could result from the effects of relative streaming velocities between baryons and dark matter in the earliest collapse of protogalaxies (Tseliakhovich & Hirata 2010). Although this effect is large at the cosmological Jeans scale of $10^6\,M_\odot$ halos, the galaxies we measure in BOSS occupy halos over a million times larger and one might imagine that the impact of the early streaming velocities have been significantly diluted. Empirically, a recent paper by Yoo & Seljak (2013) limited the acoustic-scale shifts from this effect through its impact on the large-scale DR9 power spectrum; they found a remaining rms uncertainty of 0.6 per cent. While we look forward to more work on the possible effects of relative streaming velocities, we do not inflate our systematic errors by this much, as theories often predict the effect to be negligible at mass scales well above the cosmological Jeans scale (see e.g. McQuinn & O'Leary 2012).

To summarize, for our isotropic analysis, we adopt systematic errors of 0.3 per cent for fitting and survey effects and 0.3 per cent for unmodelled astrophysical shifts. These are applied in quadrature. These systematic errors increase the error on the CMASS consensus D_V value from 0.9 per cent to 1.0 per cent and the error on the LOWZ consensus value D_V from 2.0 to 2.1 per cent. For the anisotropic analysis, we apply the above effects in quadrature to α and then add an additional independent systematic error of 0.5 per cent in quadrature to ϵ. The impact on the measurement of D_A and H is subdominant to the statistical errors.

8.2 The distance scale from BOSS BAO

As described in Anderson et al. (2012) and Anderson et al. (2014), the value of α is directly related to the ratio of the quantity $D_V(z)/r_d$ to its value in our fiducial model:

$$D_V/r_d = \alpha\,(D_V/r_d)_{fid}\,. \tag{47}$$

Similarly, $\alpha_\perp$ and $\alpha_\parallel$ measure the ratios of D_A/r_d and r_d/H, respectively, to their values in our fiducial model.

We opt to quote our results by writing these quantities as

$$D_V(z_{eff}) = \alpha D_{V,fid}(z_{eff})\left(\frac{r_d}{r_{d,fid}}\right), \tag{48}$$

$$D_A(z_{eff}) = \alpha_\perp D_{A,fid}(z_{eff})\left(\frac{r_d}{r_{d,fid}}\right), \tag{49}$$

$$H(z_{eff}) = \alpha_\parallel H_{fid}(z_{eff})\left(\frac{r_{d,fid}}{r_d}\right). \tag{50}$$

With this form, we emphasize that only the ratio of r_d between the adopted and fiducial cosmology matters. There are a variety of possible conventions and fitting formulae available for r_d; any of these can be used so long as one is consistent. Moreover, within the usual class of CDM cosmologies, the CMB data sets tightly constrain r_d. For example, the Planck Collaboration (2013b) results imply r_d to 0.4 per cent rms precision for the minimal ΛCDM model and extensions to spatial curvature and low-redshift dark energy. As this is somewhat tighter than our statistical errors on the α, it is reasonable to choose a form of the results that emphasizes the absolute measurement of the distance scale.

The effective redshift of CMASS is $z_{eff} = 0.57$, while that of LOWZ is $z_{eff} = 0.32$. Our fiducial cosmology is $\Omega_m = 0.274$, $H_0 = 70\,km\,s^{-1}\,Mpc^{-1}$, $\Omega_b h^2 = 0.0224$, $n_s = 0.95$, $m_\nu = 0\,eV$, $w = -1$, $\Omega_K = 0$, and $\sigma_8 = 0.8$. Using this cosmology, we obtain $D_{V,fid}(0.57) = 2026.49\,Mpc$, $D_{A,fid}(0.57) = 1359.72\,Mpc$, and $H_{fid}(0.57) = 93.558\,km\,s^{-1}\,Mpc^{-1}$ for CMASS. For LOWZ, we have $D_{V,fid}(0.32) = 1241.47\,Mpc$, $D_{A,fid}(0.32) = 966.05\,Mpc$, and $H_{fid}(0.32) = 81.519\,km\,s^{-1}\,Mpc^{-1}$.

Inserting the constraints on α, we find the primary isotropic results of this paper:

$$D_V(0.57) = (2056 \pm 20\,Mpc)\left(\frac{r_d}{r_{d,fid}}\right) \tag{51}$$

$$D_V(0.32) = (1264 \pm 25\,Mpc)\left(\frac{r_d}{r_{d,fid}}\right) \tag{52}$$

for the post-reconstruction DR11 consensus values. For the anisotropic CMASS fit, we find

$$D_A(0.57) = (1421 \pm 20\,Mpc)\left(\frac{r_d}{r_{d,fid}}\right), \tag{53}$$

$$H(0.57) = \left(96.8 \pm 3.4\,km\,s^{-1}\,Mpc^{-1}\right)\left(\frac{r_{d,fid}}{r_d}\right), \tag{54}$$

with a correlation coefficient between D_A and H of 0.539 (in the sense that higher H favours higher D_A). As described in Section 7.5, we recommend the anisotropic values as our primary result at $z = 0.57$ when fitting cosmological models.

When applying these constraints to test cosmology, one must of course consider the variation in the sound horizon in the models. Our fiducial cosmology has a sound horizon $r_{d,fid} = 153.19\,Mpc$ if one adopts the definition in equations 4– 6 of Eisenstein & Hu (1998, hereafter, EH98). Alternatively, if one adopts the definition of the sound horizon in CAMB, one finds $r_{d,fid} = 149.28\,Mpc$, which is 2.6 per cent less. Much of the past BAO literature uses the EH98 convention, but we now recommend using CAMB as it provides a transparent generalization to models with massive neutrinos or other variations from vanilla CDM. As discussed in Mehta et al. (2012), the ratio of the EH98 and CAMB sound horizons is very stable as a function of $\Omega_m h^2$ and $\Omega_b h^2$, varying by only 0.03 per cent for the range $0.10 < \Omega_c h^2 < 0.13$ and $0.020 < \Omega_b h^2 < 0.023$. Thus, in evaluating the ratios that appear in our expressions for D_V, D_A, and H, the choice is largely irrelevant. We further find that for $0.113 < \Omega_c h^2 < 0.126$, $0.021 < \Omega_b h^2 < 0.023$, and $m_\nu < 1\,eV$, the approximation of

$$r_d = \frac{55.234\,Mpc}{(\Omega_c h^2 + \Omega_b h^2)^{0.2538}(\Omega_b h^2)^{0.1278}(1+\Omega_\nu h^2)^{0.3794}} \tag{55}$$

matches CAMB to better than 0.1 per cent, whatever the mass hierarchy. One can use any of these conventions for the sound horizon in applying our results, so long as one is consistent in evaluating r_d and $r_{d,fid}$.

For comparison to past work, using the EH98 sound horizon, we find $D_V(0.57)/r_d = 13.42 \pm 0.13$ and $D_V(0.32)/r_d = 8.25 \pm 0.16$. Using the CAMB sound horizon instead, this shifts to $D_V(0.57)/r_d = 13.77 \pm 0.13$ and $D_V(0.32)/r_d = 8.47 \pm 0.17$.

Finally, for the DR10 consensus values, we find

$$D_V(0.57) = (2055 \pm 28\,Mpc)\left(\frac{r_d}{r_{d,fid}}\right) \tag{56}$$

Downloaded from http://mnras.oxfordjournals.org/ at University of California, Irvine on March 16, 2016

Table 12. Comparison between the different CMASS-DR11 results. While our study focuses on the BAO information in the clustering signal, all other studies model the anisotropic broadband clustering in order to measure the cosmological distortion (Alcock & Paczynski 1979) and RSD. In addition to the differences in modeling, only the results of this paper use reconstruction. The α values from some of the other papers have been corrected to match our fiducial cosmological values.

Comparison between different CMASS-DR11 results				
Source	Method	α	$\alpha_\parallel$	$\alpha_\perp$
This analysis	Consensus	1.019 ± 0.010	0.968 ± 0.033	1.045 ± 0.015
Beutler et al. (2013)	$P(k)$-multipoles	1.023 ± 0.013	1.005 ± 0.036	1.021 ± 0.016
Samushia et al. (2014)	$\xi(s)$-multipoles	1.020 ± 0.013	1.013 ± 0.035	1.019 ± 0.017
Chuang et al. (2013b)	$\xi(s)$-multipoles	1.025 ± 0.013	0.996 ± 0.031	1.039 ± 0.019
Sánchez et al. (2013b)	$\xi(s)$-wedges	1.011 ± 0.013	1.001 ± 0.031	1.016 ± 0.019

$$D_V(0.32) = (1275 \pm 36\,\mathrm{Mpc}) \left(\frac{r_\mathrm{d}}{r_\mathrm{d,fid}} \right), \quad (57)$$

$$D_\mathrm{A}(0.57) = (1386 \pm 26\,\mathrm{Mpc}) \left(\frac{r_\mathrm{d}}{r_\mathrm{d,fid}} \right), \quad (58)$$

$$H(0.57) = \left(94.1 \pm 4.7\,\mathrm{km\,s^{-1}\,Mpc^{-1}}\right) \left(\frac{r_\mathrm{d,fid}}{r_\mathrm{d}} \right). \quad (59)$$

8.3 Comparison with other DR11 studies and past work

We next compare these distance measurements to prior results in the literature. First, we note that the CMASS results from DR9, DR10, and DR11 are in close agreement. DR10 and DR11 are double and triple the survey volume of DR9, respectively, and the survey geometry has become substantially more contiguous. For the consensus values for DR9 after reconstruction, Anderson et al. (2012) found $\alpha = 1.033 \pm 0.017$, in good agreement with the DR10 value of $\alpha = 1.014 \pm 0.014$ and DR11 value of $\alpha = 1.0144 \pm 0.0098$. The DR9 anisotropic analysis of Anderson et al. (2014) found $\alpha = 1.024 \pm 0.029$, also in good agreement with our results.

Similarly, the new values are in good agreement with DR9 analyses that utilized the whole broadband correlation function and power spectrum, without the broadband marginalization of the BAO-only analysis. In particular, by fitting the full anisotropic clustering, these analyses are sensitive to the Alcock & Paczynski (1979) distortion of the broadband clustering, which gives additional information on the product $D_\mathrm{A}(z)H(z)$. This requires modeling to separate from the RSD. Reid et al. (2012) model the monopole and quadrupole moments of the redshift-space DR9 correlation function above $25\,h^{-1}$ Mpc and find $D_V(0.57) = (2070 \pm 46)$ Mpc when allowing $f\sigma_8$, D_A, and H as free parameters in the fit. Kazin et al. (2013) also use the correlation function, but fit to clustering wedges rather than the multipoles. They found consistent values. Sánchez et al. (2013b) also analyzed the correlation function of the DR9 CMASS sample using clustering wedges, fitting to the data above $44\,h^{-1}$ Mpc, but combined their constraints with those derived from other BAO measurements, CMB, and SNe data. Their inferences are entirely consistent with the other DR9 measurements. Finally, Chuang et al. (2013a) also constrained cosmology from the DR9 CMASS correlation function, finding $D_V(0.57) = (2072 \pm 53)$ Mpc. These analyses are all clearly consistent with each other and with the more precise values we find for DR11.

Similar analyses of the additional cosmological information residing in the anisotropic broadband clustering have again been performed for the CMASS DR11 sample. These are presented in a series of companion papers. Beutler et al. (2013) analyses the power spectrum multipoles to measure the BAO signal as well as RSD using the clustering model of Taruya et al. (2010). Samushia et al. (2014) and Chuang et al. (2013b) use correlation function multipoles, also including additional information from RSD. While Samushia et al. (2014) uses the model suggested by Reid & White (2011), Chuang et al. (2013b) uses a model suggested by Eisenstein et al. (2006), Crocce & Scoccimarro (2006), and Matsubara (2008). Sánchez et al. (2013b) analyses the correlation function wedges together with external data sets to constrain a wide variety of cosmological parameters. We compare the various results in Table 12, finding good agreement with those of this paper. The agreement on α is close in most cases, while our BAO results differ by about 1σ when split anisotropically. Perfect agreement is not expected: these analyses are gaining additional information on $D_\mathrm{A}(z)H(z)$ from anisotropies in the broadband shape, but none of them use reconstruction. Given the difference in these treatments and the range of clustering statistics and template modeling, we are encouraged by this level of agreement.

Anderson et al. (2012) compared the DR9 CMASS distance measurement to that from the acoustic-scale measured by 6dFGS (Beutler et al. 2011), WiggleZ (Blake et al. 2011) and from the BAO detections in SDSS-III imaging data (Padmanabhan et al. 2007; Carnero et al. 2012; Seo et al. 2012). Our DR11 measurement remains in good agreement, within 1σ, with these studies.

The LOWZ measurements may be compared to previous work on the SDSS-II Luminous Red Galaxy sample, which covered a similar area of sky but with fewer galaxies. We find very close agreement with the results of Percival et al. (2010) and Padmanabhan et al. (2012). The survey footprints of these studies overlap substantially, but not entirely, with those of DR11 LOWZ. Moreover, Percival et al. (2010) included substantial volume at lower redshift through the SDSS-II MAIN sample (Strauss et al. 2002) and 2dFGRS data sets (Colless et al. 2003); this resulted in an effective redshift of $z = 0.275$. Both Percival et al. (2010) and Padmanabhan et al. (2012) used the SDSS-II LRG sample out to $z = 0.47$. Padmanabhan et al. (2012) used density-field reconstruction, while Percival et al. (2010) did not. However, the results are all similar, with differences that are well within 1σ. For example, Padmanabhan et al. (2012) measure $D_V(0.35)/r_\mathrm{d} = 8.88 \pm 0.17$; if we adjust this to $z = 0.32$ using the best-fitting ΛCDM model and convert to α, we find $\alpha = 1.012 \pm 0.019$, very similar to the DR11 LOWZ value of $\alpha = 1.018 \pm 0.021$.

Previous analyses of the SDSS-II LRG sample have measured the anisotropic BAO to determine D_A and H separately (Okumura et al. 2008; Gaztanaga et al. 2009; Chuang & Wang 2011; Xu et al. 2012b). As we have not yet done an anisotropic analysis with LOWZ, we cannot directly compare to these works. However, all of these works inferred cosmological parameters in good agreement

Downloaded from http://mnras.oxfordjournals.org/ at University of California, Irvine on March 16, 2016

with what we find in Section 9, indicating that the distance scales are compatible.

9 COSMOLOGICAL PARAMETERS

9.1 Data sets and methodology

We next consider the cosmological implications of our distance-scale measurements. From BOSS, we consider several different measurements. First, we have the $D_V(0.57)$ measurement from CMASS galaxy clustering in each of DR9, DR10, and DR11. Secondly, we have the $D_V(0.32)$ measurement from LOWZ clustering in DR10 and DR11. Finally, we have the $D_A(0.57)$ and $H(0.57)$ joint measurement from CMASS in DR11. In all cases, we use the post-reconstruction consensus values. When not stated, we refer to the DR11 measurement. We adopt the CMASS anisotropic values as our best cosmological data set, labelling this as 'CMASS', but also show results for the isotropic fit, labelling this as 'CMASS-iso'.

At points, we combine our CMASS and LOWZ measurements with two other BAO detections at different redshifts: the measurement of D_V at $z = 0.10$ from the 6dFGS (Beutler et al. 2011) and the measurement of D_A and H at $z = 2.3$ in the Lyman α forest in BOSS (Busca et al., 2013; Kirkby et al. 2013; Slosar et al. 2013). These will be labelled as '6dF' and 'LyαF', and the union the BAO data sets will be labelled in plots as 'BAO'.

As discussed in the previous section, our BOSS galaxy BAO measurements are consistent with those from the WiggleZ survey (Blake et al. 2011; Kazin et al. 2014) at $z = 0.44$, 0.60, and 0.73 and with earlier SDSS-II LRG analyses (Percival et al. 2010; Padmanabhan et al. 2012; Mehta et al. 2012; Xu et al. 2012a). We do not include these in our data compilations because of the overlap in survey volume and redshift.

The anisotropies of the CMB are an important part of our BAO analysis. We consider three different CMB data sets. The first is the *Planck* temperature anisotropy data set, excluding lensing information from the four-point correlations in the CMB (Planck Collaboration 2013a), supplemented by *Wilkinson Microwave Anisotropy Probe* (*WMAP*) 9-year polarization data (Bennett et al. 2013) to control the optical depth to last scattering. This is the so-called Planck+WP data set in Planck Collaboration (2013b); we will abbreviate it as '*Planck*'. This is our primary CMB data set.

Our second CMB data set is the *WMAP* 9-year temperature and polarization data set (Bennett et al. 2013). We abbreviate this as '*WMAP*'. We also consider a third option, in which we combine *WMAP* 9-year data with the temperature power spectra from the finer scale and deeper data from the South Pole Telescope (SPT; Story et al. 2013) and Atacama Cosmology Telescope (ACT; Das et al. 2013). We abbreviate this as 'WMAP+SPT/ACT' or more briefly as '*eWMAP*'. The likelihood code used is the publicly available ACTLITE (Calabrese et al., 2013; Dunkley et al. 2013).

As has been widely discussed (e.g., Planck Collaboration 2013b), the cosmological fits to these CMB data sets mildly disagree. This issue can be easily characterized by comparing the fitted ranges for $\Omega_m h^2$ in the vanilla flat ΛCDM model. The values range from $\Omega_m h^2 = 0.1427 \pm 0.0024$ for *Planck* (Planck Collaboration 2013b), to 0.1371 ± 0.0044 for *WMAP*, and then to 0.1353 ± 0.0035 for WMAP+SPT/ACT. Note these numbers shift slightly from others in the literature because, following the Planck Collaboration, we include a total of 0.06 eV in neutrino masses in all our chains. The 5 per cent shift in $\Omega_m h^2$ is 2σ between the central values of *Planck* and WMAP+SPT/ACT and hence can produce noticeable variations in parameters when combining our BAO results with those from the CMB.

We include cosmological distance measurements from Type Ia supernovae by using the 'Union 2' compilation by the Supernova Cosmology Project from Suzuki et al. (2012). Supernova data are an important complement to our BAO data because they offer a precise measurement of the relative distance scale at low redshifts. We refer to this data set as 'SN'. However, we note that the recent recalibration of the SDSS-II and Supernova Legacy Survey photometric zero-points (Betoule et al. 2013) will imply a minor adjustment, not yet available, to the SNe distance constraints.

We use COSMOMC (Lewis & Bridle 2002) MCMC sampler to map the posterior distributions of these parameters. In most cases, we opt to compute chains using the CMASS DR9 data and then reweight those chains by the ratio of the DR10 or DR11 BAO likelihood to the CMASS DR9 likelihood. For each choice of cosmological model, CMB data set, and inclusion of SNe, we ran a new chain. Using these chains, the variations over choices of the BAO results could be produced quickly. This approach is feasible because the new BAO distance measurements are well contained within the allowed regions of the DR9 CMASS measurements.

We explore a variety of cosmological models, starting from the minimal ΛCDM model. We considered dark energy models of constant w and varying $w = w_0 + (1 - a)w_a$, which we notate as 'wCDM' and '$w_0 w_a$CDM', respectively. In each case, we consider variations in spatial curvature, labelled as 'oCDM', 'owCDM', and 'o$w_0 w_a$CDM'. Following Planck Collaboration (2013b), we assume a minimal-mass normal hierarchy approximated as a single massive eigenstate with $m_\nu = 0.06$ eV. This is consistent with recent oscillation data (Forero, Tórtola & Valle 2012). We note this since even in this minimal neutrino mass case, the contribution to the expansion history is becoming noticeable in cosmological analyses.

9.2 Comparison of BAO and CMB distance scales in ΛCDM

Results from the BAO method have improved substantially in the last decade, and we have now achieved measurements at a wide range of redshifts. In Fig. 21, we plot the distance–redshift relation obtained from isotropic acoustic scale fits in the latest galaxy surveys. In addition to the values from this paper, we include the acoustic-scale measurement from the 6dFGS (Beutler et al. 2011) and WiggleZ survey (Blake et al. 2011; Kazin et al. 2014). As the BAO method actually measures D_V/r_d, we plot this quantity multiplied by $r_{d,\,fid}$. The very narrow grey band here is the prediction from the *Planck* CMB data set detailed in Section 9.1. In vanilla flat ΛCDM, the CMB acoustic peaks imply precise measurements of $\Omega_m h^2$ and $\Omega_b h^2$, which in turn imply the acoustic scale. The angular acoustic scale in the CMB then determines the distance to $z = 1089$, which breaks the degeneracy between Ω_m and h once the low-redshift expansion history is otherwise specified (e.g., given Ω_K, w, and w_a). The comparison between low-redshift BAO measurements and the predictions from the CMB assuming a flat ΛCDM cosmology therefore allows per cent-level checks on the expansion history in this model over a large lever arm in redshift. One sees remarkably good agreement between the BAO measurements and the flat ΛCDM predictions from CMB observations.

Fig. 22 divides by the best-fitting prediction from Planck Collaboration (2013b) to allow one to focus on a per cent-level comparison. In addition to the BAO data from the previous figure, we also plot older BAO measurements based primarily on SDSS-II LRG data (Percival et al. 2010; Padmanabhan et al. 2012). This figure also shows the flat ΛCDM prediction from the WMAP+SPT/ACT data

Downloaded from http://mnras.oxfordjournals.org/ at University of California, Irvine on March 16, 2016

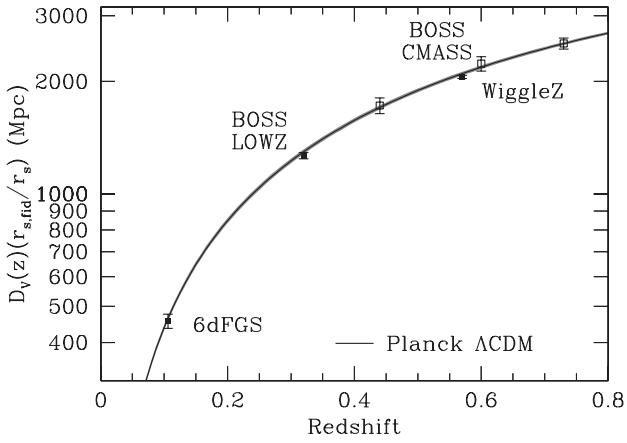

Figure 21. The distance–redshift relation from the BAO method on galaxy surveys. This plot shows $D_V(z)(r_{s,fid}/r_d)$ versus z from the DR11 CMASS and LOWZ consensus values from this paper, along with those from the acoustic peak detection from the 6dFGS (Beutler et al. 2011) and WiggleZ survey (Blake et al. 2011; Kazin et al. 2014). The grey region shows the 1σ prediction for $D_V(z)$ from the *Planck* 2013 results, assuming flat ΛCDM and using the *Planck* data without lensing combined with smaller scale CMB observations and *WMAP* polarization (Planck Collaboration 2013b). One can see the superb agreement in these cosmological measurements.

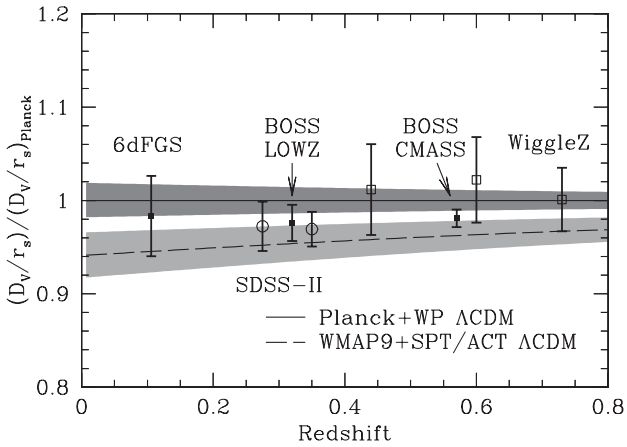

Figure 22. The $D_V(z)/r_d$ measured from galaxy surveys, divided by the best-fitting flat ΛCDM prediction from the *Planck* data. All error bars are 1σ. The *Planck* prediction is a horizontal line at unity, by construction. The dashed line shows the best-fitting flat ΛCDM prediction from the WMAP+SPT/ACT results, including their smaller scale CMB compilation (Bennett et al. 2013). In both cases, the grey region shows the 1σ variation in the predictions for $D_V(z)$ (at a particular redshift, as opposed to the whole redshift range), which are dominated by uncertainties in $\Omega_m h^2$. As the value of $\Omega_m h^2$ varies, the prediction will move coherently up or down, with amplitude indicated by the grey region. One can see the mild tension between the two sets of CMB results, as discussed in Planck Collaboration (2013b). The current galaxy BAO data fall in between the two predictions and are clearly consistent with both. As we describe in Section 7.5, the anisotropic CMASS fit would yield a prediction for this plot that is 0.5 per cent higher than the isotropic CMASS fit; this value would fall somewhat closer to the *Planck* prediction. In addition to the BOSS data points, we plot SDSS-II results as open circles, that from Percival et al. (2010) at $z = 0.275$ and from Padmanabhan et al. (2012) at $z = 0.35$. These data sets have a high level of overlap with BOSS LOWZ and with each other, so one should not include more than one in statistical fitting. However, the results are highly consistent despite variations in the exact data sets and differences in methodology. We also plot results from WiggleZ from Kazin et al. (2014) as open squares; however, we note that the distance measurements from these three redshift bins are substantially correlated.

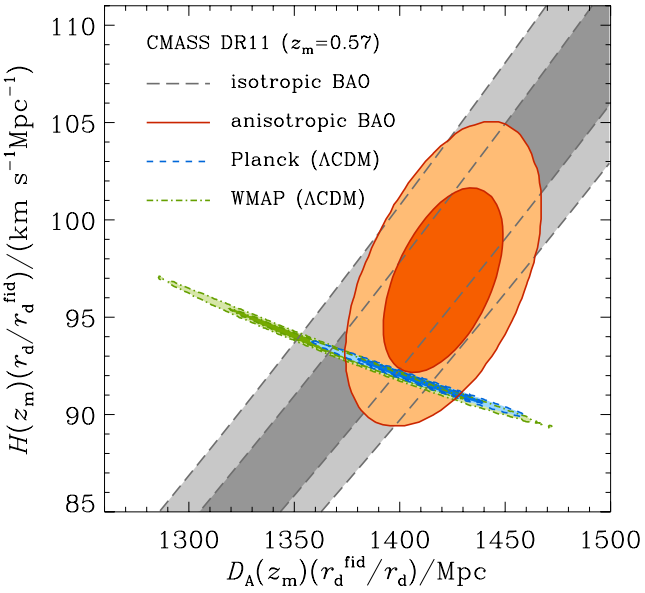

Figure 23. Comparison of the 68 and 95 per cent constraints in the $D_A(0.57)(r_d^{fid}/r_d) - H(0.57)(r_d^{fid}/r_d)$ plane from CMASS consensus anisotropic (orange) and isotropic (grey) BAO constraints. The *Planck* contours correspond to Planck+WMAP polarization (WP) and no lensing. The green contours show the constraints from *WMAP*9.

set. The predictions from these two data sets are in mild conflict due to the ∼5 per cent difference in their $\Omega_m h^2$ values, discussed in Section 9.1. One can see that the isotropic BAO data, and the BOSS measurements in particular, fall between the two predictions and are consistent with both. Note that the recent revision of *Planck* data by Spergel, Flauger & Hlozek (2013) results in a value of $\Omega_m h^2$ that is in excellent agreement with our isotropic BAO measurements, which brings *Planck* predictions of the distance scale at $z = 0.32$ and $z = 0.57$ much closer to BOSS measurements.

Our 68 and 95 per cent constraints in the $D_A(0.57)(r_d^{fid}/r_d)$–$H(0.57)(r_d/r_d^{fid})$ plane from CMASS consensus anisotropic measurements are highlighted in orange in Fig. 23. In grey we overplot one-dimensional 1- and 2σ contours of our consensus isotropic BAO fit. Also shown in Fig. 23 are the flat ΛCDM predictions from the Planck and *WMAP* CMB data sets detailed in Section 9.1. The CMB constraints occupy a narrow ellipse defined by the extremely precise measurement of the angular acoustic scale of 0.06 per cent (Planck Collaboration 2013b). The extent of the ellipse arises primarily from the remaining uncertainty on the physical CDM density, $\Omega_c h^2$; Planck narrows the allowed range by nearly a factor of 2 compared with *WMAP*. The CMASS isotropic BAO constraints are consistent with both CMB predictions shown here. The anisotropic constraints in particular prefer larger values of $\Omega_c h^2$ (right edge of the *WMAP* contour) also favoured by *Planck*. Also evident in this plot is the offset between the best-fitting anisotropic constraint on $H(0.57)(r_d/r_d^{fid})$ (or ϵ) and the flat ΛCDM predictions from the CMB.

To make the flat ΛCDM comparison between the CMB and our BAO measurements more quantitative, we report in Table 13 the Planck, *WMAP*, and *eWMAP* ΛCDM predictions for our isotropic and anisotropic BAO observables at $z = 0.32$ and 0.57. All three predictions are in good agreement with our isotropic measurements. The largest discrepancy between the *Planck* ΛCDM predictions and BOSS measurements is about $1.5\,\sigma$ for the anisotropic parameter ϵ (or the closely related $\alpha_\parallel$) at $z = 0.57$. *eWMAP* and BOSS disagree

Downloaded from http://mnras.oxfordjournals.org/ at University of California, Irvine on March 16, 2016

Table 13. Comparison of CMB flat ΛCDM predictions for the BAO distance scale to our BOSS DR11 measurements. We translate the CMB predictions to our observables of α, ϵ, $\alpha_\parallel$, and $\alpha_\perp$. As the CMB data sets vary notably in the value of $\Omega_m h^2$, we report these quantities. We also translate our BOSS distance measurements to the constraints they imply on $\Omega_m h^2$, assuming the flat ΛCDM model and using the CMB measurements of $\Omega_b h^2$ and the angular acoustic scale. We stress that this inference of $\Omega_m h^2$ is entirely model dependent and should not be used as a more general result of this paper. However, it does allow an easy comparison of the CMB and BOSS data sets in the context of ΛCDM.

Data set	$z_{\rm eff}$	α	ϵ	$\alpha_\parallel$	$\alpha_\perp$	$\Omega_m h^2$
Planck	0.32	1.040 ± 0.016	-0.0033 ± 0.0013	1.033 ± 0.014	1.043 ± 0.018	0.1427 ± 0.0024
WMAP	0.32	1.008 ± 0.029	-0.0007 ± 0.0021	1.007 ± 0.025	1.009 ± 0.031	0.1371 ± 0.0044
e*WMAP*	0.32	0.987 ± 0.023	0.0006 ± 0.0016	0.988 ± 0.020	0.986 ± 0.025	0.1353 ± 0.0035
LOWZ	0.32	1.018 ± 0.021	–	–	–	0.1387 ± 0.0036
Planck	0.57	1.031 ± 0.013	-0.0053 ± 0.0020	1.020 ± 0.009	1.037 ± 0.015	0.1427 ± 0.0024
WMAP	0.57	1.006 ± 0.023	-0.0012 ± 0.0034	1.004 ± 0.017	1.007 ± 0.027	0.1371 ± 0.0044
e*WMAP*	0.57	0.988 ± 0.019	0.0010 ± 0.0027	0.990 ± 0.013	0.987 ± 0.021	0.1353 ± 0.0035
CMASS-iso	0.57	1.0144 ± 0.0098	–	–	–	0.1389 ± 0.0022
CMASS	0.57	1.019 ± 0.010	-0.025 ± 0.014	0.968 ± 0.033	1.045 ± 0.015	0.1416 ± 0.0018

at about $1.8\,\sigma$ in ϵ, which leads to an approximately $2.2\,\sigma$ offset in $\alpha_\perp$.

Our measurements therefore provide no indication that additional parameters are needed to describe the expansion history beyond those in flat ΛCDM. However, it is also clear from Fig. 22 and Table 13 that the disagreement between the WMAP+SPT/ACT and *Planck* ΛCDM BAO predictions is comparable to the error on the BOSS acoustic-scale measurement. Under the assumption of a flat ΛCDM model, our anisotropic measurements show a mild preference for the *Planck* parameter space over WMAP+SPT/ACT. We are optimistic that the further analysis of the CMB data sets will resolve the apparent difference.

Since the uncertainties in the ΛCDM prediction of the BAO observables from the CMB are dominated by the uncertainty in $\Omega_c h^2$, another way to summarize and compare the BAO measurements across redshift is as a constraint on $\Omega_m h^2$ from the flat ΛCDM model holding the CMB acoustic scale, ℓ_A (Eq.equation 10 of Planck Collaboration 2013b), and physical baryon density, $\Omega_b h^2$ fixed. These values are given in the $\Omega_m h^2$ column of Table 13. We stress that these inferences depend critically on the assumption of a flat ΛCDM expansion history. Using this method, the BOSS inferences are more precise than the CMB and fall between the *WMAP* and *Planck* constraints. The isotropic CMASS analysis yields $\Omega_m h^2 = 0.1389 \pm 0.0022$, in close agreement with the LOWZ result of 0.1387 ± 0.0036. Our anisotropic analysis shifts to a notably larger value, $\Omega_m h^2 = 0.1416 \pm 0.0018$, closer to the Planck measurement. This shift in $\Omega_m h^2$ between the isotropic and anisotropic CMASS fits is simply a restatement of the half sigma shift in α between our isotropic and anisotropic fits, discussed in Section 7.5.

For our cosmological parameter estimation, we present *Planck* in most cases but show the results for *WMAP* and WMAP+SPT/ACT in some cases so that the reader can assess the differences. For most combinations, the agreement is good. This is because the BAO data fall between the two CMB results and hence tend to pull towards reconciliation, and because the low-redshift data sets dominate the measurements of dark energy in cosmologies more complicated than the vanilla flat ΛCDM model.

Fig. 23 and Table 13 illustrate many of the features of the ΛCDM model fits we present in Table 14. For instance, the addition of a CMASS BAO measurement to the CMB improves the constraint on $\Omega_m h^2$ by 40 per cent for *Planck* (with similar improvements for the other CMB choices). The central values for all three reported ΛCDM parameters shift by 1σ between isotropic and anisotropic CMASS fits. There are also one sigma shifts between *Planck* and *WMAP*/*eWMAP* central parameter values at fixed BAO measurements; taken together, WMAP+CMASS-iso or *e*WMAP+CMASS-iso and Planck+CMASS differ in their central values of Ω_m and H_0 by about 2σ. Additionally, combining with other BAO and SN measurements relaxes this tension to about 1σ. Within the context of the ΛCDM model, the combination of CMB and BAO provides 1 per cent (3 per cent) constraints on H_0 and Ω_m, respectively. These constraints relax by a factor of 3 (2) in the most general expansion history model, o$w_0 w_a$CDM.

In Anderson et al. (2012), we showed that the BAO distance–redshift relation is consistent with that measured by Type Ia supernovae. This remains true with these DR11 results.

9.3 Cosmological parameter estimates in extended models

While the flat ΛCDM expansion history is sufficient to explain current CMB and BAO measurements, the addition of precise low-redshift BAO distances greatly improves constraints on parameters that generalize the flat ΛCDM expansion history. In this section, we allow for non-zero spatial curvature (Ω_K), a fixed equation of state for dark energy (w), and a time-varying dark energy equation of state (w_0 and w_a).

Fig. 24 illustrates the utility of BAO measurements for constraining these additional parameters. As one changes the model of the spatial curvature or dark energy equation of state, the Ω_m and H_0 values required to simultaneously match the CMB measurement of $\Omega_m h^2$ and the distance to $z = 1089$ change. Here, we show the result assuming $w = -0.7$ for a flat cosmology, as well as that for a closed Universe with $\Omega_K = -0.01$ and a cosmological constant. One can see that these predictions are sharply different from flat ΛCDM at low redshift.

In Fig. 25, we focus instead on the two effective redshifts of our BAO observables, now examining how variations in the new parameters alter predictions for both D_A and H. For ease of comparison, we plot $\Delta\chi^2 = 2.3$, 6.1 contours for both the isotropic (dashed) and anistropic (solid) fits; these values correspond to 68 and 95 per cent confidence regions when fitting two parameters. The extremely narrow black ellipse (nearly parallel with the green curve) shows the predictions from *Planck* in a flat ΛCDM model; the uncertainty in the *Planck* predictions are dominated by the uncertainty in CDM density, $\Omega_c h^2$. The three coloured curves cross at the *Planck* best-fitting cosmology, and show how the predictions for the BAO observables depend on each of the extra parameters. To

Downloaded from http://mnras.oxfordjournals.org/ at University of California, Irvine on March 16, 2016

Table 14. Constraints by different CMB+BAO data sets in the cosmological parameters $\Omega_m h^2$, Ω_m, and H_0 in the ΛCDM model, oCDM model where we also show constraints in Ω_K and wCDM model where we also show constraints in w_0. Here, we compare the constraining power of different BAO measurements at different redshifts (e.g. LOWZ versus CMASS) as well as different analyses (isotropic versus anisotropic). We refer to 'CMASS-DR9' as the isotropic measurement presented in Anderson et al. (2012), 'CMASS-iso' as the isotropic measurement from the CMASS sample in this work, and the anisotropic one as simply 'CMASS'. 'LOWZ' is the isotropic measurement of the LOWZ sample also shown here. Given the volume sampled by the CMASS sample, and the constraining power of the anisotropic analysis, we get the best cosmological constraints in this case, especially when combined with Planck.

Cosmological model	Data sets	$\Omega_m h^2$	Ω_m	H_0 (km s^{-1} Mpc^{-1})	Ω_K	w_0
ΛCDM	*Planck*	0.1427 (24)	0.316 (16)	67.3 (11)	–	–
ΛCDM	*WMAP*	0.1371 (44)	0.284 (25)	69.6 (21)	–	–
ΛCDM	*eWMAP*	0.1353 (35)	0.267 (19)	71.3 (17)	–	–
ΛCDM	Planck + CMASS-DR9	0.1428 (20)	0.317 (13)	67.1 (9)	–	–
ΛCDM	Planck + CMASS-iso	0.1408 (15)	0.304 (9)	68.1 (7)	–	–
ΛCDM	Planck + CMASS	0.1418 (15)	0.311 (9)	67.6 (6)	–	–
ΛCDM	Planck + LOWZ	0.1416 (20)	0.309 (13)	67.7 (9)	–	–
ΛCDM	WMAP + CMASS-DR9	0.1403 (30)	0.305 (16)	67.9 (12)	–	–
ΛCDM	WMAP + CMASS-iso	0.1383 (25)	0.292 (10)	68.8 (8)	–	–
ΛCDM	WMAP + CMASS	0.1400 (24)	0.302 (10)	68.0 (8)	–	–
ΛCDM	WMAP + LOWZ	0.1379 (30)	0.289 (15)	69.2 (13)	–	–
ΛCDM	*e*WMAP + CMASS-DR9	0.1401 (25)	0.295 (14)	69.0 (11)	–	–
ΛCDM	*e*WMAP + CMASS-iso	0.1393 (18)	0.290 (9)	69.3 (7)	–	–
ΛCDM	*e*WMAP + CMASS	0.1409 (17)	0.300 (9)	68.6 (7)	–	–
ΛCDM	*e*WMAP + LOWZ	0.1409 (24)	0.282 (13)	69.9 (11)	–	–
oCDM	Planck + CMASS-DR9	0.1418 (25)	0.323 (15)	66.3 (14)	−0.0029 (42)	–
oCDM	Planck + CMASS-iso	0.1418 (25)	0.303 (9)	68.4 (8)	+0.0016 (30)	–
oCDM	Planck + CMASS	0.1420 (24)	0.311 (9)	67.5 (8)	+0.0000 (30)	–
oCDM	Planck + LOWZ	0.1418 (25)	0.307 (14)	68.0 (15)	+0.0007 (42)	–
oCDM	WMAP + CMASS-DR9	0.1372 (41)	0.306 (15)	67.0 (14)	−0.0050 (48)	–
oCDM	WMAP + CMASS-iso	0.1370 (41)	0.290 (11)	68.7 (10)	−0.0017 (41)	–
oCDM	WMAP + CMASS	0.1378 (41)	0.300 (10)	67.8 (9)	−0.0027 (41)	–
oCDM	WMAP + LOWZ	0.1371 (41)	0.291 (15)	68.7 (16)	−0.0017 (50)	–
oCDM	*e*WMAP + CMASS-DR9	0.1356 (35)	0.302 (15)	67.1 (14)	−0.0079 (44)	–
oCDM	*e*WMAP + CMASS-iso	0.1357 (36)	0.288 (10)	68.6 (9)	−0.0045 (37)	–
oCDM	*e*WMAP + CMASS	0.1360 (36)	0.296 (9)	67.7 (8)	−0.0061 (38)	–
oCDM	*e*WMAP + LOWZ	0.1357 (35)	0.288 (15)	68.6 (16)	−0.0046 (47)	–
wCDM	Planck + CMASS-DR9	0.1439 (23)	0.284 (48)	72.1 (71)	–	−1.19 (26)
wCDM	Planck + CMASS-iso	0.1439 (23)	0.251 (36)	76.4 (66)	–	−1.33 (24)
wCDM	Planck + CMASS	0.1425 (22)	0.305 (20)	68.5 (25)	–	−1.04 (11)
wCDM	Planck + LOWZ	0.1432 (24)	0.279 (26)	72.0 (36)	–	−1.17 (14)
wCDM	WMAP + CMASS-DR9	0.1378 (50)	0.324 (47)	65.9 (65)	–	−0.91 (27)
wCDM	WMAP + CMASS-iso	0.1380 (47)	0.288 (37)	69.9 (61)	–	−1.04 (26)
wCDM	WMAP + CMASS	0.1354 (43)	0.323 (18)	64.8 (25)	–	−0.84 (12)
wCDM	WMAP + LOWZ	0.1373 (47)	0.292 (25)	68.8 (36)	–	−0.99 (16)
wCDM	*e*WMAP + CMASS-DR9	0.1366 (35)	0.341 (34)	63.5 (36)	–	−0.79 (13)
wCDM	*e*WMAP + CMASS-iso	0.1360 (35)	0.311 (22)	66.2 (30)	–	−0.87 (12)
wCDM	*e*WMAP + CMASS	0.1354 (33)	0.330 (16)	64.1 (20)	–	−0.80 (8)
wCDM	*e*WMAP + LOWZ	0.1358 (35)	0.299 (23)	67.5 (29)	–	−0.90 (10)

produce these curves, we held $\Omega_c h^2$, $\Omega_b h^2$, and the CMB acoustic scale fixed; the reader should keep in mind that marginalizing over $\Omega_c h^2$ (the width of the *Planck* flat ΛCDM prediction) will allow a larger range of parameter values to be consistent with both the CMB and BAO observables compared with the fixed $\Omega_c h^2$ case.

Fig. 25 already anticipates many of the results from detailed joint parameter fitting reported in Tables 14 and 15. For instance, by comparing the model variations to the isotropic BAO measurement uncertainties, the constraint on Ω_K should be about 30 per cent better from the $z = 0.57$ isotropic BAO feature than the $z = 0.32$ measurement. For the case combining CMASS isotropic and *Planck* constraints, the uncertainty on $\Omega_c h^2$ (e.g., the extent of the flat ΛCDM *Planck* contour) degrades the constraint on Ω_K from $\sim$0.002 to 0.003. For the wCDM model, the situation is reversed: the lower redshift isotropic BAO measurement is more constraining even though the fractional measurement errors are larger. The wCDM model curves also help explain why the Planck + CMASS-iso constraint, $w = -1.34 \pm 0.25$, does not improve the error on w over our DR9 result, $w = -0.87 \pm 0.25$ (Anderson et al. 2012), even though our error on the BAO scale has improved from 1.7 to 1 per cent: models with $w < -1$, favoured by our CMASS isotropic BAO measurement, produce smaller changes in the BAO observables at $z = 0.57$ per unit change in w than models close to $w = -0.7$. Moreover, the best-fitting parameters for both the CMB and BAO data sets have

Downloaded from http://mnras.oxfordjournals.org/ at University of California, Irvine on March 16, 2016

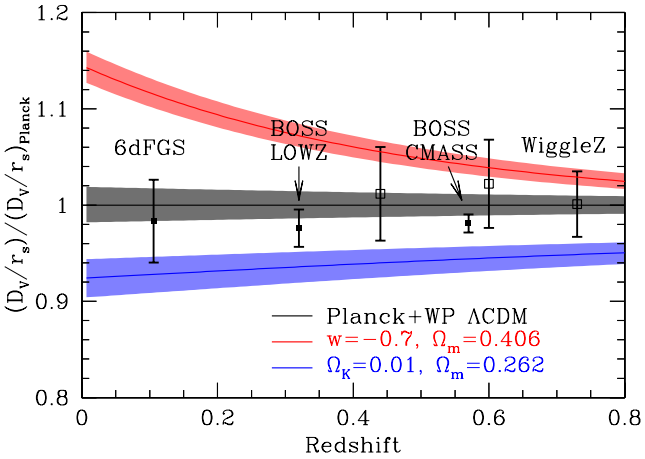

Figure 24. The $D_V(z)/r_d$ measured from galaxy surveys, divided by the best-fitting flat ΛCDM prediction from the *Planck* data. All error bars are 1σ. We now vary the cosmological model for the *Planck* prediction. Red shows the prediction assuming a flat Universe with $w = -0.7$; blue shows the prediction assuming a closed Universe with $\Omega_K = -0.01$ and a cosmological constant.

shifted between DR9 and DR11. In fact, combining CMASS-DR9 with *Planck* instead of *WMAP*7 yields $w = -1.18 \pm 0.25$. In that case, the BAO and CMB flat ΛCDM constraints have closer best fit α values.

The left-hand panel of Fig. 25 also demonstrates why the CMASS anisotropic constraints are more constraining than the isotropic ones, particularly for dark energy parameters. Variation in w at fixed CMB acoustic scale primarily shifts $D_A(0.57)$, and the anisotropic measurements provide tighter constraints in that direction. Note that none of these extra parameters drive the expansion rate as high as our anisotropic best fit to $H(0.57)$.

In order to explore our results on the full multidimensional parameter space in which we derive our cosmological constraints, we now describe the results of our MCMC chains. Here, we use our BAO measurements in combination with CMB results, and supplemented at times by SN data and other BAO measurements, doing the analysis in the context of different cosmological models. We first start by comparing constraints on the parameters $\Omega_m h^2$, Ω_m, and H_0 from our different BAO data sets in Table 14. In this case, we combine BAO with different CMB data sets: *Planck*, *WMAP*9, or *eWMAP*, in the ΛCDM, oCDM, or wCDM cosmological models. We find that all CMB+BAO combinations return similar cosmological fits in ΛCDM and oCDM models, with H_0 around 68 km s^{-1} Mpc^{-1}, Ω_m around 0.30, and negligible spatial curvature. Somewhat more variation is seen in the wCDM case, because of a degeneracy between w and H_0 that is described later in this section. However, these variations are accompanied by larger formal errors and are highly consistent with the ΛCDM fit. In our best constrained case (Planck+CMASS in ΛCDM), we find a 1 per cent measurement of $\Omega_m h^2$, a 1 per cent measurement of H_0, and a 3 per cent measurement of Ω_m. These broaden only slightly in oCDM, to 2 per cent in $\Omega_m h^2$. We find a tight measurement of curvature, consistent with a flat Universe with 0.003 error.

The degeneracy between Ω_m and H_0 is shown in Fig. 26. Here, we compare the allowed parameter space in the case of *Planck* and *WMAP*9, for the minimal ΛCDM model (left-hand panel) and the ow_0w_aCDM model (Chevallier & Polarski 2001; Linder 2003, right-hand panel). The latter was recommended by the Dark Energy Task Force (hereafter DETF; Albrecht et al. 2006) for dark energy Figure-of-Merit comparisons. This model contains three more degrees of freedom (curvature and a time-dependent equation of state for dark energy). As was discussed in Mehta et al. (2012) and Anderson et al. (2012), the combination of CMB, BAO, and SNe data results produces a reverse distance ladder that results in tight constraints on H_0 and Ω_m despite this flexibility in the cosmological model. The CMB determines the acoustic scale, which the BAO uses to measure the distance to intermediate redshift. The SNe then transfer that distance standard to low redshift, which implies H_0. Combining this with the CMB measurement of $\Omega_m h^2$ yields Ω_m.

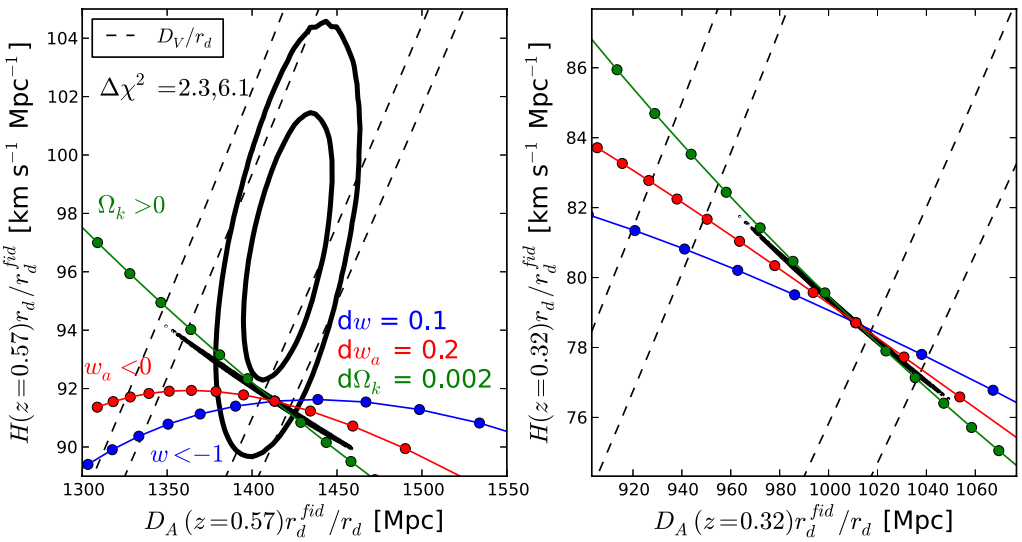

Figure 25. $\Delta\chi^2 = 2.3$, 6.1 contours for both the isotropic (dashed) and anistropic (solid) fits for the BAO observables at $z = 0.57$ (left-hand panel) and $z = 0.32$ (right-hand panel). Overplotted are the *Planck* flat ΛCDM predictions (narrow black band), where the uncertainty is dominated by the uncertainty on $\Omega_c h^2$. We overlay predictions for the BAO observables for three one-parameter extensions (Ω_K, w, or w_a) at fixed $\Omega_{c,b}h^2$ and CMB acoustic scale. Given our relative errors on D_A and H at $z = 0.57$, we can see that for the models of interest, the improved constraint on D_A is driving the improvement of our results from the isotropic to anisotropic analysis. Also note that none of these models move along the long-axis of our anisotropic constraints towards our best-fitting values.

Downloaded from http://mnras.oxfordjournals.org/ at University of California, Irvine on March 16, 2016

Table 15. Cosmological constraints by different data sets in the cosmological models ΛCDM, oCDM, wCDM, owCDM, w_0w_aCDM, and ow_0w_aCDM. We compare the cosmological constraints from combining *Planck* with acoustic scale from BOSS galaxies as well as lower and higher redshift BAO measurements from the 6-degree field galaxy redshift survey (6DF) and the BOSS-Lyman α forest (LyαF), respectively. We also compare how these combinations benefit from the constraining power of Type Ia Supernovae from the Union 2 compilation by the Supernovae Cosmology Project (SN). The *WMAP* and *eWMAP* cases have been added for comparison. As in Table 14, 'CMASS-iso' means the isotropic measurement from the CMASS sample, whereas the anisotropic one is referred to simply as 'CMASS'. 'LOWZ' is the isotropic measurement from the LOWZ sample. 'BAO' stands for the combination CMASS + LOWZ + 6DF + LyαF.

Cosmological model	Data sets	$\Omega_m h^2$	Ω_m	H_0 (km s^{-1} Mpc^{-1})	Ω_K	w_0	w_a
ΛCDM	Planck + CMASS-iso + LOWZ	0.1405 (14)	0.302 (8)	68.2 (6)	–	–	–
ΛCDM	Planck + CMASS + LOWZ	0.1415 (14)	0.308 (8)	67.8 (6)	–	–	–
ΛCDM	Planck + BAO	0.1417 (13)	0.310 (8)	67.6 (6)	–	–	–
ΛCDM	Planck + CMASS + LOWZ + SN	0.1414 (13)	0.308 (8)	67.8 (6)	–	–	–
ΛCDM	Planck + BAO + SN	0.1416 (13)	0.309 (8)	67.7 (6)	–	–	–
ΛCDM	WMAP + BAO + SN	0.1399 (22)	0.302 (8)	68.1 (7)	–	–	–
ΛCDM	*e*WMAP + BAO + SN	0.1411 (16)	0.301 (8)	68.5 (6)	–	–	–
oCDM	Planck + CMASS-iso + LOWZ	0.1417 (25)	0.302 (8)	68.5 (8)	+0.0017 (30)	–	–
oCDM	Planck + CMASS + LOWZ	0.1420 (25)	0.309 (8)	67.8 (7)	+0.0006 (30)	–	–
oCDM	Planck + BAO	0.1423 (25)	0.311 (8)	67.7 (7)	+0.0007 (29)	–	–
oCDM	Planck + CMASS + LOWZ + SN	0.1416 (24)	0.308 (8)	67.9 (7)	+0.0003 (30)	–	–
oCDM	Planck + BAO + SN	0.1419 (24)	0.309 (8)	67.7 (7)	+0.0004 (29)	–	–
oCDM	WMAP + BAO + SN	0.1384 (40)	0.300 (9)	67.9 (8)	−0.0019 (40)	–	–
oCDM	*e*WMAP + BAO + SN	0.1364 (34)	0.296 (8)	67.9 (7)	−0.0054 (35)	–	–
wCDM	Planck + CMASS-iso + LOWZ	0.1431 (22)	0.274 (21)	72.5 (32)	–	−1.19 (13)	–
wCDM	Planck + CMASS + LOWZ	0.1425 (21)	0.299 (16)	69.1 (21)	–	−1.07 (9)	–
wCDM	Planck + BAO	0.1419 (21)	0.308 (14)	67.9 (18)	–	−1.01 (8)	–
wCDM	Planck + CMASS + LOWZ + SN	0.1426 (19)	0.299 (12)	69.1 (16)	–	−1.07 (7)	–
wCDM	Planck + BAO + SN	0.1423 (19)	0.305 (12)	68.4 (14)	–	−1.04 (6)	–
wCDM	WMAP + BAO + SN	0.1380 (33)	0.307 (12)	67.0 (16)	–	−0.94 (8)	–
wCDM	*e*WMAP + BAO + SN	0.1379 (28)	0.312 (11)	66.5 (15)	–	−0.90 (7)	–
owCDM	Planck + CMASS-iso + LOWZ	0.1418 (25)	0.261 (31)	74.1 (46)	−0.0022 (36)	−1.27 (21)	–
owCDM	Planck + CMASS + LOWZ	0.1420 (24)	0.298 (23)	69.2 (27)	−0.0005 (44)	−1.08 (14)	–
owCDM	Planck + BAO	0.1422 (24)	0.315 (19)	67.3 (20)	+0.0018 (44)	−0.98 (11)	–
owCDM	Planck + CMASS + LOWZ + SN	0.1421 (25)	0.298 (14)	69.1 (16)	−0.0008 (34)	−1.07 (8)	–
owCDM	Planck + BAO + SN	0.1422 (25)	0.306 (13)	68.2 (15)	+0.0002 (34)	−1.03 (7)	–
owCDM	WMAP + BAO + SN	0.1374 (42)	0.306 (13)	67.1 (16)	−0.0010 (44)	−0.95 (8)	–
owCDM	*e*WMAP + BAO + SN	0.1357 (35)	0.305 (13)	66.7 (15)	−0.0039 (40)	−0.93 (8)	–
w_0w_aCDM	Planck + CMASS-iso + LOWZ	0.1434 (22)	0.302 (53)	69.8 (66)	–	−0.90 (51)	−0.78 (124)
w_0w_aCDM	Planck + CMASS + LOWZ	0.1431 (21)	0.350 (41)	64.3 (41)	–	−0.54 (39)	−1.41 (101)
w_0w_aCDM	Planck + BAO	0.1428 (21)	0.361 (32)	63.1 (29)	–	−0.43 (30)	−1.62 (84)
w_0w_aCDM	Planck + CMASS + LOWZ + SN	0.1433 (22)	0.304 (17)	68.7 (19)	–	−0.98 (19)	−0.36 (64)
w_0w_aCDM	Planck + BAO + SN	0.1431 (22)	0.311 (16)	67.8 (18)	–	−0.93 (18)	−0.41 (62)
w_0w_aCDM	WMAP + BAO + SN	0.1372 (43)	0.302 (16)	67.5 (17)	–	−1.00 (16)	0.16 (59)
w_0w_aCDM	*e*WMAP + BAO + SN	0.1366 (31)	0.300 (15)	67.5 (17)	–	−1.04 (14)	0.41 (40)
ow_0w_aCDM	Planck + CMASS-iso + LOWZ	0.1419 (25)	0.296 (50)	70.0 (62)	−0.0042 (40)	−0.83 (45)	−1.41 (115)
ow_0w_aCDM	Planck + CMASS + LOWZ	0.1417 (25)	0.347 (38)	64.2 (37)	−0.0039 (47)	−0.50 (34)	−1.79 (91)
ow_0w_aCDM	Planck + BAO	0.1420 (24)	0.361 (30)	62.9 (27)	−0.0020 (47)	−0.40 (28)	−1.82 (82)
ow_0w_aCDM	Planck + CMASS + LOWZ + SN	0.1419 (25)	0.306 (16)	68.1 (19)	−0.0042 (44)	−0.87 (20)	−0.98 (89)
ow_0w_aCDM	Planck + BAO + SN	0.1423 (25)	0.313 (16)	67.5 (17)	−0.0023 (43)	−0.87 (20)	−0.74 (83)
ow_0w_aCDM	WMAP + BAO + SN	0.1371 (44)	0.302 (16)	67.4 (18)	+0.0018 (68)	−1.00 (18)	0.22 (73)
ow_0w_aCDM	*e*WMAP + BAO + SN	0.1358 (35)	0.301 (15)	67.2 (17)	−0.0023 (55)	−0.99 (16)	0.18 (60)

As shown in the figure, changing between *Planck* and *WMAP* data does not significantly shift these constraints.

As has been discussed before (Anderson et al. 2012; Mehta et al. 2012; Planck Collaboration 2013b), the H_0 value inferred from this reverse distance ladder, 67.5 ± 1.8 km s^{-1} Mpc^{-1}, is notably lower than some recent local measurements. For example, Riess et al. (2011) find $H_0 = 73.8 \pm 2.4$ km s^{-1} Mpc^{-1} and Freedman et al. (2012) find $H_0 = 74.3 \pm 2.1$ km s^{-1} Mpc^{-1}. The Riess et al. (2011) value would be decreased by a small recalibration of the water maser distance to NGC 4258 (Humphreys et al. 2013). Efstathiou (2013) warns about possible biases in the period–luminosity relation fits due to low-metallicity Cepheids and finds a lower value of $H_0 = 70.6 \pm 3.3$ km s^{-1} Mpc^{-1} using only NGC 4258 as the primary distance standard, including the maser recalibration, or $H_0 = 72.5 \pm 2.5$ km s^{-1} Mpc^{-1} using three sets of primary standards. While we believe that the comparison of these direct measurements to our BAO results is important, the results are also affected by the ongoing photometric recalibration of the SDSS and SNLS SNe data (Betoule et al. 2013). We have therefore not pursued a more quantitative assessment at this time.

Downloaded from http://mnras.oxfordjournals.org/ at University of California, Irvine on March 16, 2016

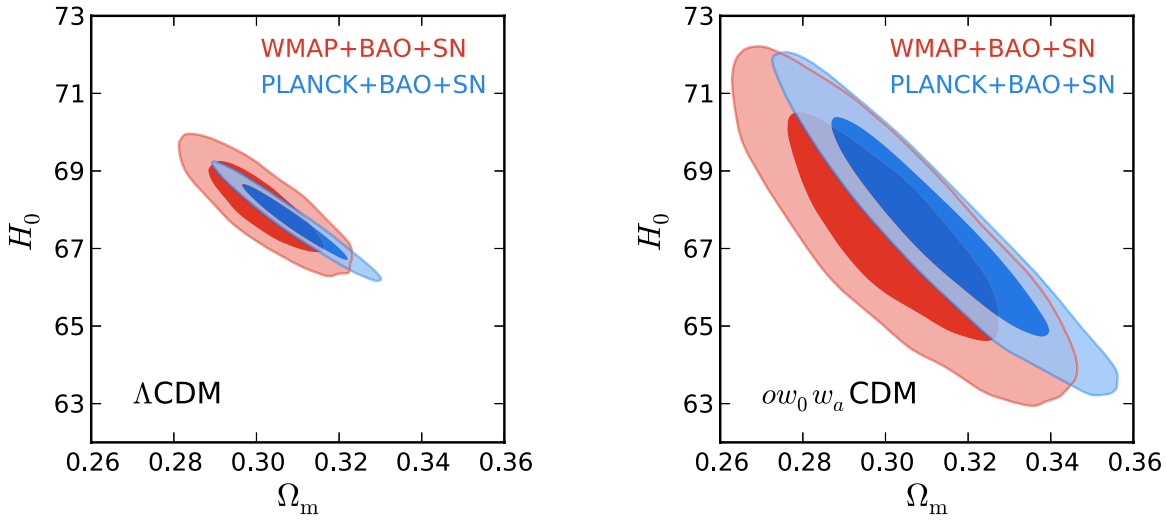

Figure 26. Constraints in the Ω_m–H_0 plane for the combination CMB+BAO+SN, in the ΛCDM (left) and ow_0w_aCDM (right) cosmological models. Here, we show the degeneracy direction in this plane and we compare the allowed regions in this parameter space when the CMB data set used is *WMAP*9 (red) or *Planck* (blue). The allowed regions open up when adding more degrees of freedom to the cosmological model; however, they still exclude values of 73 km s^{-1} Mpc^{-1} and above. The BAO and SN data sets make the H_0 values from *WMAP*9 and *Planck* agree with each other. The best-fitting value of Ω_m is slightly different between the two, but still consistent within 1σ.

We next discuss how BAO can help constrain additional degrees of freedom. In Table 15, we present our results in more general cosmological models: ΛCDM, oCDM (adding curvature), wCDM (adding an equation of state parameter for dark energy), owCDM (adding both), w_0w_aCDM (allowing for time-dependence in the e.o.s. of dark energy), and ow_0w_aCDM (our most general model, for DETF comparisons). In each case, we begin with the results of combining our CMASS and LOWZ data with Planck, showing both isotropic and anisotropic CMASS cases. We then extend the data combination with anisotropic CMASS to include additional BAO information from the 6dFGS and Lyα forest, as well as SNe results from the Union 2 compilation. Finally, for the full combination of BAO and SNe, we vary the CMB measurements between *Planck*, *WMAP*, and *eWMAP* to explore any dependence on the tensions between those data sets.

We find that these data sets can constrain the equation of state of dark energy to 6 per cent and curvature to 0.2 per cent, although the time evolution of dark energy is still unconstrained. In the DETF cosmology, we find a Figure-of-Merit value (inverse square root of the minor of the covariance matrix containing the covariances of w_0 and w_a) of 13.5. We find that the anisotropic BAO measurement from CMASS-DR11 is much more powerful when constraining the equation of state of dark energy (even when considering time-evolving dark energy) than its isotropic counterpart.

Fig. 27 shows the constraints in the H_0–w plane for different BAO data sets combined with *Planck* results. The degeneracy between both parameters is quite evident, showing that a more negative value for w can result in a higher estimation for the Hubble constant. This effect can also be seen in Fig. 24; for the wCDM model, variations in the distance to intermediate redshift produce larger variations in the local distance scale. The extent of the error contours as we vary the choice BAO data set is somewhat complicated, as was illustrated in Fig. 25. The efficacy of a given BAO distance precision to constrain w degrades as the fit shifts to more negative values of w; this is because models with $w \ll -1$ have their dark energy disappear by intermediate redshift, leaving the BAO and CMB constraints degenerate. The improvement when we change from the isotropic CMASS results to the anisotropic ones is partially due to a shift in w towards 0 and partially because of the rotation of the contours to favour a D_A constraint. Overall, this figure also shows the consistency between the various BOSS results and the tight constraints on w that the BAO now provides.

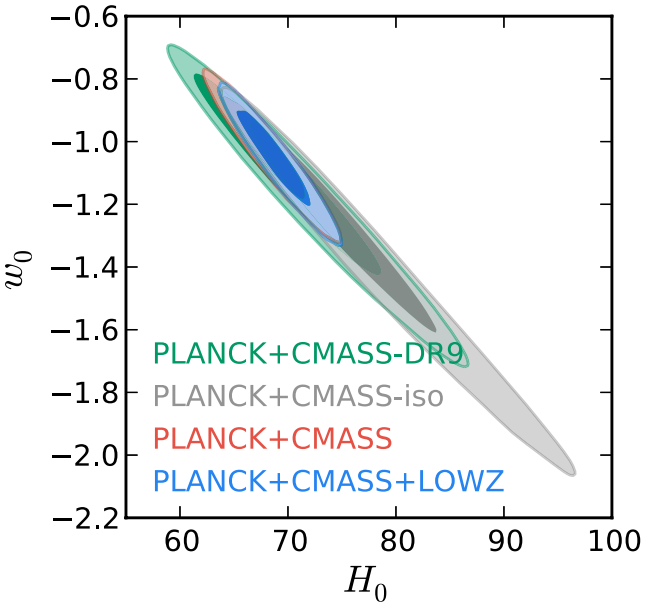

Figure 27. Constraints in the H_0–w plane for Planck+DR9, Planck+CMASS-isotropic, Planck+CMASS (anisotropic), and Planck+CMASS+LOWZ. This figure shows the degeneracy between the Hubble constant and the dark energy equation of state, assumed constant in time. Comparing with the Planck+CMASS-DR9 results (green contours), we note that the additional volume in CMASS-DR11 did not help that much (dark contours). However, performing an anisotropic BAO analysis of the same data really improves the constraints (red contours). The addition of the LOWZ isotropic BAO measurement at lower redshift (blue contours) has a marginal improvement over the CMASS anisotropic constraints, but it is a significant improvement over CMASS isotropic (see Table 14).

Downloaded from http://mnras.oxfordjournals.org/ at University of California, Irvine on March 16, 2016

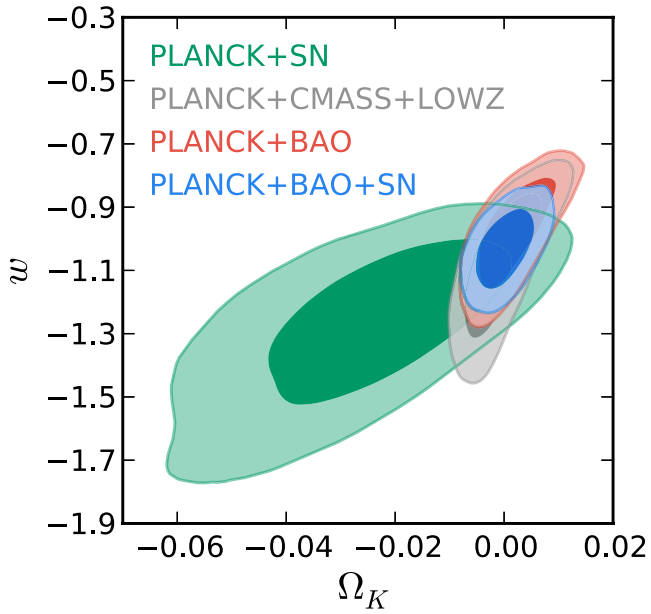

Figure 28. Constraints in the Ω_K–w plane for Planck+CMASS+LOWZ, Planck+BAO, Planck+BAO+SN, and Planck+SN. The combination of CMB and SNe (green contours) has a substantial statistical degeneracy in this parameter space; however, combining CMB and BAO strongly constrains the curvature (grey contours for the LOWZ+CMASS results presented in this paper, and red contours when adding low- and high-redshift BAO measurements). This makes the combination of CMB, BAO, and SNe (blue contours) a powerful one in this parameter space, yielding a fit centred around the ΛCDM values of $\Omega_K = 0$ and $w = -1$.

We turn next to the owCDM case, attempting to measure a constant dark energy equation of state in the presence of non-zero spatial curvature. These constraints are shown in Fig. 28 for several combinations of data sets. The allowed region in this parameter space by the combination CMB+SN is large, due to a substantial degeneracy between w and curvature. This degeneracy is lifted by the BAO, which in combination with the CMB sharply constrains the curvature. Even without the SNe data, the BAO distance constraints are now strong enough to measure w while simultaneously measuring Ω_K. With *Planck*, CMASS, and LOWZ measurements alone, we find $w = -1.08 \pm 0.15$. Further combine with the BAO measurement from 6dF and the Lyα forest BAO measurement from BOSS, we find $w = -0.98 \pm 0.11$. In both cases, the fitted cosmologies are consistent with a flat Universe. Hence, the BAO distance scale now provides enough precision, without additional data beyond the CMB, to measure w to 11 per cent even while marginalizing over spatial curvature. It is remarkable that the BAO data prefer a flat Universe with $w = -1$ despite simultaneously opening two additional degrees of freedom relative to the flat cosmological constant model. We note the BAO and SNe constraints remain highly complementary in their degeneracy directions; adding the SN data shrinks the allowed region further, to $w = -1.04 \pm 0.07$ while remaining consistent with a flat Universe.

Finally, in Fig. 29 we show our constraints on a time-dependent dark energy equation of state. The contours show the allowed parameter space using the combination of CMB and BAO data, with and without SNe data, in a flat w_0w_aCDM model (left-hand panel) and an ow_0w_aCDM model with curvature (right-hand panel). This parameter space is poorly constrained, with a clear degeneracy between the w_0 and w_a parameters, such that less negative values of w_0 are related to more negative values of w_a. The addition of SN data suppresses the likelihood of less negative w_0 values, greatly reducing the allowed parameter space. We note that allowing non-zero spatial curvature degrades the dark energy constraints, but not catastrophically. The area covered by the 2σ contour in the ow_0w_aCDM case is the DETF Figure of Merit.

10 CONCLUSION

We have presented constraints on cosmology and the distance–redshift relation from the Data Releases 10 and 11 galaxy samples of

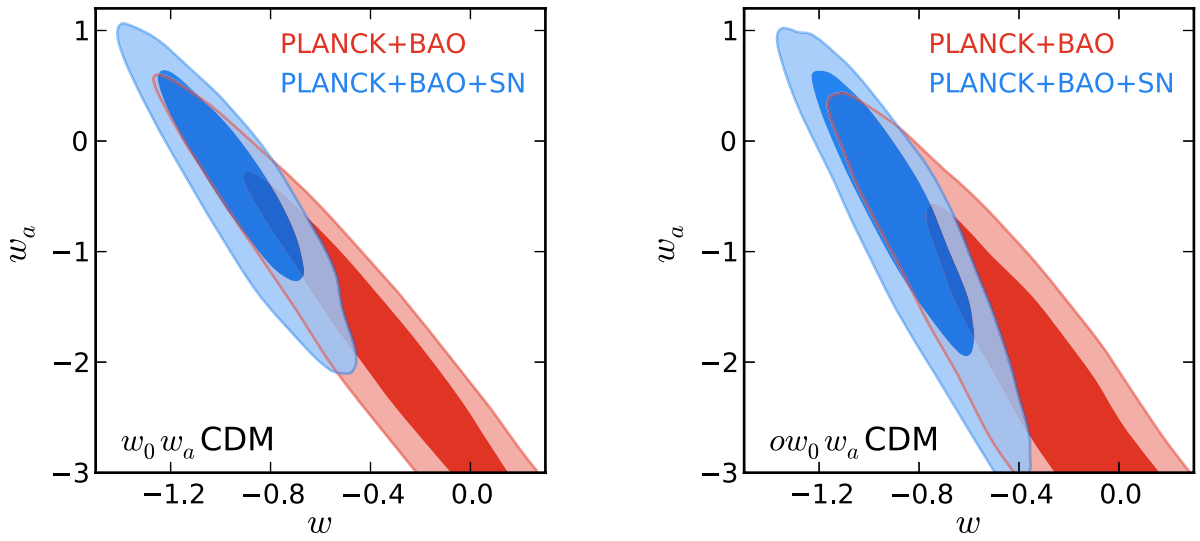

Figure 29. Constraints in the w_a–w_0 plane for Planck+BAO (red contours), and Planck+BAO+SN (blue contours), for both w_0w_aCDM (left-hand panel) and ow_0w_aCDM (right-hand panel). Note that the area of the 95 per cent contour in the right-hand panel is related to the dark energy Figure of Merit, as recommended by the DETF. The degeneracy direction in clear in both panels, but the addition of SN data helps rule out very negative values of w_a. Furthermore, the best-fitting values for these two parameters in this case are closer to those of a ΛCDM cosmology ($w_0 = -1$, $w_a = 0$) than without SN data, in which case ΛCDM falls outside of the 68 per cent ellipse.

Downloaded from http://mnras.oxfordjournals.org/ at University of California, Irvine on March 16, 2016

the Baryon Oscillation Spectroscopic sample. These results, based on the largest volume of the Universe ever surveyed at this high density (8.4 Gpc^3, including both LOWZ and CMASS samples), provide the strongest constraints on the distance–redshift relation achieved with the BAO method and the most accurate determination of the distance scale in the crucial redshift range where the expansion of the Universe begins to accelerate.

The combination of large survey volume, high sampling density and high bias of the LOWZ and CMASS galaxies allows detection of the acoustic oscillation signal at unprecedented significance. The acoustic signature is seen in both the power spectrum and the correlation function, before density-field reconstruction and after reconstruction. The measures are all highly consistent and the values and errors are in accord with our models and mock catalogues (Manera et al. 2013a, 2014). Unlike our earlier results based upon DR9, we find density-field reconstruction significantly improves our measurement of the acoustic scale (see Fig. 4), with the amount of improvement consistent with expectations if the underlying cosmology were of the ΛCDM family.

With the larger volume of data, we now have statistically significant evidence for variations in the target catalogue density that are correlated with seeing and stellar density. We correct for these systematics, along with a correction for redshift failures and galaxies for which a redshift was not obtained due to fibre collisions, using weights. A similar procedure was used in Anderson et al. (2012), except the weights have been revised to correct for the effects of seeing.

We fit the acoustic signature to an appropriately scaled template in both the correlation function and power spectrum, marginalizing over broad-band shape. Our results are insensitive to the model of broad-band power and highly consistent between configuration- and Fourier-space. As an extension of the work reported in Anderson et al. (2012), we now explicitly consider the effects of binning in the correlation function and power spectrum and combine the two methods using several different binning choices. We measure a spherically averaged distance, $D_V \equiv [cz(1+z)^2 D_\mathrm{A}/H]^{1/3}$, in units of the sound-horizon, r_d, at two 'effective' redshifts: $z = 0.32$ and $z = 0.57$. Our consensus results for the distance, including a budget for systematic errors, are $D_V(0.32) = (1264 \pm 25\,\mathrm{Mpc})\left(r_\mathrm{d}/r_{\mathrm{d,fid}}\right)$ and $D_V(0.57) = (2056 \pm 20\,\mathrm{Mpc})\left(r_\mathrm{d}/r_{\mathrm{d,fid}}\right)$. The measurement at $z = 0.57$ is the first ever 1 per cent measurement of a distance using the BAO method.

As in Anderson et al. (2014), we have used the anisotropy in the measured configuration-space clustering, induced by RSD, to separately constrain the distance along and across the line of sight. We compress the dependence on the angle to the line of sight into two statistics, either the multipole moments or 'wedges'. We obtain consistent fits from both methods. A detailed study of possible systematics in inferences from anisotropic clustering is presented in Vargas-Magana et al. (2013). Our consensus results for the CMASS sample at $z = 0.57$ are $D_\mathrm{A}(0.57) = (1421 \pm 20\,\mathrm{Mpc})\left(r_\mathrm{d}/r_{\mathrm{d,fid}}\right)$ and $H(0.57) = \left(96.8 \pm 3.4\,\mathrm{km\,s^{-1}\,Mpc^{-1}}\right)\left(r_{\mathrm{d,fid}}/r_\mathrm{d}\right)$ with a correlation coefficient between the two of 0.539.

Samushia et al. (2014), Beutler et al. (2013) and Sánchez et al. (2013b) have used the correlation function and power spectrum over a wide range of scales, along with a model for the broad-band power, to constrain cosmological parameters including the distance–redshift relation and $H(z)$. We find excellent agreement between their results and the pure-BAO measurement described here, despite differences in the procedure. This is not unexpected, in that the bulk of the information is contained in the acoustic signal rather than the broad-band power.

The BOSS results provide the tightest constraints in an reverse distance ladder that tightly constrains the expansion rate from $z \sim 0$ to 0.6. The measurements reported here are in excellent agreement with earlier BAO results by BOSS Anderson et al. (2012) and by other groups (Percival et al. 2010; Beutler et al. 2011; Blake et al. 2011; Padmanabhan et al. 2012).

The DR11 D_V distance to $z = 0.57$ is approximately 1.8 per cent smaller than that reported to the same redshift based on the DR9 data. This shift is approximately 1σ relative to the DR9 error bars. As the data set has tripled in size, such a shift is consistent with expectations. Both the $z \simeq 0.32$ and 0.57 distance measurements are highly consistent with expectations from the *Planck* and *WMAP* CMB measurements assuming a ΛCDM model, lying approximately mid-way between the inferences from the two experiments. Our results for D_A and H are similarly consistent with both CMB data sets; in detail, the anisotropic results are slightly closer to the *Planck* best-fitting ΛCDM prediction. While there are some mild tensions between the CMB data sets, the distance scale inferred from acoustic oscillations in the distant Universe ($z \simeq 10^3$) and in the local Universe ($z < 1$) are in excellent agreement with the predictions of a ΛCDM model, with gravity well described by general relativity and with a time-independent and spatially constant dark energy with equation of state $p = -\rho$.

The BOSS will finish data taking within the next year. Along with the additional data, constraints at higher z from the Lyα forest, improvements in the analysis and a full systematic error study, we expect BOSS to provide the definitive measurement of the absolute distance scale out to $z \simeq 0.7$ for some time to come.

ACKNOWLEDGEMENTS

Funding for SDSS-III has been provided by the Alfred P. Sloan Foundation, the Participating Institutions, the National Science Foundation, and the US Department of Energy Office of Science. The SDSS-III website is http://www.sdss3.org/.

SDSS-III is managed by the Astrophysical Research Consortium for the Participating Institutions of the SDSS-III Collaboration including the University of Arizona, the Brazilian Participation Group, Brookhaven National Laboratory, University of Cambridge, Carnegie Mellon University, University of Florida, the French Participation Group, the German Participation Group, Harvard University, the Instituto de Astrofisica de Canarias, the Michigan State/Notre Dame/JINA Participation Group, Johns Hopkins University, Lawrence Berkeley National Laboratory, Max Planck Institute for Astrophysics, Max Planck Institute for Extraterrestrial Physics, New Mexico State University, New York University, Ohio State University, Pennsylvania State University, University of Portsmouth, Princeton University, the Spanish Participation Group, University of Tokyo, University of Utah, Vanderbilt University, University of Virginia, University of Washington, and Yale University.

We acknowledge the use of the Legacy Archive for Microwave Background Data Analysis (LAMBDA). Support for LAMBDA is provided by the NASA Office of Space Science.

This research used resources of the National Energy Research Scientific Computing Center, which is supported by the Office of Science of the US Department of Energy under Contract no. DE-AC02-05CH11231.

Some of the CMASS reconstruction and MCMC computations were supported by facilities and staff of the Yale University Faculty of Arts and Sciences High Performance Computing Center.

LOWZ reconstruction computations were supported by the facilities and staff of the UK Sciama High Performance Computing

Downloaded from http://mnras.oxfordjournals.org/ at University of California, Irvine on March 16, 2016

cluster supported by SEPNet and the University of Portsmouth. Power spectrum calculations, and fitting made use of the COSMOS/Universe supercomputer, a UK-CCC facility supported by HEFCE and STFC in cooperation with CGI/Intel.

We thank Christian Reichardt for his help in using the ACTLITE likelihood code.

REFERENCES

Abazajian K. et al., 2004, AJ, 128, 502
Abazajian K. N. et al., 2009, ApJS, 182, 543 (DR7)
Ade et al., Planck Collaboration I, 2013a, preprint (arXiv:1303.5062)
Ade et al., , 2013b, preprint (arXiv:1303.5076)
Ahn C. et al. Planck Collaboration XVI, 2014, ApJS, 211, 17
Aihara H. et al., 2011, ApJS, 193, 29
Albrecht A. et al., 2006, preprint (arXiv:astro-ph/0609591)
Alcock C., Paczynski B., 1979, Nature, 281, 358
Anderson L. et al., 2012, MNRAS, 427, 3435
Anderson L. et al., 2014, MNRAS, 439, 83
Bennett C. et al., 2013, ApJS, 208, 20
Bernardeau F., Colombi S., Gaztanaga E., Scoccimarro R., 2002, Phys. Rep., 367, 1
Betoule M. et al., 2013, A&A, 552, 124
Beutler F. et al., 2011, MNRAS, 416, 3017
Beutler F. et al., 2013, preprint (arXiv:1312.4611)
Blake C. et al., 2011, MNRAS, 415, 1707
Blanton M., Lin H., Lupton R. H., Maley F. M., Young N., Zehavi I., Loveday J., 2003, AJ, 125, 2276
Bolton A. et al., 2012, AJ, 144, 144
Busca N. G. et al., 2013, A&A, 552, 96
Calabrese E. et al., 2013, Phys. Rev. D, 87, 103012
Carnero A., Sánchez E., Crocce M., Cabré A., Gaztañaga E., 2012, MNRAS, 419, 1689
Chevallier M., Polarski D., 2001, Int. J. Mod. Phys. D, 10, 213
Chuang C.-H., Wang Y., 2011, MNRAS, 426, 226
Chuang C.-H. et al., 2013a, MNRAS, 433, 3559
Chuang C.-H. et al., 2013b, MNRAS, 435, 255
Cole S. et al., 2005, MNRAS, 362, 505
Colless M. et al., 2003, preprint (astro-ph/0306581)
Crocce M., Scoccimarro R., 2006, Phys. Rev. D, 73
Crocce M., Scoccimarro R., 2008, Phys. Rev. D, 77, 023533
Das S. et al., 2013, preprint (arXiv:1301.1037)
Dawson K. et al., 2012, AJ, 145, 10
Doi M. et al., 2010, AJ, 139, 1628
Doroshkevich A. G., Zel'dovich Ya. B., Sunyaev R. A., 1978, SvA, 22, 523
Dunkley J. et al., 2013, J. Cosmol. Astropart. Phys., 07, 025
Efstathiou G., 2013, MNRAS, preprint (arXiv:1311.3461)
Eisenstein D. J., Hu W., 1998, ApJ, 496, 605 (EH98)
Eisenstein D. J. et al., 2005, ApJ, 633, 560
Eisenstein D. J., Seo H. J., White M., 2006, ApJ, 664, 660
Eisenstein D. J., Seo H.-J., White M., 2007a, ApJ, 664, 660
Eisenstein D. J., Seo H.-J., Sirko E., Spergel D. N., 2007b, ApJ, 664, 675
Eisenstein D. J. et al., 2011, AJ, 142, 72
Feldman H. A., Kaiser N., Peacock J. A., 1994, ApJ, 426, 23
Font-Ribera A. et al., 2013, preprint (arXiv:1311.1767)
Forero D. V., Tórtola M., Valle J., 2012, Phys. Rev. D, 86, 073012
Freedman W. L., Madore B. F., Scowcroft V., Burns C., Monson A., Persson S. E., Seibert M., Rigby J., 2012, ApJ, 758, 24
Fukugita M., Ichikawa T., Gunn J. E., Doi M., Shimasaku K., Schneider D. P., 1996, AJ, 111, 1748
Gaztanaga E., Cabre A., Hui L., 2009, MNRAS, 399, 1663
Goroff M. H., Grinstein B., Rey S.-J., Wise M. B., 1986, ApJ, 311, 6
Górski K. M., Hivon E., Banday A. J., Wandelt B. D., Hansen F. K., Reinecke M., Bartelmann M., 2005, ApJ, 622, 759
Gunn J. E. et al., 1998, AJ, 116, 3040
Gunn J. E. et al., 2006, AJ, 131, 2332
Hamilton A. J. S., Tegmark M., 2000, MNRAS, 312, 285
Ho S. et al., 2012, ApJ, 761, 14
Humphreys L., Reid M. J., Moran J. M., Greenhill L. J., Argon A. L., 2013, ApJ, 775, 13
Hütsi G., 2006, A&A, 449, 891
Høg E. et al., 2000, A&A, 355, 27
Jain B., Bertschinger E., 1994, ApJ, 431, 495
Kaiser N., 1987, MNRAS, 227, 1
Kazin E., Sanchez A. G., Blanton M. R., 2012, MNRAS, 419, 3223
Kazin E. et al., 2013, MNRAS, 435, 64
Kazin E. A., Koda J., Blake C., Padmanabhan N., 2014, MNRAS, preprint (arXiv:1401.0358)
Kirkby D. et al., 2013, J. Cosmol. Astropart. Phys., 3, 24
Landy S. D., Szalay A. S., 1993, ApJ, 412, 64
Lewis A., Bridle S., 2002, Phys. Rev. D, 66, 103511
Lewis A., Challinor A., Lasenby A., 2000, ApJ, 538, 473
Linder E. V., 2003, Phys. Rev. D, 90, 091301
Lupton R., Gunn J. E., Ivezić Z., Knapp G., Kent S., 2001, in Harnden F. R., Jr, Primini F. A., Payne H. E., eds, ASP Conf. Ser. Vol. 238, Astronomical Data Analysis Software and Systems X. Astron. Soc. Pac., San Francisco, p. 269
McQuinn M., O'Leary R. M., 2012, ApJ, 760, 3
Makino N., Sasaki M., Suto Y., 1992, Phys. Rev. D, 46, 585
Manera M. et al., 2013, MNRAS, 428, 1036
Manera M. et al., 2014, preprint (arXiv:1401.4171)
Maraston C. et al., 2013, MNRAS, 435, 2764
Matsubara T., 2008, Phys. Rev. D, 77, 063530
Mehta K. T., Seo H.-J., Eckel J., Eisenstein D. J., Metchnik M., Pinto P., Xu X., 2011, ApJ, 734, 94
Mehta K., Cuesta A. J., Xu X., Eisenstein D. J., Padmanabhan N., 2012, MNRAS, 427, 2168
Meiksin A., White M., Peacock J. A., 1999, MNRAS, 304, 851
Mortonson M. J., Weinberg D. H., White M., 2014, Particle Data Group 2014 Review of Particle Physics, Chapter 25, preprint (arXiv:1401.0046)
Noh Y., White M., Padmanabhan N., 2009, Phys. Rev. D, 80, 123501
Nuza S. E. et al., 2013, MNRAS, 432, 743
Okumura T., Matsubara T., Eisenstein D. J., Kayo I., Hikage C., Szalay A. S., Schneider D. P., 2008, ApJ, 676, 889
Padmanabhan N., White M., 2009, Phys. Rev. D, 80, 063508
Padmanabhan N. et al., 2007, MNRAS, 378, 852
Padmanabhan N. et al., 2008, ApJ, 674, 1217
Padmanabhan N., Xu X., Eisenstein D. J., Scalzo R., Cuesta A. J., Mehta K. T., Kazin E., 2012, MNRAS, 427, 2132
Parejko J. K. et al., 2013, MNRAS, 429, 98
Peacock J. A., Dodds S. J., 1994, MNRAS, 267, 1020
Peebles P. J. E., Yu J. T., 1970, ApJ, 162, 815
Percival W. J., Cole S., Eisenstein D. J., Nichol R. C., Peacock J. A., Pope A. C., Szalay A. S., 2007, MNRAS, 381, 1053
Percival W. J. et al., 2010, MNRAS, 401, 2148
Percival W. J. et al., 2014, MNRAS, 439, 2531
Perlmutter S. et al., 1999, ApJ, 517, 565
Pier J. R., Munn J. A., Hindsley R. B., Hennessy G. S., Kent S. M., Lupton R. H., Ivezić Ž., 2003, AJ, 125, 1559
Reid B. A., White M., 2011, MNRAS, 417, 1913
Reid B. A. et al., 2012, MNRAS, 426, 2719
Riess A. G. et al., 1998, AJ, 116, 1009
Riess A. G. et al., 2011, ApJ, 730, 119
Ross A. J. et al., 2011, MNRAS, 417, 1350
Ross A. J. et al., 2012, MNRAS, 424, 564
Ross A. J. et al., 2014, MNRAS, 437, 1109
Rybicki G. B., Press W. H., 1995, Phys. Rev. Lett., 74, 1060
Samushia L. et al., 2014, MNRAS, preprint (arXiv:1312.4899)
Sánchez A. G. et al., 2013a, MNRAS, 433, 1201
Sánchez A. G. et al., 2013b, preprint (arXiv:1312.4854)
Schlegel D. J., Finkbeiner D. P., Davis M., 1998, ApJ, 500, 525
Seo H.-J., Siegel E. R., Eisenstein D. J., White M., 2008, ApJ, 686, 13
Seo H.-J. et al., 2010, ApJ, 720, 1650
Seo H.-J. et al., 2012, ApJ, 761, 13
Slosar A. et al., 2013, J. Cosmol. Astropart. Phys., 4, 26

Downloaded from http://mnras.oxfordjournals.org/ at University of California, Irvine on March 16, 2016

Smee S. et al., 2013, AJ, 146, 32
Smith J. A. et al., 2002, AJ, 123, 2121
Spergel D., Flauger R., Hlozek R., 2013, preprint (arXiv:1312.3313)
Story K. T. et al., 2013, ApJ, 779, 86
Stoughton C. et al., 2002, AJ, 123, 485
Strauss M. A. et al., 2002, AJ, 124, 1810
Sunyaev R. A., Zel'dovich Ya. B., 1970, ApSS, 7, 3
Suzuki N. et al., 2012, ApJ, 746, 85
Swanson M. E. C., Tegmark M., Hamilton A. J. S., Hill J. C., 2008, MNRAS, 387, 1391
Taruya A., Nishimichi T., Saito S., 2010, Phys. Rev. D, 82
Tegmark M. et al., 2004, ApJ, 606, 702
Tegmark M. et al., 2006, Phys. Rev. D, 74, 123507
Thomas D. et al., 2013, MNRAS, 431, 1383
Tojeiro R. et al., 2012, MNRAS, 424, 136
Tojeiro R. et al., 2014, preprint (arXiv:1401.1768)
Tseliakhovich D., Hirata C., 2010, Phys. Rev. D, 82, 083520
Vargas-Magana et al., 2013, preprint (arXiv:1312.4996)
Veropalumbo A., Marulli F., Moscardini L., Moresco M., Cimatti A., 2014, MNRAS, preprint (arXiv:1311.5895)
Weinberg D. H., Mortonson M. J., Eisenstein D. J., Hirata C., Reiss A. G., Rozo E., 2013, Phys. Rep. 530, 87
White M. et al., 2011, ApJ, 728, 126
Xu X., Padmanabhan N., Eisenstein D. J., Mehta K. T., Cuesta A. J., 2012a, MNRAS, 427, 2146
Xu X., Cuesta A. J., Padmanabhan N., Eisenstein D. J., McBride C. K., 2012b, MNRAS, 431, 2834
Yoo J., Seljak U., 2013, Phys. Rev. D, 88, 103520
York D. G. et al., 2000, AJ, 120, 1579

[1]*Department of Astronomy, University of Washington, Box 351580, Seattle, WA 98195, USA*
[2]*APC, Astroparticule et Cosmologie, Université Paris Diderot, CNRS/IN2P3, CEA/Irfu, Observatoire de Paris, Sorbonne Paris Cité, 10, rue Alice Domon & Léonie Duquet, F-75205 Paris Cedex 13, France*
[3]*Lawrence Berkeley National Laboratory, 1 Cyclotron Road, Berkeley, CA 94720, USA*
[4]*Center for Cosmology and Particle Physics, New York University, New York, NY 10003, USA*
[5]*Department Physics and Astronomy, University of Utah, UT 84112, USA*
[6]*Apache Point Observatory, PO Box 59, Sunspot, NM 88349-0059, USA*
[7]*Institute of Cosmology & Gravitation, Dennis Sciama Building, University of Portsmouth, Portsmouth PO1 3FX, UK*
[8]*Instituto de Fisica Teorica (UAM/CSIC), Universidad Autonoma de Madrid, Cantoblanco, E-28049 Madrid, Spain*
[9]*Department of Physics, Yale University, 260 Whitney Ave, New Haven, CT 06520, USA*
[10]*Institut de Ciències del Cosmos, Universitat de Barcelona, IEEC-UB, Martíi Franquès 1, E-08028 Barcelona, Spain*
[11]*Harvard–Smithsonian Center for Astrophysics, 60 Garden St, Cambridge, MA 02138, USA*
[12]*CPPM, Aix-Marseille Université, CNRS/IN2P3, Cedex 07, Marseille, France*
[13]*Department of Astrophysical Sciences, Princeton University, Ivy Lane, Princeton, NJ 08544, USA*
[14]*Department of Physics, Carnegie Mellon University, 5000 Forbes Avenue, Pittsburgh, PA 15213, USA*
[15]*Department of Physics, Ohio State University, Columbus, OH 43210, USA*
[16]*Center for Cosmology and Astro-Particle Physics, Ohio State University, Columbus, OH 43210, USA*
[17]*Department of Physics and Astronomy, UC Irvine, 4129 Frederick Reines Hall, Irvine, CA 92697, USA*
[18]*University College London, Gower Street, London WC1E 6BT, UK*
[19]*IFIC, Universidad de Valencia-CSIC, E-46071 Valencia, Spain*
[20]*Max-Planck-Institut für extraterrestrische Physik, Postfach 1312, Giessenbachstr., D-85748 Garching, Germany*
[21]*Leibniz-Institut für Astrophysik Potsdam (AIP), An der Sternwarte 16, D-14482 Potsdam, Germany*
[22]*CEA, Centre de Saclay, IRFU, F-91191 Gif-sur-Yvette, France*
[23]*Institut d'Astrophysique de Paris, Université Paris 6, UMR7095-CNRS, 98bis Boulevard Arago, F-75014 Paris, France*
[24]*Campus of International Excellence UAM+CSIC, Cantoblanco, E-28049 Madrid, Spain*
[25]*Instituto de Astrofísica de Andalucía (CSIC), E-18080 Granada, Spain*
[26]*Department of Astronomy, Columbia University, New York, NY 10027, USA*
[27]*Department of Physics, University of California, 366 LeConte Hall, Berkeley, CA 94720, USA*
[28]*Department of Physics, Drexel University, 3141 Chestnut Street, Philadelphia, PA 19104, USA*
[29]*Korea Institute for Advanced Study, Dongdaemun-gu, Seoul 130-722, Korea*
[30]*Kavli Institute for the Physics and Mathematics of the Universe (WPI), Todai Institues for Advanced Study, The University of Tokyo, Chiba 277-8582, Japan*
[31]*National Abastumani Astrophysical Observatory, Ilia State University, 2A Kazbegi Ave., GE-1060 Tbilisi, Georgia*
[32]*Department of Astronomy and Astrophysics, The Pennsylvania State University, University Park, PA 16802, USA*
[33]*Institute for Gravitation and the Cosmos, The Pennsylvania State University, University Park, PA 16802, USA*
[34]*Instituto de Astrofísica de Canarias (IAC), C/Vía Láctea, s/n, E-38200 La Laguna, Tenerife, Spain*
[35]*Departamento de Física Teórica, Universidad Autónoma de Madrid, E-28049 Cantoblanco, Madrid, Spain*
[36]*Berkeley Center for Cosmological Physics, LBL and Department of Physics, University of California, Berkeley, CA 94720, USA*
[37]*Center for Astrophysics and Space Sciences, Department of Physics, University of California, 9500 Gilman Dr., San Diego, CA 92093 USA*
[38]*ICREA & ICC-UB University of Barcelona, Marti i Franques 1, E-08028 Barcelona, Spain*
[39]*Department of Astronomy, University of Wisconsin-Madison, 475 N. Charter Street, Madison, WI 53706, USA*
[40]*Department of Physical Sciences, The Open University, Milton Keynes MK7 6AA, UK*
[41]*Department of Astronomy, Ohio State University, Columbus, OH 43210, USA*
[42]*Department of Astronomy, University of California at Berkeley, Berkeley, CA 94720, USA*
[43]*Department of Astronomy, Case Western Reserve University, Cleveland, OH 44106, USA*
[44]*National Astronomy Observatories, Chinese Academy of Science, Beijing 100012, People's Republic of China*

This paper has been typeset from a TEX/LATEX file prepared by the author.

Downloaded from http://mnras.oxfordjournals.org/ at University of California, Irvine on March 16, 2016